

Tobias Großmann

Whispering-Gallery-Mode Lasing in Polymeric Microcavities

Whispering-Gallery-Mode Lasing in Polymeric Microcavities

Zur Erlangung des akademischen Grades eines
DOKTORS DER NATURWISSENSCHAFTEN
von der Fakultät für Physik
des Karlsruher Instituts für Technologie (KIT)

genehmigte

DISSERTATION

von

Dipl.-Phys. Tobias Großmann
aus Chang-Hua/Taiwan

Tag der mündlichen Prüfung : 23.11.2012

Referent : Prof. Dr. Heinz Kalt

Korreferent : Priv.-Doz. Dr.-Ing. Timo Mappes

Prüfungskommission:

Prof. Dr. W. Wulfhekel

Prof. Dr. H. Kalt

Priv.-Doz. Dr.-Ing. T. Mappes

Prof. Dr. A. Mirlin

Prof. Dr. W. de Boer

Prof. Dr. J. Kühn



Karlsruher Institut für Technologie (KIT)

Institut für Angewandte Physik

Wolfgang-Gaede-Straße 1

76131 Karlsruhe

<http://www.aph.kit.edu/kalt>

Tobias Großmann

tobias.grossmann@kit.edu

This work was performed in close collaboration between the Institut für Angewandte Physik and the Institut für Mikrostrukturtechnik at the Karlsruher Institut für Technologie (KIT). Financial support was provided by the Deutsche Telekom Stiftung, the Karlsruhe School of Optics and Photonics (KSOP), the Karlsruhe House of Young Scientists (KHYS), and the DFG Research Center for Functional Nanostructures (CFN), by a grant from the Ministry of Science, Research, and the Arts of Baden-Württemberg (Grant No. Az:7713.14-300) and by the German Federal Ministry for Education and Research BMBF (Grant No. FKZ 13N8168A).



Deutsche Telekom Stiftung



Karlsruhe School of Optics & Photonics

Contents

1	Introduction	1
2	Microgoblets as whispering galleries	5
2.1	Whispering-gallery modes in optical microcavities	5
2.1.1	Classification of WGMs	8
2.1.2	Optical properties of microcavities	8
2.2	Passive high-Q microgoblet resonators	14
2.2.1	Lithographic fabrication of microgoblets	15
2.2.2	Resonator-waveguide coupling	17
2.2.3	Experimental setup for tapered optical fiber coupling	19
2.2.4	Q-factor and modal Structure of WGMs in microgoblets	21
2.2.5	Finite element simulations of WGMs in microgoblets	24
2.3	Summary and conclusions	27
3	Low-threshold microgoblet dye lasers	29
3.1	Dye laser basics	29
3.1.1	Chemical structure of organic dyes	30
3.1.2	Free-electron model	31
3.1.3	Optical transitions in dye molecules	32
3.1.4	Dyes as gain medium	34
3.2	Dye-doped microgoblet lasers	38
3.2.1	Rhodamine-doped PMMA	39
3.2.2	Rhodamine-doped microgoblets	40
3.2.3	Pyromethene-doped microgoblets	46
3.3	Microgoblet lasers for label-free biosensing	50
3.3.1	Optical biosensors	51
3.3.2	High-Q WGMs for label-free molecule detection	52
3.3.3	Microgoblet lasers in aqueous environments	57
3.3.4	Label-free detection of proteins	61
3.4	Summary and conclusions	64

4	Microgoblet lasers with extrinsic gain layer	65
4.1	Dip-pen nanolithography on microgoblets	66
4.1.1	DPN for surface functionalization of microgoblets	66
4.1.2	DPN for active microgoblets	69
4.1.3	Integration of gain and biofunctionality in phospholipid-coated microgoblets	70
4.1.4	Summary and conclusions	71
4.2	Low-threshold lasing in organic semiconductor microgoblets	72
4.2.1	Guest-host organic semiconductors	73
4.2.2	Simulation of WGMs with organic gain layer	74
4.2.3	Lasing properties of organic semiconductor microgoblets	76
4.2.4	Summary and conclusions	79
5	Photonic molecule lasers for enhanced light-matter interaction	81
5.1	Whispering-gallery modes in photonic molecules	82
5.1.1	Classification of supermodes in PMs	83
5.1.2	Supermodes in coupled polymeric microdisks	85
5.2	Fabrication of polymeric photonic molecules	86
5.3	Spectroscopy of supermode lasing	89
5.4	Vernier effect in photonic molecule lasers	91
5.5	Photonic molecules for sensing applications	93
5.5.1	Summary and conclusions	95
6	Summary	97
A	Nanoporous liquid-core lasers	101
	Publications	105
	References	109
	Acknowledgements	125

Chapter 1

Introduction

Nearly a century after Einstein's theoretical description of the process of stimulated emission in 1916 [1], which formed the basis for first experimental realizations of lasers by Townes and Maiman in the 1960s [2, 3], the development of novel devices and applications based on lasers are nowadays still a hot topic in science and technology [4, 5]. One of the first type of cavities used to generate coherent laser light through stimulated emission was a so-called whispering-gallery-mode resonator, where the light is confined via repeated total internal reflection at the boundary of the dielectric structure, forming a whispering-gallery mode (WGM). Shortly after the first experimental realization of a laser by Maiman, Garret et al. reported in 1961 whispering-gallery-mode lasing from polished spheres made of doped calcium fluoride with diameters in the order of several millimeters [6].

Over the last years, advances in micro- and nano-fabrication have enabled continuous down-scaling of these whispering-gallery-mode lasers. Devices with low-threshold or even thresholdless lasers have been proposed and demonstrated as efficient sources of radiation that operate at room temperature and occupy a small volume on a chip [5, 7, 8]. Besides the investigation of lasing, the ability to achieve an ultra-high resonator quality in combination with a small mode volume has made WGM microcavities highly promising for a broad range of applications and scientific research, such as non-linear optics [9–11], cavity quantum electrodynamics (c-QED) [12–14], optical telecommunications [15, 16] and sensing [4, 17, 18].

One of the driving technological breakthroughs leading to the broad utilization of WGM resonators was the development of surface-tension induced cavity geometries, which were first demonstrated for the case of microspheres made from silicon dioxide (SiO_2) [19, 20] and later transferred to on-chip resonators in the form of microtoroids [21, 22]. Microcavities fabricated with a surface-tension induced reflow step can

possess an atomic-scale surface finish [21], which leads to extremely long photon lifetimes in the cavities. Unfortunately, the reflow process of SiO_2 has to occur with a high-power carbon dioxide (CO_2) laser. This process has two major disadvantages. Firstly, the CO_2 laser produces temperatures above 1000°C on the silicon chip, which hinders the additional integration of further components onto the same wafer. Secondly, the reflow process using laser radiation is a serial fabrication technique, so that microtoroids can hardly be produced on a large scale.

These limitations can be overcome by the employment of thermoplastic polymers with a low glass-transition temperature (slightly above 100°C), such as poly(methyl methacrylate) (PMMA), as cavity material instead of SiO_2 . This allows for thermal reflow at temperatures which are around one order of magnitude lower compared to temperatures needed for reflow of SiO_2 and therefore enables large-scale fabrication of polymeric devices [23]. Besides this, polymers have the advantage of being low-cost materials [24] which can easily be tailored for different applications, e.g., by integration of additional functional chemical components or gain media [25].

Low material costs and large-scale fabrication in combination with a surface-tension induced cavity geometry make the utilization of polymeric whispering-gallery-mode resonators highly attractive for biosensing applications where the development of disposable sensor chips is of major interest [26]. These biosensors for the label-free detection of molecules are promising for the point-of-care diagnosis, where the entire analysis system is ideally integrated in a compact hand-held device. This high integration level is one of the primary properties for future label-free biosensors [27]. So far, experiments with passive WGM resonators with high quality factors demonstrated a sensitivity down to the single molecule level [17]. Despite this promising prospect of an extremely high sensitivity, the technology used for the excitation of WGMs in passive microcavities via tapered fibers is a major drawback for the development of commercial products based on passive, on-chip devices. Tapered fibers can degrade within hours and require a positioning precision on the nanometer scale.

One solution to overcome the aforementioned technological difficulties of operating passive high-Q microresonators is the use of active microcavities instead of passive ones. In addition to the possibility of using the robust free-space excitation and detection of lasing modes, active microcavities in principle allow for an even higher detection sensitivity compared to their passive counterparts. This originates from the narrower linewidths achievable with active cavities due to the compensation of propagation losses in the presence of gain [28, 29]. Therefore, in combination with the cost advantage of polymers, efficient on-chip polymeric WGM lasers are one of the most attractive approaches for the realization of compact systems for label-free molecule detection.

To achieve a high detection sensitivity utilizing photonic microstructures, two different strategies can be pursued. Firstly, the quality of the resonator should be maximized, which can be achieved by using surface-tension-induced microcavity geometries. This results in multiple interactions of the photons circulating in the cavity with the analyte, leading to a high sensitivity [18]. Secondly, the spatial overlap of the optical modes with the target molecules can be increased. A promising approach predicted in theory to enhance the light-matter interaction is the employment of two coupled resonators, referred to as a photonic molecule (PM) [30, 31]. The spatial distribution of modes in PMs can be altered compared to single cavities, such that sufficiently small coupling-gap sizes between two microcavities can result in a significant field enhancement in the coupling-gap region [32]. The overlap of the optical mode with the environment is significantly enlarged in this region. This could make photonic molecules attractive for applications besides biosensing, where a large light-matter interaction is required, such as c-QED [31].

The objective of this work comprises the development of efficient polymeric lasers based on whispering-gallery modes with a focus on their application for label-free biosensing. For this, surface-tension induced resonators as well as coupled microcavities forming a photonic molecule are fabricated and characterized. The integration of efficient gain media into polymeric microresonators is a further central point of this work. Different experimental approaches for the integration of organic gain materials are investigated. The lasing characteristics are analyzed experimentally using photoluminescence spectroscopy and interpreted by comparison with results from finite element calculations.

Organization of the thesis

This thesis is structured in six chapters. In chapter 2, a general description of the properties of whispering-gallery modes and their occurrence in optical microcavities is given. After establishing the figures of merit of optical microcavities, such as whispering-gallery-mode resonators, a specific type of polymeric resonator with a goblet-like geometry, which was developed by the surface-tension-induced reflow of PMMA microdisks, is introduced. The optical properties of these microgoblet resonators without gain medium are characterized experimentally using tapered optical fiber coupling as well as theoretically with finite element simulations.

An efficient type of gain medium, which is promising for integration in polymeric microcavities, are organic laser dyes. A general discussion of the properties of dye molecules and their application as gain medium is presented in chapter 3. For the development of polymeric microgoblet lasers, PMMA was doped with the dyes rho-

damine 6G and pyrromethene 597, resulting in optically pumped lasers emitting at wavelengths around 600 nm. The operation of these WGM lasers in aqueous environments allows for their application as biosensors, and the label-free detection of proteins with microgoblet lasers is presented in the last section of this chapter.

Besides direct doping of the polymer, two different approaches for the realization of an extrinsic gain layer on top of microgoblet resonators are investigated in chapter 4. In the first approach, dip-pen nanolithography (DPN) is utilized to coat the cavity circumference with a molecular ink doped with laser dyes. A second approach, which allows for low-threshold lasing, is the deposition of a gain material with high refractive index onto the microgoblets. For this, an organic semiconductor is used. The modification of the optical modes in the presence of a coating with high refractive index is analyzed with finite element simulations and compared to experiments where the effect of the gain layer thickness on the lasing properties is studied.

Chapter 5 begins with an overview of the optical properties and applications of photonic molecules and photonic-molecule lasers. Subsequently, a lithographic fabrication method for the realization of strongly coupled polymeric microdisks is presented. The lasing properties of dye-doped photonic molecules are investigated using spatially resolved microphotoluminescence spectroscopy. This technique allows for the direct imaging of whispering-gallery modes in photonic molecules and enables the study of the mode localization in these structures. Finally, photonic-molecule lasing is investigated in aqueous environments. The properties of photonic molecules for sensing applications are characterized and compared to the case of single microcavities.

In the last chapter, the most important results of this work are summarized, conclusions are drawn, and an outlook for future research in this field is given.

Chapter 2

Microgoblets as whispering galleries

This chapter begins with a general description of the properties of whispering-gallery modes and their occurrence in optical microcavities. After describing the general properties and figures of merit of whispering-gallery resonators, a specific type of polymeric resonator with a goblet-like geometry, which was developed and investigated in this work, is introduced. The optical properties of microgoblet resonators without gain medium were characterized experimentally using tapered optical fiber coupling as well as theoretically with finite element simulations. These resonators form the basis for the realization of microcavity lasers, which is presented in the following chapters.

2.1 Whispering-gallery modes in optical microcavities

First studies of the phenomenon of whispering galleries were reported in literature in the early 19th century [33] and were explained by Lord Rayleigh [34, 35] at the beginning of the 20th century based on observations made in St. Paul's Cathedral in London, where acoustic waves, e.g., whispers, could be heard along the whole circumference of the gallery, due to repeated reflections on the side walls.

In the 1930s similar phenomena were proposed for electromagnetic waves at optical frequencies [36], where light waves can be confined within dielectric media with curved boundaries, if the refractive index of the dielectric structure is larger

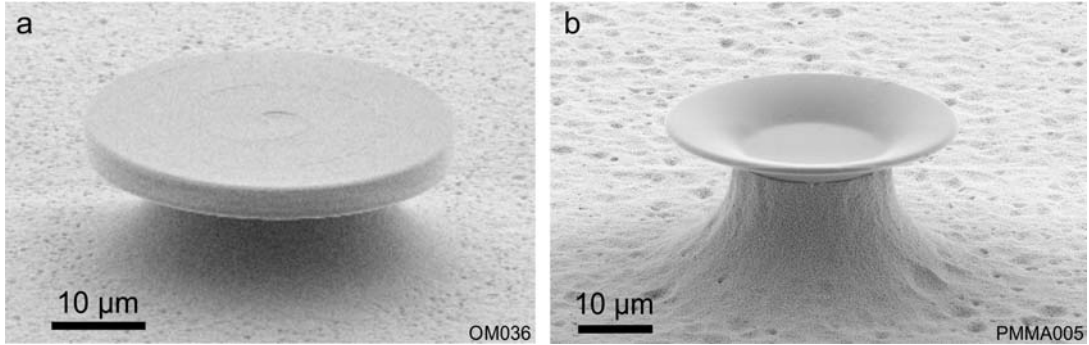


Figure 2.1: Scanning electron micrograph of a polymeric (a) microdisk [45] and (b) microgoblet [23].

than that of the surrounding, leading to repeated (total) internal reflections and the interference of the light wave with itself after a roundtrip. In the case of constructive interference, the waves in resonance form a so-called whispering-gallery mode (WGM). The simplest geometries of dielectric microcavities in which WGMs can be excited often have a rotational symmetry, such as spheres [6, 37, 38], disks [39–41], toroids [21, 42, 43] and goblets [23]. Examples of two types of WGM resonators investigated in this work are depicted in Fig. 2.1, showing scanning electron micrographs of a polymeric microdisk and microgoblet.

For a WGM microcavity consisting of a dielectric material with rotational symmetry, radius R and refractive index n , the simple resonance condition for a WGM with the free-space resonance wavelength λ_0 leading to constructive interference in the cavity is

$$2\pi R = N_\phi \lambda_0 / n \quad (2.1)$$

N_ϕ is an integer describing the number of wavelengths of the WGM within the circumference of the cavity and is called azimuthal mode number in the following. In this work, the typical microcavities have radii in the order of $10 \mu\text{m}$, which is much larger than light at visible wavelengths. Hence, the azimuthal mode number N_ϕ is much larger than one. In this mesoscopic regime, a description of WGMs by geometric optics is also valid and leads to the same results as wave optics [44]. For cavities without rotational symmetry, the left side of equation 2.1 can be replaced by the circumference of the resonator.

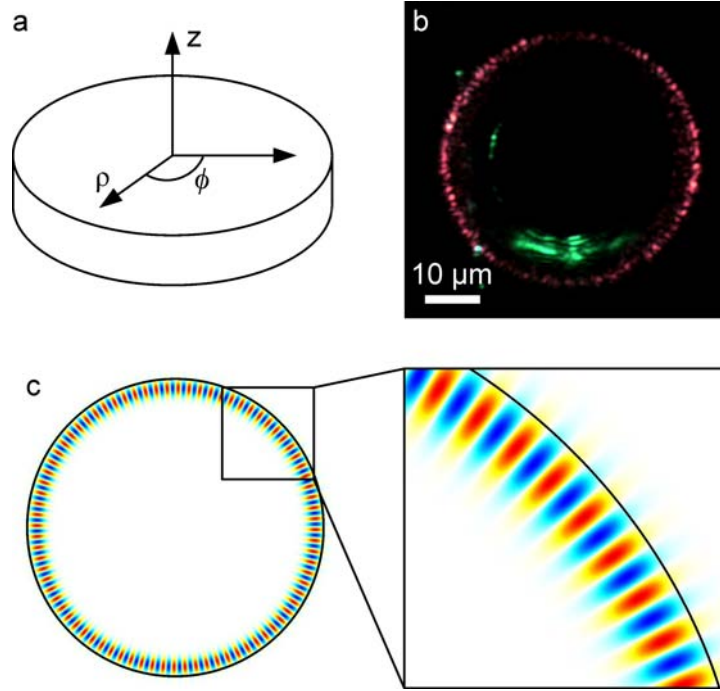


Figure 2.2: Visualization of WGMs. (a) Geometry of an ideal microdisk with coordinate system. (b) Microscope image showing excited WGMs in a dye-doped polymeric microcavity. (c) Results of numerical simulations showing a WGM with $N_\phi = 80$ in an ideal microdisk. The electric field component E_z of a WGM in the (ρ, ϕ) -plane is depicted. The red color indicates the maximum, the blue color the minimum field strength.

Equation 2.1 does not give any information about the spatial distribution of the electromagnetic field of the modes. It only states that a WGM has an N_ϕ -fold rotational symmetry, which is an important parameter for the classification of modes and can be directly derived from Maxwell's equations.

Examples of visualized WGMs in resonators with rotational symmetry are depicted in Fig. 2.2. Fig. 2.2 (b) shows an optical microscope image of an excited WGM in a polymeric microcavity. Simulation results of an ideal microdisk with $N_\phi = 80$ are depicted in Fig. 2.2 (c), where the electric field in z -direction in the (ρ, ϕ) -plane of the microdisk is shown. The field distribution was obtained by numerically solving Maxwell's equations for the geometry of a microdisk and shows how WGMs are confined within a curved dielectric. These examples show that the electric field is located close to the boundary of the microcavity. Only a small fraction of the electric field (the evanescent field) is guided out of the cavity. The evanescent field of WGMs mediates the interaction of the mode with the environment, which is a widely used mechanism in sensing applications [18, 27, 46, 47].

2.1.1 Classification of WGMs

In addition to the above stated condition (equation 2.1) for constructive interference along the propagation in ϕ -direction, WGMs with low losses have to fulfill resonance conditions in the ρ - and z -direction in order to be entirely confined within the three-dimensional microcavity. Therefore, two further mode numbers, N_ρ and N_z , are introduced to describe the confinement in the direction lateral to the propagation to fully classify whispering-gallery resonances. N_ρ and N_z denote the number of maxima minus one of the energy density in ρ - and z -direction respectively.

Besides the order of the resonance in the three directions, the two polarization states transverse magnetic (TM) and transverse electric (TE) lead to slightly different resonance wavelengths and have to be distinguished. Modes with an electric field dominantly polarized perpendicular to the (ρ, ϕ) -plane are called TM modes, while modes with a magnetic field polarized perpendicular to the (ρ, ϕ) -plane are called TE modes. The abbreviated notation for WGMs in this work will be $\text{TM}_{N_\rho, N_z}^{N_\phi}$ or $\text{TE}_{N_\rho, N_z}^{N_\phi}$.

Examples of the classification of WGMs in an ideal microdisk are depicted in Fig. 2.3, where the energy density $w = \epsilon|\vec{E}|^2$ of different TE modes in the plane $\phi = 0$ close to the rim of the microdisk is depicted. The $\text{TE}_{0,0}^{381}$ mode is called fundamental mode and has the largest resonance wavelength. The other modes with more than one maximum of the energy density in the axial (z) or radial (ρ) direction are higher-order modes.

2.1.2 Optical properties of microcavities

The spatial and temporal confinement of WGMs in optical microcavities as well as the optical density of states strongly depends on the geometry of the resonator and, due to the strong overlap of WGMs with the surface of the cavity, on the surface roughness of the dielectric structure. The following section will give an overview of the characteristic figures of merit to generally quantify the confinement of energy in optical microcavities and to show the dependency of these figures on the geometry of the cavity.

Mode volume

A commonly used measure for a quantitative description of the spatial confinement of modes in microcavities is the mode volume. The mode volume describes the spatial

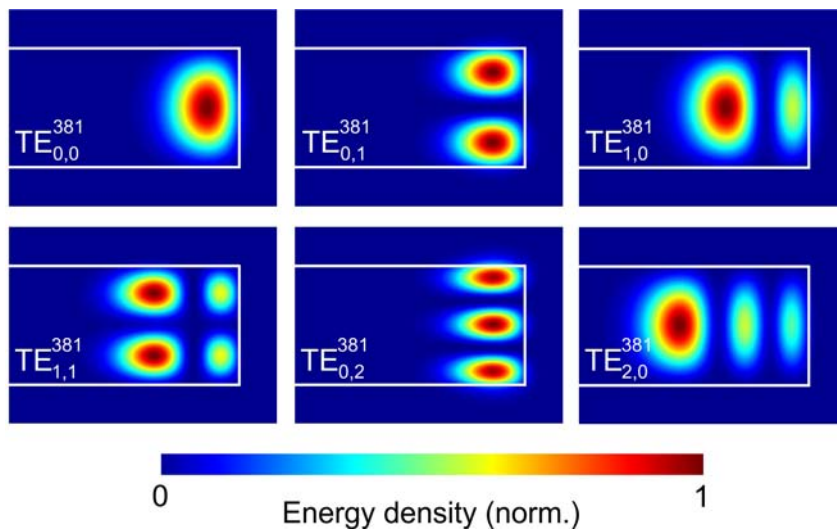


Figure 2.3: Example of the classification of WGMs in an ideal microdisk. The images show cross-sections of the electric energy density in the plane $\phi = 0$ close to the outer boundary of the microdisk.

volume inside and outside the resonator in which the main part of the energy density of a mode is confined.

Several different definitions are common for the computation of the mode volume, depending on the physical problem. For example, for the description of non-linear effects other definitions of an effective mode volume are more suitable than definitions used in quantum optics [48]. In the most common definition of mode volume V_m , it is defined as the equivalent spatial volume the mode occupies, if the energy density w is distributed homogeneously at the maximum value w_{\max} [48]:

$$V_m = \frac{\int w(\vec{r}) dV}{w_{\max}} = \frac{\int \epsilon(\vec{r}) |\vec{E}(\vec{r})|^2 dV}{\max [\epsilon(\vec{r}) |\vec{E}(\vec{r})|^2]} \quad (2.2)$$

Typical units for the mode volume of microcavities are μm^3 or cubic wavelengths $(\lambda_0/n)^3$.

Free spectral range

A further quantity depending on the geometry of a microcavity is the free spectral range $\delta\lambda_{\text{FSR}}$ (FSR). The FSR describes the spectral distance between consecutive longitudinal modes (N_ϕ and $N_\phi + 1$) with the same N_ρ and N_z mode numbers and

polarization, such as the spectral spacing between fundamental modes. The FSR of WGMS in cavities with rotational symmetry can be calculated with equation 2.1 and is given by [49]:

$$\delta\lambda_{\text{FSR}} = \frac{\lambda_0^2}{2\pi Rn + \lambda_0} \approx \frac{\lambda_0^2}{2\pi Rn} \quad (2.3)$$

The approximation in the last step is valid for $R \gg \lambda_0$ and is therefore valid for all cavities investigated in this work. Values for the FSR of optical microcavities are typically in the order of several nanometers.

Quality factor

The quality factor (Q-factor) is one of the most important figures of merit for quantification of the temporal confinement of energy in an optical microcavity and can generally be used to characterize the dissipation in all types of resonant systems. The Q-factor of a mode with eigenfrequency ω_0 is defined as the ratio of the stored energy U to the dissipated power $-dU/dt$ per cycle of the electric field and can also be expressed by the photon lifetime τ in the cavity [50]:

$$Q = \omega_0 \frac{\text{stored energy}}{\text{dissipated power}} = \omega_0 \frac{U}{-dU/dt} = \omega_0\tau \quad (2.4)$$

From this equation, the time dependency of the energy $U(t)$ stored in the cavity can be determined:

$$U = U_0 e^{-\omega_0 t/Q} \quad (2.5)$$

This equation shows that the cavity Q-factor can be directly determined by measuring the temporal decay of the energy in so-called cavity-ringdown measurements [21]. This type of measurement is difficult to perform experimentally. An alternative and more practical way to determine the Q-factor is the measurement of the resonance linewidth in the frequency domain. This approach is derived and discussed in the following.

Due to the relation $U(t) \propto E(t)^2$, the time dependency of the electric field is given by

$$E(t) = E_0 e^{-\omega_0 t/2Q} e^{-i\omega_0 t} \quad (2.6)$$

Fourier transformation of equation 2.6 results in the Lorentzian-shaped intensity distribution of the resonance

$$I(\omega) \propto \frac{1}{(\omega - \omega_0)^2 + (\omega_0/2Q)^2} \quad (2.7)$$

This Lorentzian lineshape has a full width at half maximum of $\delta\omega = \omega_0/Q$. The Q-factor is therefore given as

$$Q = \frac{\omega_0}{\delta\omega} \approx \frac{\lambda_0}{\delta\lambda} \quad (2.8)$$

and can thus be directly inferred from the linewidth of the resonance.

Loss mechanisms in optical microcavities

The Q-factor in microcavities is limited by the three main intrinsic loss mechanisms absorption (Q_{abs}^{-1}), radiation (Q_{rad}^{-1}) and surface scattering (Q_{ss}^{-1}) as well as an extrinsic loss (Q_{ext}^{-1}), which only occurs when light is coupled into the resonator by an external coupler, such as a tapered optical fiber or a prism, and therefore can also be dissipated via this channel. The total Q-factor can then be expressed by the Q-factors resulting from these individual loss mechanisms via [39]

$$\begin{aligned} \frac{1}{Q} &= \frac{1}{Q_{abs}} + \frac{1}{Q_{rad}} + \frac{1}{Q_{ss}} + \frac{1}{Q_{ext}} & (2.9) \\ &= \frac{1}{Q_0} + \frac{1}{Q_{ext}} & (2.10) \end{aligned}$$

The intrinsic loss mechanisms are summarized in the intrinsic Q-factor Q_0 with $Q_0^{-1} = Q_{abs}^{-1} + Q_{rad}^{-1} + Q_{ss}^{-1}$. In the following, the physical background of these three contributions to Q_0 are discussed and an order of magnitude estimation of each contribution for the polymeric WGMs resonators investigated in this work will be given.

Absorption losses

The absorption of the electromagnetic wave in the dielectric cavity material can be expressed via the complex refractive index $\tilde{n} = n + i\kappa$ or the linear attenuation coefficient $\alpha = \lambda/(4\pi\kappa)$ and limits the Q-factor as follows [51]:

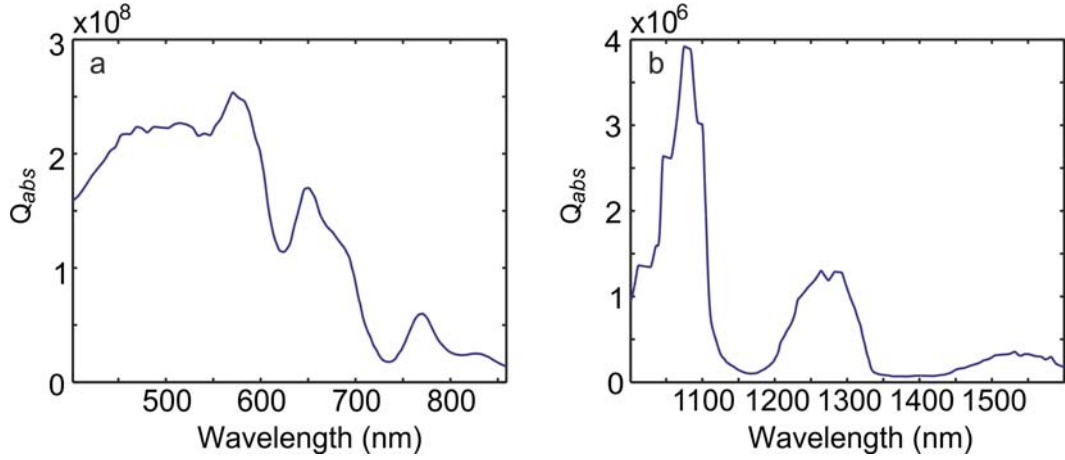


Figure 2.4: Calculated absorption-limited Q-factors Q_{abs} in PMMA based on absorption spectra reported in literature [52–54]. In PMMA microcavities, the Q-factors can reach values in the order of 10^8 in the visible spectral region (a) and values in the order of 10^6 in the infra-red wavelength region (b).

$$Q_{abs} = \frac{n}{2\kappa} = \frac{2\pi n}{\alpha\lambda} \quad (2.11)$$

The polymers used to fabricate microcavities in this work, e.g., poly(methyl methacrylate) (PMMA), have low absorption losses and are therefore ideal dielectric materials for the realization of high-Q microresonators. In PMMA microcavities, the absorption-limited Q-factor Q_{abs} can reach values in the order of 10^8 at visible wavelengths and values around 10^6 in the infra-red wavelength region (see Fig. 2.4).

Equation 2.11 implies that extinction losses of WGMs in resonators are identical to those of plane waves in the bulk medium. However, this approach is not accurate for Rayleigh scattering in WGM resonators, where small fluctuations in the dielectric constant cause scattering which is partially re-emitted into the mode [55] and hence do not cause energy losses as high as in the bulk material. Calculations show that Q_{abs} of WGMs can be up to almost one order of magnitude larger than expected from the extinction coefficient of the bulk material [55].

Radiation losses

Due to the curved surface of WGM resonators, a small fraction of the energy of the modes is inevitably lost by radiation. In the particle picture of light, this energy loss can be described as tunneling of photons through a potential barrier. These radiation losses are mainly determined by the curvature of the microcavity and

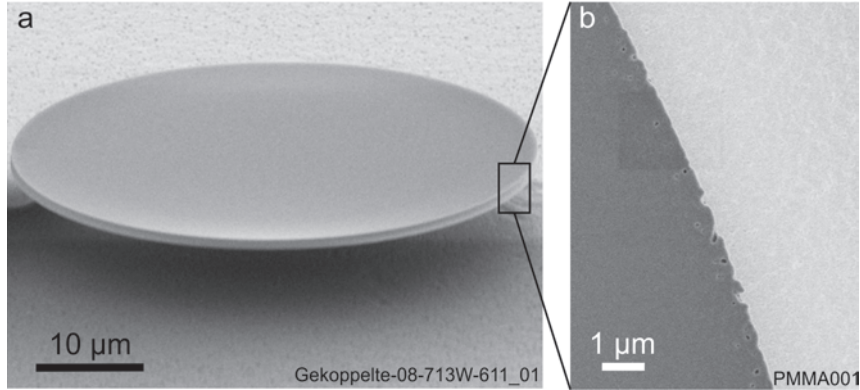


Figure 2.5: Scanning electron micrographs of (a) a PMMA microdisk and (b) an enlarged section of the cavity rim showing the surface roughness caused by lithographic structuring.

therefore strongly depend on the the radius R and the azimuthal mode number N_ϕ of the microcavity. From analytical calculations it can be derived that the radiation-limited Q-factor increases exponentially with N_ϕ . As N_ϕ is proportional to the radius (equation 2.1), the same dependency of Q_{rad} for increasing radius can be derived.

Due to the strong dependency of Q_{rad} on the cavity geometry, cavities investigated in this work were designed such that radiation-limited losses are negligible compared to the other loss mechanisms. The values of Q_{rad} were inferred from numerical simulations (see section 2.2.5). Radiation-limited Q-factors of typical WGM resonators in this work with a radius of $R=20\ \mu\text{m}$, $N_\phi=280$ and wavelength $\lambda=600\ \text{nm}$ are in the order of 10^{16} . In general, radiation losses increase significantly when the refractive index contrast between cavity and environment becomes smaller, e.g., if the WGM resonators are operated in aqueous environment. The lower refractive index contrast results in a lowered potential barrier and thus increased tunneling of photons out of the cavity. In aqueous environment, the WGMs in PMMA microcavities with the above mentioned geometry have radiation-limited Q-factors in the order of 10^8 at wavelengths around 600 nm.

Surface-scattering losses

As discussed in the previous section, WGMs are guided in dielectric cavities due to repeated reflections along the cavity surface. Due to the large overlap of the electric field of WGMs with the cavity surface, imperfections along the dielectric interface cause surface-scattering losses. Especially in lithographically structured microcavities, surface scattering is the dominating loss mechanism due to blemishes on the nanometer scale. An example of lithographic roughness after the fabrication of a PMMA microdisk is depicted on the scanning electron micrographs in Fig. 2.5.

Q-factors of polymeric microcavities after lithographic fabrication range between 10^4 and 10^6 , depending on the lithography technique [23, 45].

One possibility to reduce the influence of surface scattering is to increase the dimensions of the microcavity. Analytical calculations estimating the dependency of the surface-scattering limited Q-factor in microdisks show that Q_{ss} is proportional to the radius of the resonator [39] due to a smaller overlap of the WGM with the cavity surface. However, a larger cavity radius can have disadvantages for applications like biosensing, where a large evanescent field is desirable to gain high sensitivities [18]. Furthermore, large cavity dimensions are unwanted due to limitations in the achievable density of integrated photonic components.

Therefore, great efforts have been made over the last years to develop techniques to increase Q-factors of on-chip microcavities after lithographic structuring. A major scientific breakthrough was achieved by the introduction of a surface-tension-induced reflow step in the post-lithographic fabrication process. Q-factors above 10^8 were reported for microtoroids with a nearly atomic-scale surface finish made from silicon dioxide (SiO_2) microdisks via carbon dioxide (CO_2) laser reflow [21]. This reflow step has two major disadvantages. Firstly, the CO_2 laser produces temperatures above 1000°C on the silicon chip, which hinders the additional integration of further components on the same wafer. Secondly, the reflow process with laser is a serial fabrication technique where every single microtoroid has to be addressed individually by the machining laser, so that microtoroids can hardly be produced on a large scale. These limitations can be overcome by using thermoplastic polymers with low glass-transition temperature, such as PMMA, as cavity material instead of SiO_2 . The lithographic fabrication on PMMA microcavities is discussed in the next section.

2.2 Passive high-Q microgoblet resonators¹

In this section the fabrication process involving a surface-tension induced reflow step of PMMA microdisks, resulting in a goblet-like cavity geometry, is introduced. The optical properties of passive microgoblets, i.e., without gain medium, such as the Q-factor and the mode structure, are characterized by tapered optical fiber coupling and compared to finite-element simulations. The microgoblet resonators introduced here form the basis for the realization of WGM lasers with low lasing threshold, which will be discussed in the next chapter.

¹The results presented in this section have been published in [23].

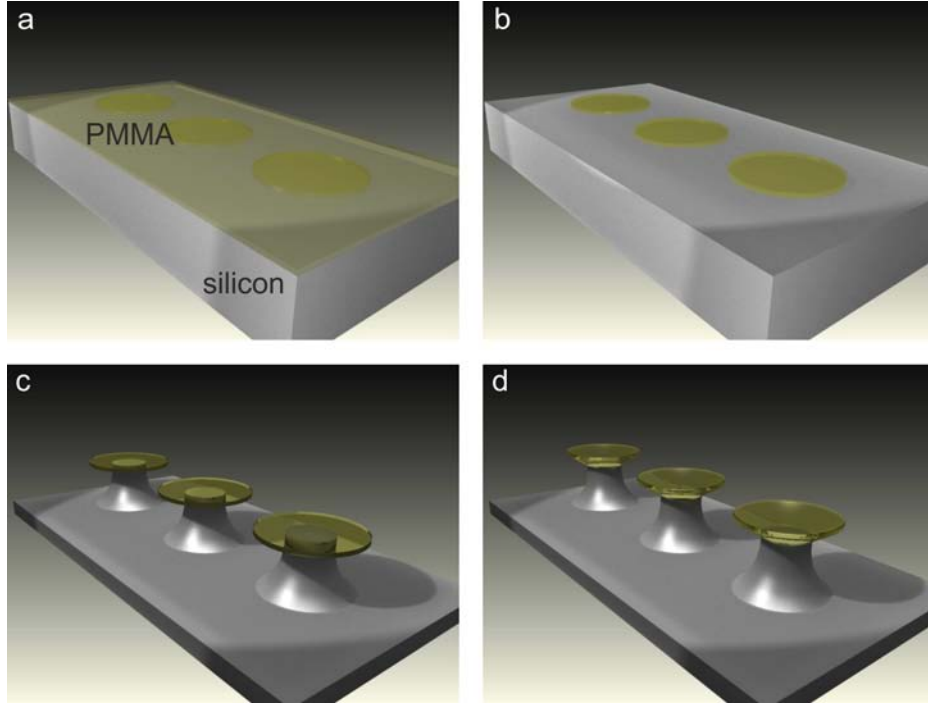


Figure 2.6: Fabrication of PMMA microgoblets. After exposure (a) and development (b) of PMMA, the silicon substrate is etched using XeF_2 (c). A thermal reflow (d) then forms the goblet-like geometry of the cavities [23].

2.2.1 Lithographic fabrication of microgoblets

The PMMA microcavities are fabricated in a four-step process that is applicable for mass production (Fig. 2.6). In a first step a $1\ \mu\text{m}$ thick PMMA layer (MicroChem PMMA 950k A7, 7 weight-% high molecular weight PMMA dissolved in anisole) is spin-coated on top of a silicon substrate. The sample is baked at 110°C in order to reduce the solvent content. While the sample cools down, stress develops between the PMMA and the silicon substrate due to the different thermal expansion coefficients² of the two materials. PMMA circles can then be patterned either by UV lithography using deep UV light ($\lambda = 240$ to $250\ \text{nm}$) and a quartz-chromium mask or by electron beam (e-beam) lithography (Fig. 2.6 (a)). In this work, samples were fabricated using e-beam lithography. After development (Fig. 2.6 (b)), the exposed silicon substrate is isotropically etched using XeF_2 , resulting in free-standing PMMA microdisks on silicon pedestals (Fig. 2.6 (c)).

²The thermal expansion coefficient at room temperature of PMMA is $300 \times 10^6\ \text{K}^{-1}$ [56] and $2.5 \times 10^6\ \text{K}^{-1}$ for silicon [57].

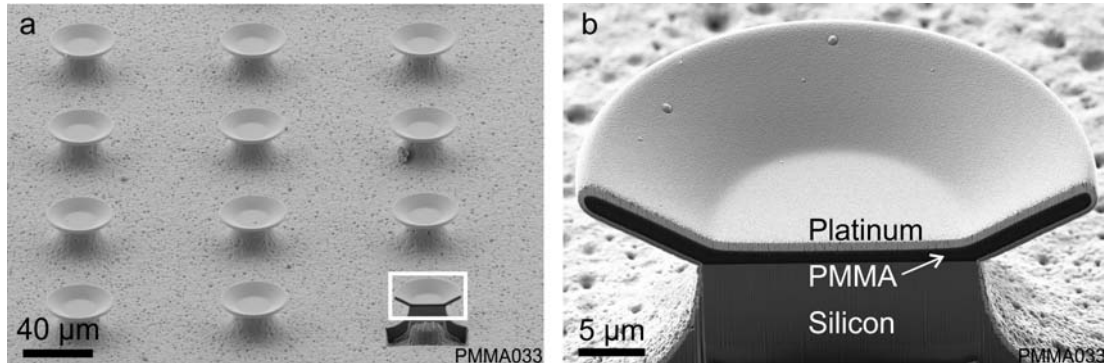


Figure 2.7: (a) Scanning electron micrograph of an array of PMMA microgoblets, where the bottom right resonator marked by a white rectangle was cut by focused ion beam (FIB). (b) Enlarged micrograph of the cut microgoblet showing the cross-section of the cavity. The resonator was coated with platinum to enable the FIB cut.

In order to take advantage of the stress in the PMMA layer, a thermal reflow step was developed that allows the reduction of surface roughness and the formation of the goblet-like geometry. When the PMMA islands are melted during the reflow process, the liquid photoresist surfaces are pulled into a shape which minimizes the energy of the system [58]. By heating the sample for 30 s on a hotplate at a temperature of 125 °C to slightly above the glass transition temperature T_g of PMMA ($T_g \approx 100 - 110$ °C, depending on how strongly the molecules are cross-linked), heat is transported in a well-defined manner through the silicon pedestal to the center of the cavity. The temperature of the PMMA being above the glass transition temperature allows the surface tension in the PMMA layer to smoothen the cavity surface [58]. In addition, the glass transition state enables the formation of a goblet resonator by allowing the PMMA to relax its residual stress in the rim-region and the upper side of the disk, while the central part of the lower side is fixed by the pedestal (Fig. 2.6 (d)). This process is self-quenching, as after the stress has relaxed no further forces apply to the microstructure, thus further treatment on the hotplate has no effect.

A scanning electron micrograph of an array of PMMA microgoblets after fabrication is depicted in Fig. 2.7 (a). The fact that all resonators on the substrate are fabricated with a single reflow step clearly demonstrates the fabrication advantages of this type of microcavity compared to silica microtoroids or microspheres. To visualize the cross-section of the microgoblets, focused ion beam (FIB) cuts of the microstructure were made. The resonator on the bottom right of Fig. 2.7 (a) is marked with a white rectangle and was cut by FIB. Figure 2.7 (b) gives an enlarged view of the resonator cross-section. One can clearly see the goblet-like geometry

formed by surface tension and the relaxing of the residual stress during the reflow process. To quantify the improvement of the thermal reflow on the optical properties of WGMs in goblet-shaped microcavities by measurement of the Q-factor, spectra of the resonances were recorded by evanescently coupling light into the resonator with a tapered optical fiber. The next sections give a mathematical description of evanescent coupling of energy into microcavities. The analytical expressions derived in the next section explain the characteristics of the resonance features observable in transmission measurements by tapered optical fiber coupling.

2.2.2 Resonator-waveguide coupling

Free-space excitation of whispering-gallery modes in polymeric microcavities is inefficient due to different phase velocities of waves in air and polymer. Efficient excitation of WGMs requires a phase matching of wave vectors, which can be achieved using a tapered waveguide, where the evanescent field overlaps with the modes of the resonator. This technique has been proven to be suitable to couple light into on-chip microcavities [59, 60].

A mathematical description of the resonator-waveguide coupling can be given by the coupling-of-mode formalism [61] in combination with the slowly varying amplitude approximation. This requires that the coupling between resonator and waveguide is weak, so that the perturbation of the resonator and waveguide mode is small. In the case of a strong coupling, analytical treatment would require the matrix model of the coupling amplitudes [62]. Both models yield the same results as long as the slowly varying amplitude approximation $E_c(t + T) - E_c(t) \approx T \frac{d}{dt} E_c(t)$ holds for the cavity field $E_c(t)$. T is the cavity round-trip time. With the coupling-of-modes approach, the resonator-waveguide coupling can be described by the three parameters ω_0 (resonance frequency of the cavity), $1/\tau_0$ (intrinsic cavity losses), and $1/\tau_{ex}$ (coupling losses to the waveguide) [61]:

$$\frac{d}{dt}a = i\omega_0 a - \left(\frac{1}{2\tau_0} + \frac{1}{2\tau_{ex}} \right) a + \kappa s \quad (2.12)$$

The resonator mode is denoted as a and the waveguide mode is denoted as s ³. The coupling coefficient is designated as κ and can be expressed by τ_{ex} using time reversal symmetry [61]: $\kappa^2 = 1/\tau_{ex}$.

³The quantities a and s have different units: $|a|^2$ is a normalized energy and $|s|^2$ is a normalized power.

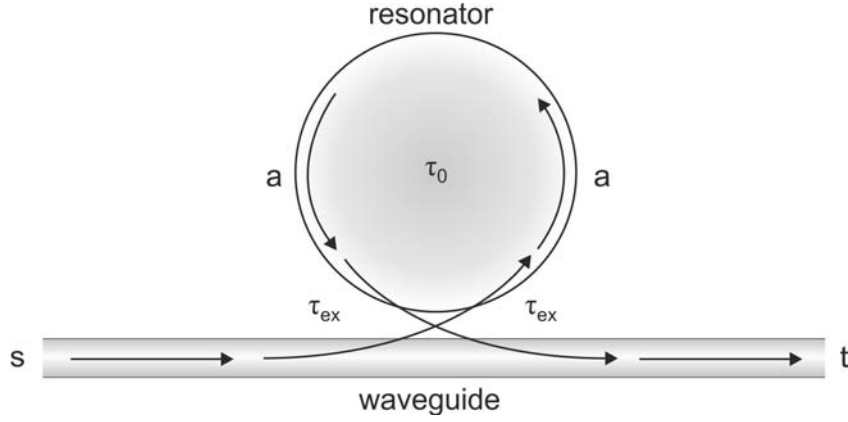


Figure 2.8: Scheme of waveguide-resonator coupling. A fraction of the power of the waveguide mode s is coupled in the resonator mode a . The transmitted signal t is a superposition of the transmitted part of s and the fraction of a , which is coupled back from the resonator into the waveguide. (Figure adapted from [59].)

Without waveguide, the energy loss of the resonator calculated by equation 2.12 is given by

$$\frac{d}{dt} |a|^2 = -\frac{1}{\tau_0} |a|^2 \quad (2.13)$$

The intrinsic Q-factor is therefore $Q = \omega_0 \tau_0$, which is consistent with equation 2.4.

Insertion of the ansatz $s \propto \exp(i\omega t)$ into equation 2.12 leads to the following expression for a :

$$a = \frac{\kappa s}{i(\omega - \omega_0) + (2\tau_0)^{-1} + (2\tau_{ex})^{-1}} \quad (2.14)$$

The transmitted field t in the waveguide (compare Fig. 2.8) is a superposition of the transmitted waveguide mode and the fraction of a , which is coupled back from the resonator into the waveguide. Using energy conservation, the transmission $T = |t|^2$ can be expressed as [61]

$$T = \left| \frac{\tau_{ex}^{-1} - \tau_0^{-1} - 2i(\omega - \omega_0)}{\tau_{ex}^{-1} + \tau_0^{-1} + 2i(\omega - \omega_0)} \right|^2 \quad (2.15)$$

$$= \left| \frac{Q_{ex}^{-1} - Q_0^{-1} - 2i(\omega - \omega_0)}{Q_{ex}^{-1} + Q_0^{-1} + 2i(\omega - \omega_0)} \right|^2 \quad (2.16)$$

The coupling-limited Q-factor Q_{ex} is determined by the amount of coupling to the waveguide with $Q_{ex} = \omega_0 \tau_{ex}$. Equation 2.16 shows that the transmission spectrum around the resonance frequency ω_0 recorded through an evanescently coupled waveguide has a Lorentzian-shaped linewidth. If the coupling losses are low ($Q_{ex} \gg Q_0$), the intrinsic cavity Q-factors Q_0 can be determined from the FWHM of the Lorentzian-shaped dip in the transmission spectrum. This regime is called undercoupled and is used to infer the Q-factor from transmission measurements. On the other hand, if $Q_0 \gg Q_{ex}$ the system is overcoupled and the loaded Q-factor with $Q_l^{-1} = Q_{ex}^{-1} + Q_0^{-1}$ can be significantly lower than the intrinsic Q-factor itself. For $Q_0 = Q_{ex}$, the system is critically coupled. In this case the transmission drops to zero at the resonance frequency ω_0 . The transmission vanishes due to the interference of the cavity leakage field and transmitted pump field, which exhibit equal magnitude but a relative phase shift π [63]. The entire power in the waveguide is dropped into the resonator and leads to a high field build-up in the cavity.

The introduced coupling coefficient κ (see section 2.2.2) and respectively Q_{ex} strongly depend on the distance between resonator and waveguide. In experiments, this distance has to be precisely controlled and determines the coupling regime in which the measurement occurs. In the following section the experimental setup used for tapered optical fiber coupling is described.

2.2.3 Experimental setup for tapered optical fiber coupling

In order to access the evanescent field of the guided fundamental mode in the core of single-mode fibers, the fiber cladding has to be removed. Flame brushing is a commonly used fabrication technique to manufacture tapered fibers. A small region (about 2 mm) of the fiber is heated by a flame and pulled apart by linear motors [64]. The tapered region has a length of several millimeters. The fundamental mode, which is guided by the refractive index difference between core and cladding, undergoes an adiabatic transition to an air-guided mode. This air-guided region is used for the evanescent coupling of light into the resonator. An schematic of a tapered optical fiber is depicted in Fig. 2.9(a). At the start of the stretching process, the air-guided fiber region supports multiple waveguide modes. To ensure that the air-guided region is single mode, the intensity transmitted through the fiber is monitored during the stretching process. Multiple modes in the air-guided region cause an oscillating signal due to beating. Further stretching of the fiber taper reduces the number of modes until the air-guided region becomes single mode and the oscillations in the transmitted signal disappear. Typical minimum taper-waist diameters for single-mode tapers for wavelengths in the region of 1300 nm are 1 μm .

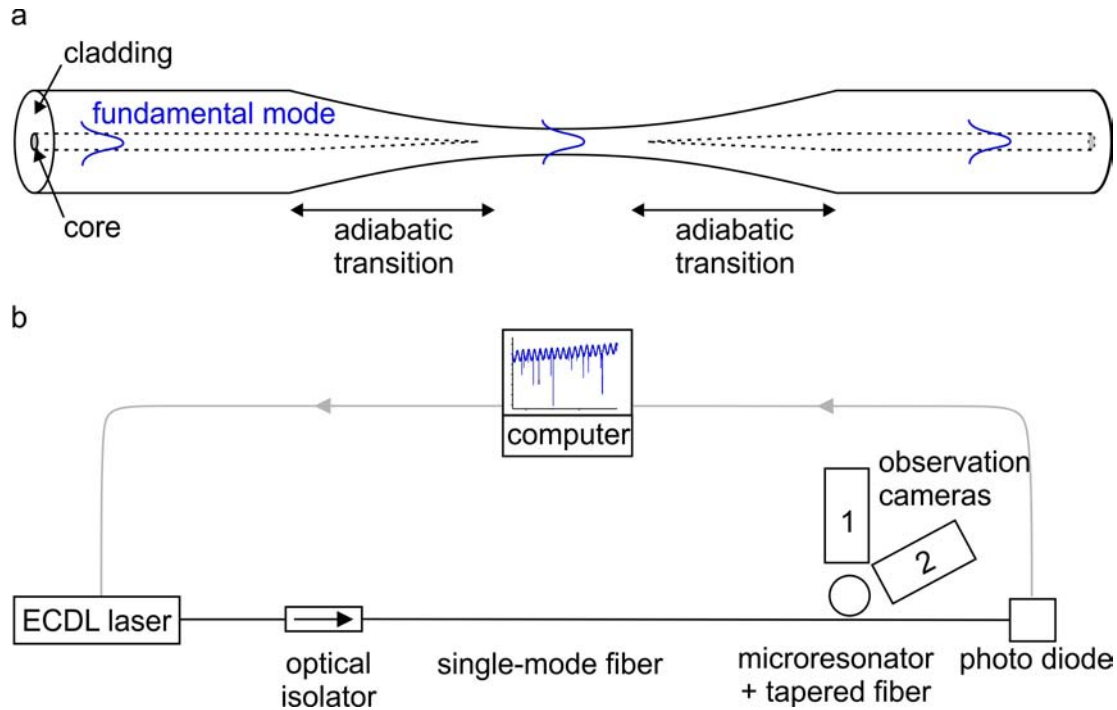


Figure 2.9: Measurement setup for tapered optical fiber coupling. (a) Tapered optical fibers have a region where the mode is guided in air after an adiabatic transition from the core-guided region. (b) Schematic of the transmission measurement setup to characterize WGMs in microresonators.

A schematic of the optical setup for transmission measurements is depicted in Fig. 2.9 (b). Central elements of the setup are a tunable, external-cavity laser source with narrow linewidth, the tapered optical fiber and the microscopes for the relative positioning of fiber and resonator.

In order to precisely align tapered fiber and microresonator, the tapered fiber was positioned on a five-axis positioning stage with a maximum resolution of 20 nm and monitored by two cameras from the top and the side. A microscope image showing a top view of a tapered fiber in close vicinity to a microgoblet is depicted in Fig. 2.10 (a). Measurement of the mode spectrum and Q-factor of the goblet resonators was performed in the 630 nm and 1300 nm wavelength region using external-cavity diode lasers (ECDL)⁴. The single-mode, tunable, external-cavity laser was connected to a single-mode optical fiber with a tapered section. While bringing the tapered section of the fiber close to the resonator, the tunable laser was conti-

⁴The ECDL with a tuning range from 1280 nm to 1390 nm (INTUN TL1300-B, Thorlabs) had a linewidth of 200 kHz and the ECDL with a tuning range from 633 nm to 637 nm (TLB-6304 Velocity, New Focus) had a linewidth smaller than 300 kHz.

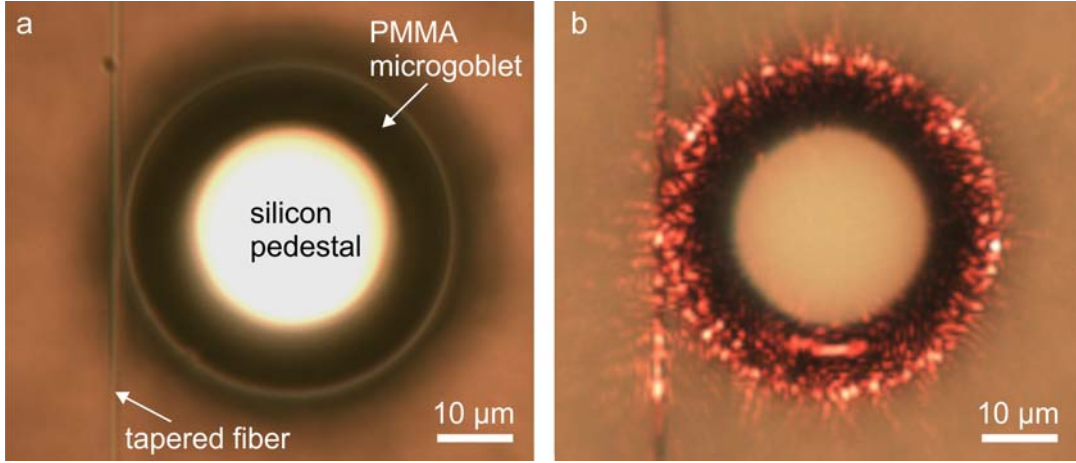


Figure 2.10: Microscope images of PMMA microgoblets. (a) Top view of the tapered fiber and the microgoblet. (b) Light from the tunable ECDL with a wavelength around 634 nm is coupled into the cavity.

nously swept and the transmitted intensity was monitored using a photodiode. The resonator-waveguide gap was adjusted until the cavity resonances appeared as sharp dips in the transmission spectrum and could be measured [23]. With the ECDL at 634 nm a coarse adjustment of the tapered fiber was performed by monitoring the scattered-light in the resonator during the alignment process. Fig. 2.10 (b) shows a microscope image for a taper-resonator distance where the laser light is coupled into the resonator.

2.2.4 Q-factor and modal Structure of WGMs in microgoblets

Transmission spectra of microgoblet resonators were recorded with the measurement setup described in the previous section. To minimize the influence of the measurement process itself on the cavity Q-factor, measurements were performed in the undercoupled regime in order to ensure that coupling losses to the waveguide are negligible with $Q_{ex} \gg Q_0$ [19]. Furthermore, the power of the ECDL was kept below several μW to avoid thermal distortion of the resonance linewidth due to field build-up in the cavity.

A typical transmission spectrum of a microgoblet with a diameter of 42 μm in the 1300 nm wavelength region is shown in Fig. 2.11 (a). The modal spectrum reveals a repeating comb-like structure, which can be attributed to the excitation of several

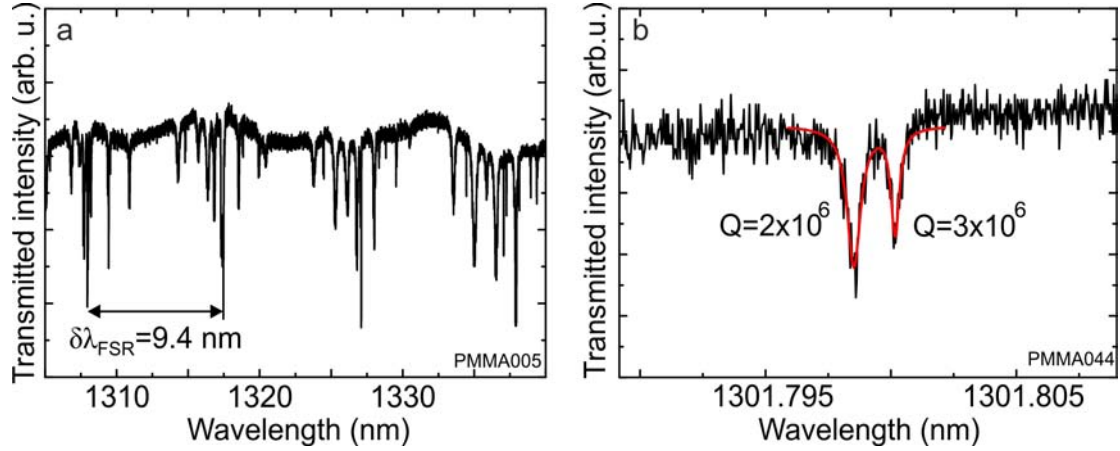


Figure 2.11: Mode spectrum and Q-factors of passive microgoblet resonators in the 1300 nm wavelength region. (a) Transmission spectrum recorded through an evanescently coupled tapered fiber. The free spectral range of a microgoblet with a diameter of $42 \mu\text{m}$ is 9.4 nm [23]. (b) Q-factors of the WGMs in microgoblets are as high as 3×10^6 in the 1300 nm wavelength region and were inferred from the FWHM of the Lorentzian fit (solid red line) of the resonance in the undercoupled regime [65].

different transverse modes which are spectrally separated by the free spectral range. Differing electric field distribution of different types of transverse cavity modes⁵ results in differing coupling strengths. This becomes apparent in the transmission spectrum by the varying height of the dips of different transverse modes. The free spectral range in Fig. 2.11 (a) can be clearly identified as 9.4 nm by the spectral separation of the resonances with the lowest value of the transmitted intensity in the minimum⁶.

Q-factors of the WGMs were inferred from the FWHM of the Lorentzian-shaped resonances in the transmission spectrum (see equation 2.8). Figure 2.11 (b) shows a section of the transmission spectrum around 1301 nm with two resonance dips. The Q-factors of the WGMs here are 2×10^6 and 3×10^6 . Compared to the Q-factors of PMMA microdisks, which are between 10^4 and 10^5 , the effective reflow step leads to an improvement of more than one order of magnitude. These Q-factors are as high as in replica-molded polymer microtoroids [24, 43], while the goblet microresonators take advantage of an inexpensive, large-scale compatible fabrication technique not needing a master array of ultrahigh-Q silica microtoroids for replica molding [23].

⁵The spatial energy density distribution of the WGMs in microgoblets is discussed and visualized in the following section using finite element simulations.

⁶These resonances are most likely the fundamental modes of the cavity, as these modes possess the largest spatial overlap of the field distribution with the fundamental mode of the tapered fiber.

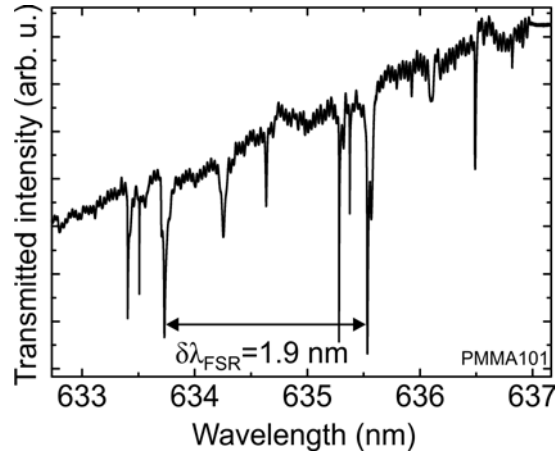


Figure 2.12: Mode spectrum of microgoblets in the 630 nm wavelength region. The free spectral range in this wavelength region is 1.9 nm.

Due to an ultrasmooth cavity surface and efficient coupling by a tapered fiber, the Q-factors of the goblet microcavities seem to be limited by absorption losses of PMMA rather than surface-scattering losses. This is supported by the fact that the values of absorption-limited Q-factors for PMMA reported in literature are around 10^6 [53] for wavelengths around 1300 nm (compare Fig. 2.4 (b)). These values of Q_{abs} are in the same order of magnitude as the measured Q-factors. This indicates that absorption losses in the infra-red wavelength region, mainly caused by vibrational absorption bands of PMMA [66], play a major role in the Q-factor limitation.

To further investigate the role of the different loss mechanisms in PMMA microgoblets, Q-factors were measured in the visible spectral region around 630 nm. In this wavelength region, absorption losses of PMMA are two orders of magnitude lower than for infra-red wavelengths [52] with $Q_{abs} \approx 10^8$ (compare Fig. 2.4 (a)). Measurements in this wavelength region should therefore give insight into whether Q-factors of microgoblets are ultimately limited by absorption of bulk PMMA or by surface-scattering losses.

A transmission spectrum of a tapered fiber coupled to a microgoblet in the wavelength region between 633 and 637 nm is depicted in Fig. 2.12. The free spectral range in this wavelength region was found to be 1.9 nm. The Q-factors in this wavelength region took on values as high as 2×10^6 . These values are as high as in the 1300 nm wavelength region. This verifies the hypothesis that absorption losses at infra-red wavelengths play a major role in the Q-factor limitations but are not the only contributing loss mechanism. If this were so, the Q-factor would take on values above 10^8 at 630 nm. Additional losses most likely originate from surface scattering

caused by dust particles on the cavity surface and a small number of remaining surface defects from the lithographic structuring.

2.2.5 Finite element simulations of WGMs in microgoblets

For a better understanding of the measured modes and for visualization of the spatial distribution of the excited WGMs in the microgoblets, finite element (FEM) simulations were performed to solve Maxwell's equations for a goblet-like geometry⁷. This is a simulation method especially suitable for calculation of eigenfrequencies, field distributions and Q-factors of dielectric structures for time-harmonic electromagnetic waves. In this work, simulations using the eigensolver `JCMResonance` (part of the simulation software package `JCMSuite` from JCMwave) were set up in cooperation with the Zuse Institute Berlin (ZIB).

Simulation method

The simulation method based on finite elements is a frequency domain eigensolver, which looks for solutions of Maxwell's equations within the computational domain that satisfy the appropriate boundary conditions at the boundary of the cavity. Using the time-harmonic ansatz for electromagnetic waves

$$\vec{E}(\vec{r}, t) = \vec{E}(\vec{r})e^{i\omega t} \quad (2.17)$$

reduces Maxwell's equations to an eigenvalue problem with the eigenvector \vec{E} and the eigenvalue ω^2 [67]:

$$\epsilon^{-1}\nabla \times \mu^{-1}\nabla \times \vec{E} - \omega^2\vec{E} = 0 \quad (2.18)$$

This eigenvalue problem is solved numerically by dividing the computational domain into a grid of small patches. The electromagnetic fields are then approximated by simple polynomial functions within these patches.

The three-dimensional simulation of microgoblets with geometric dimensions in the order of 1000 cubic wavelengths requires high computational resources. The FEM solver `JCMResonance` allows for considerable reduction of computational costs by taking advantage of the rotational symmetry of the resonator. The eigenvalues were

⁷Due to the reduced symmetry of microgoblets in comparison to ideal microdisks, analytical calculations to solve Maxwell's equations are not straightforward.

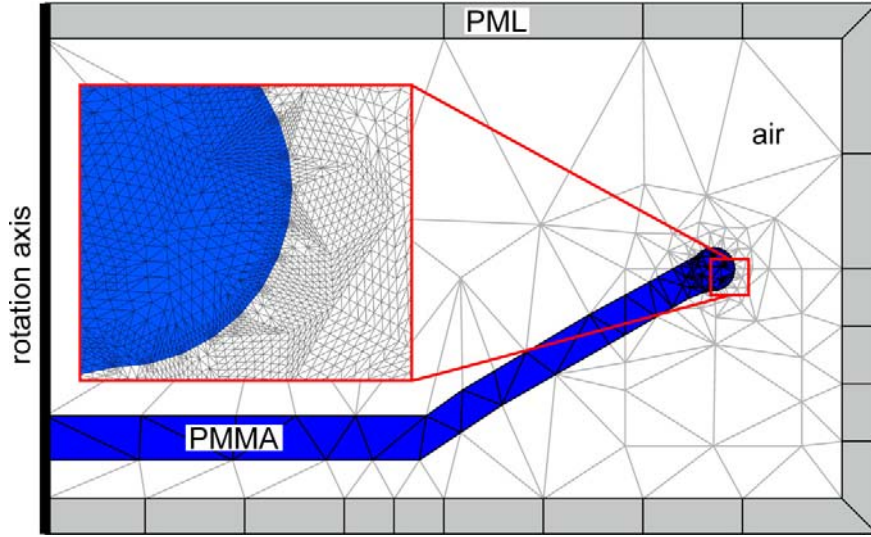


Figure 2.13: Two-dimensional cross-section in radial direction of the microgoblet after the initial triangulation of the computational domain. The left boundary is the rotation axis. The other boundaries are formed by perfectly matched layers (PML). The inset shows an enlarged section of the cavity boundary (marked red) after three adaptive refinement steps. The cavity-air interface has the densest number of triangles.

thus computed using cylindrical coordinates, which reduces the problem to two dimensions. A cross-section in radial direction of the microgoblet after triangulation of the computational domain is shown in Fig. 2.13. The left boundary in Fig. 2.13 is the rotation axis. The other boundaries are defined by so-called perfectly matched layers (PML). These layers allow for transparent boundary conditions and prevent artefacts of the finite computational area, e.g., back-reflection of energy, from influencing the solutions.

The electric fields on the triangulated computational domain were approximated by third order polynomials. This polynomial order was found to offer the best compromise between accuracy of the solutions, computation time and memory consumption. In order to further reduce computational costs, an adaptive mesh refinement technique is incorporated in the software. This means that the mesh is refined in areas of the computational domain where the deviation of the electric field from the previously computed field is especially high. The accuracy of the simulation is thus increased successively. Further information about the algorithm and the adaptive mesh refinement technique has been presented by Pomplun et al. [67].

The computed resonance frequency has a complex value $\omega_{res} = \omega_{real} + i\omega_{imag}$. The real part of the resonance frequency denotes the temporal oscillation of the elec-

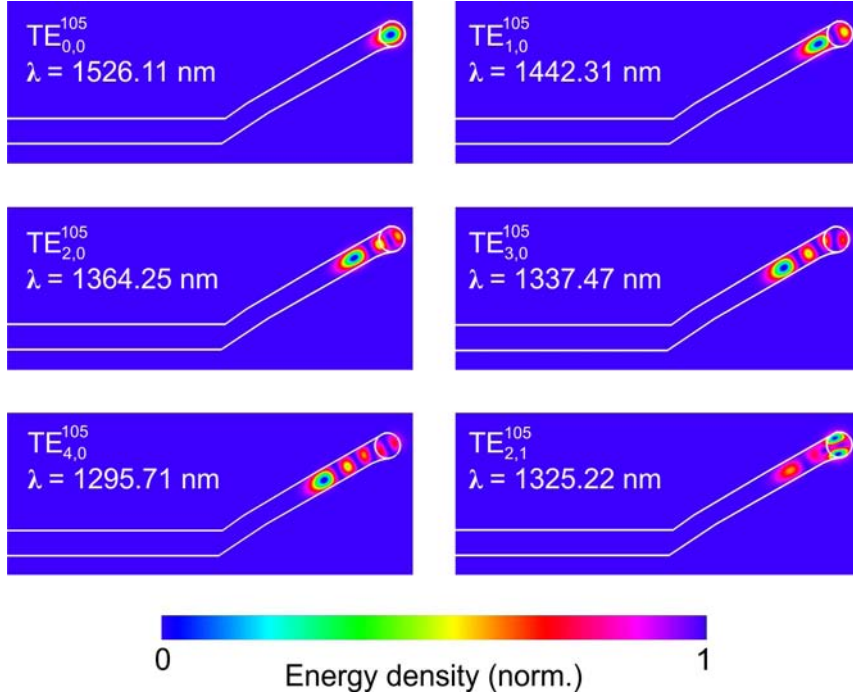


Figure 2.14: Simulated modes of a microgoblet. The intensity distribution and resonance wavelength of the WGMs were calculated with JCMResonance. The azimuthal mode number of the presented WGMs is $N_\phi = 105$ [23].

tromagnetic field. The imaginary part can be related to the temporal decay of the fields and was thus used to calculate the Q-factor of the resonances computed by finite element simulations:

$$Q = \frac{\omega_{real}}{2\omega_{imag}} \quad (2.19)$$

Further details of the computation algorithm for calculation of WGMs using JCM-Resonance can be found elsewhere [68, 69].

Simulation of WGMs in microgoblets

The exact geometry of goblet-like cavities used for the numerical modeling of WGMs was inferred from scanning electron micrographs of fabricated microgoblets. Figure 2.14 exemplarily shows the calculated intensity distributions of the TE_{N_ρ, N_z}^{105} modes in a goblet-shaped microresonator. In this case the maximum radius was

19.6 μm and the minimum radius (radius of the silicon pedestal) was 10.7 μm . The order of the modes was determined by manual review of the field strength of all three components of the electric field as well as the energy density. The electric field component with the highest field strength determines the polarization of the mode as defined in section 2.1.1. The spectral positions of the resonances in Fig. 2.14 are between 1290 nm and 1530 nm. The fundamental $\text{TE}_{0,0}^{105}$ mode is located at the rim of the cavity and has the highest resonance wavelength. As the radial order of the modes increases, the maximum of intensity moves towards the center of the goblet. In the analyzed wavelength region, only one higher order axial mode ($\text{TE}/\text{TM}_{2,1}^{105}$) for each polarization was found. This is accounted for by the dimension and the refractive index of the cavity. As the thickness of the resonator is in the order of the wavelength and the refractive index contrast between PMMA and air is only approximately 0.5, further higher axial modes are not confined in the cavity. The free spectral range was found to be 9.4 nm and perfectly fits to the measured free spectral range denoted in Fig 2.11 (a). Comparison of the simulation results with the measurements clearly indicates that the modal structure of microgoblets in the 1300 nm wavelength region is dominated by the fundamental mode and higher order radial modes of both polarizations [23].

At wavelengths around 630 nm, the number of modes in the axial direction was found to increase compared to the infra-red wavelength region due to a shorter wavelength. In addition to a larger number of modes, the free spectral range changed to a value of 1.9 nm, which is in good agreement with the experimentally measured value obtained from tapered optical fiber coupling (compare Fig. 2.12 (a)).

2.3 Summary and conclusions

In this chapter, microgoblet resonators were introduced as a type of optical microcavity which supports whispering-gallery modes. The surface-tension induced, goblet-shaped cavity geometry was fabricated by thermal reflow of PMMA microdisks standing on silicon pedestals. The reflow process resulted in a smooth cavity surface with a greatly reduced number of lithographic blemishes. Compared to resonators made of SiO_2 , the low glass-transition temperature of PMMA enabled a reflow at temperatures slightly above 100 $^\circ\text{C}$, which is around one order of magnitude lower compared to temperatures needed for reflow of SiO_2 and allows for large-scale fabrication of these polymeric devices. The optical properties of the passive on-chip microgoblets were characterized by tapered optical fiber coupling. The Q-factors of the PMMA cavities took on values as high as 3×10^6 at wavelengths around 1300 nm. The high optical quality of passive, polymeric microgoblet resona-

tors and the simple integration of gain medium within polymeric host matrices are ideal prerequisites for the development of on-chip lasers with low thresholds, which is presented in the next chapter.

Chapter 3

Low-threshold microgoblet dye lasers

For the development of lasers with low threshold, an efficient gain medium with high amplification has to be integrated within the resonator without deteriorating the quality of the cavity. Ideally, the gain medium is distributed homogeneously throughout the entire optical mode of the cavity to achieve a high modal gain. For polymeric resonators, organic laser dyes fulfill these requirements due to their good compatibility with polymeric host matrices and their high internal quantum efficiency. This makes dyes a suitable gain medium for integration within polymeric microgoblets.

The following chapter begins with a general discussion of the properties of dye molecules and their application as gain medium. For the development of microgoblet lasers, PMMA was doped with the dyes rhodamine 6G and pyrromethene 597, resulting in optically pumped microgoblet lasers emitting at wavelengths around 600 nm. The operation of these WGM lasers in aqueous environment allows for their application as label-free biosensors and the label-free detection of proteins is presented in the last section of this chapter.

3.1 Dye laser basics

Historically, the investigation of dyes as gain medium began in the 1960s shortly after the first experimental demonstration of a laser [70]. The first dye lasers were based on liquid solutions of dyes, which provides several advantages compared to solid-state lasers: The liquid can be easily cooled, bleached molecules can be exchanged

and the cost of the gain medium is relatively low compared to crystals, typically used for solid-state lasers. Furthermore, the broad gain spectrum enables tuning of the dye laser emission over a wide range of wavelengths [71]. Dye lasers can be operated either continuous-wave (cw) mode [72] or with ultra-short pulses [73].

Despite the above mentioned advantages of liquid dye lasers, a lot of effort has been made over the last years to incorporate dyes in solid-state host matrices, such as polymers. Solid-state dye lasers have the advantages of being non-volatile, non-toxic, mechanically stable and compact [74].

Two classes of dyes which are especially suitable for the incorporation in PMMA and possess a high efficiency are xanthene and pyrromethene (PM) [75]. Due to their advantageous properties, dyes from these two classes are investigated in this work for the realization of dye-doped microgoblet lasers. Before the experimental realization of the dye-doped polymeric microcavities is presented, the following section gives a general introduction to organic dyes and their application as gain medium in optically-pumped lasers.

3.1.1 Chemical structure of organic dyes

Strictly speaking, a dye is an organic compound, which has a high absorption in the visible part of the spectrum originating from several conjugated double bonds. Therefore, dyes belong to the class of unsaturated compounds [70]. Saturated molecules without double or triple bonds only absorb light at wavelengths below 160 nm. The energy of such photons is above the dissociation energy of most chemical bonds. Therefore, saturated hydrocarbons are not suitable as active medium in lasers. In a wider sense, the word dye encompasses all substances containing conjugated double bonds, which results in absorption of wavelengths above 200 nm [70].

In contrast to single bonds (σ bonds), double and triple bonds possess additional π electrons for binding. A simple illustration of covalent binding of π electrons is shown in Fig. 3.1, where the chemical structure of ethene is depicted. The molecular plane of ethene is formed by a σ bond of the hybridized sp^2 orbitals. The π bond resulting from the atomic p_z orbitals forms an electron cloud above and below the molecular plane. Like ethene, dye molecules are essentially planar and the π electrons of the carbon atoms typically form a charge cloud above and below the the molecular plane linked by σ bonds of the conjugated chain. An example for delocalized π -electron clouds of a simple cyanine dye is depicted in Fig. 3.2. These delocalized π electrons determine the optical transitions of the dye molecule. This part of the molecule is referred to as chromophore and can be described by a simplified quantum-mechanical model, which is discussed in the next section.

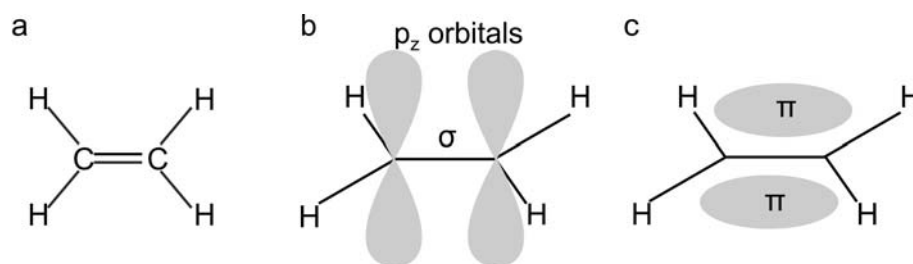


Figure 3.1: (a) Chemical structure of ethene. (b) The molecular plane is formed by a σ bond of the hybridized sp^2 orbitals. (c) The π bond resulting from the p_z orbitals forms an electron cloud above and below the molecular plane [76].

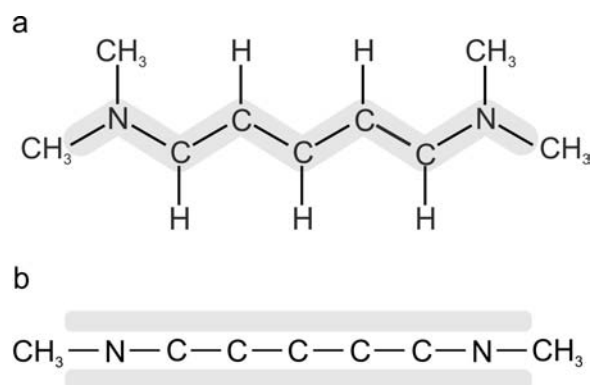


Figure 3.2: Clouds of delocalized π electrons (marked grey) in a cyanine dye seen from (a) above the molecular plane and (b) from the side. (Adapted from [70].)

3.1.2 Free-electron model

The delocalized π electrons are assumed to move freely within their planar distributions above and below the molecular plane. The movement is only limited by the repulsive potential of the methyl groups at the end of the dye chain. The electrostatic potential of a single π electron moving in the field of the molecule may be considered as constant. The electronic states of a dye molecule can therefore be approximated to first order by those of freely moving electrons in a potential well, shown in Fig. 3.3. Assuming that the conjugated chain has a length L , the energy of the n th eigenstate of electrons in a dye molecule E_n is given by

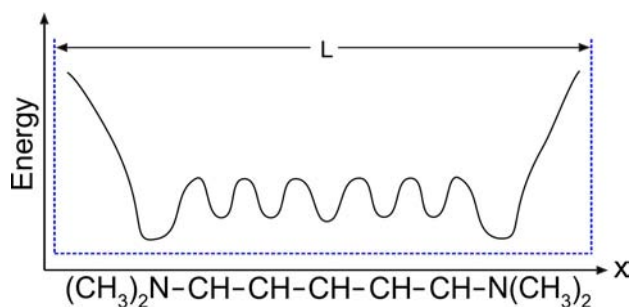


Figure 3.3: Potential energy of a π electron moving along the carbon chain of cyanine. The energy states of π electrons are approximated by a model of freely moving electrons in a potential well (dashed blue line) of length L , which is given by the length of the carbon chain. [70].

$$E_n = \frac{h^2 n^2}{8mL^2} \quad (3.1)$$

The mass of the electron is denoted as m , Planck's constant is h and the quantum number n gives the number of antinodes of the eigenfunction along the chain. Each state can be occupied by two electrons with opposite spins (Pauli principle). The total spin of the molecular state is therefore $S = 0$. The molecule is in the singlet state S_0 . For a dye in the ground state with $2N$ electrons, the lowest N states are filled¹. The smallest energy needed to excite the molecule is given by the energy difference between the highest occupied state E_N and the lowest unoccupied energy state E_{N+1} . With equation 3.1, this energy can be calculated as

$$\Delta E_{min} = E_{N+1} - E_N = \frac{h^2}{8mL^2}(2N + 1) \quad (3.2)$$

This equation shows that, in first approximation, the spectral position of the absorption band of dyes is given by the chain length and the number of π electrons. This model is relatively exact for large dye molecules. For smaller molecules, further electron correlations have to be included in the free-electron model [70].

3.1.3 Optical transitions in dye molecules

The transition from the ground state S_0 to the next highest energy state S_1 of the molecule, e.g., by absorption of a photon, occurs by an electron transition from

¹ N is an odd number for stable molecules. Unpaired electron states only occur in highly reactive radicals.

the bonding π orbital to the anti-bonding π^* orbital, resulting in a change of the electron densities, and is accompanied by vibrations of the molecule. These electronic transitions are instantaneous in comparison to time scales of vibrations of the nuclei. The approximation that an electronic transition occurs without changes of the nuclei positions is called Franck-Condon principle. The transitions between S_0 and S_1 are therefore represented by vertical lines in diagrams where the potential energy of the electronic molecular state (often approximated as Morse potential) is plotted as function of the nuclei distance (Fig. 3.4 (a)). The horizontal lines in the Morse potential represent the vibrational states, which are equidistant around the equilibrium point due to the approximately quadratic potential in this region. A transition is more likely to occur for overlapping wavefunctions of the vibrational states of the initial and final state and can be calculated using quantum mechanics by evaluation of the overlap integral of these wavefunctions. After excitation into a higher singlet level (S_1 or higher), the molecule undergoes a radiationless relaxation within picoseconds into the $S_{1,\nu'=0}$ level. From this level with a lifetime of nanoseconds, a transition into the state $S_{0,\nu\neq 0}$ under spontaneous emission of a photon (fluorescence) can occur, followed by a further non-radiative relaxation into the $S_{0,\nu=0}$ state. The large number of atoms in a dye gives rise to a large number of vibration modes. The absorption and emission spectra of dye molecules are therefore typically broadened by several tens of nanometers, as depicted in Fig. 3.4 (b). The separation between the maximum of the absorption and of the emission spectrum is often referred to as Stokes shift.

In addition to the above discussed singlet state with $S = 0$, triplet states T with parallel electron spin ($S = 1$) exist for all excited electronic states. Each triplet state is located at a slightly lower energy than the corresponding singlet state and can not be directly excited with electromagnetic radiation from the singlet ground state due to the selection rule $\Delta S = 0$. Hence, singlet-singlet as well as triplet-triplet transitions are allowed, while optical singlet-triplet transitions are forbidden [77]. Nevertheless, spin-orbit coupling enables the non-radiative transition from the singlet to the triplet manifold. This process is called intersystem crossing (ISC) and is slow (about 100 ns) compared to the spontaneous emission lifetime. This short spontaneous emission lifetime (several nanoseconds) of dyes can be explained by the very large dipole matrix element ($\approx eL$) originating from the large spatial delocalization of π electrons.

The π -electron distribution was also found to play a major role for ISC. It was empirically discovered that for π -electron distributions where the electrons of the chromophore can make a loop the triplet yield is higher than for distributions where the loop is blocked [70]. This could be explained by an increased orbital magnetic moment caused by circulating electrons, which increases the spin-orbit coupling. A

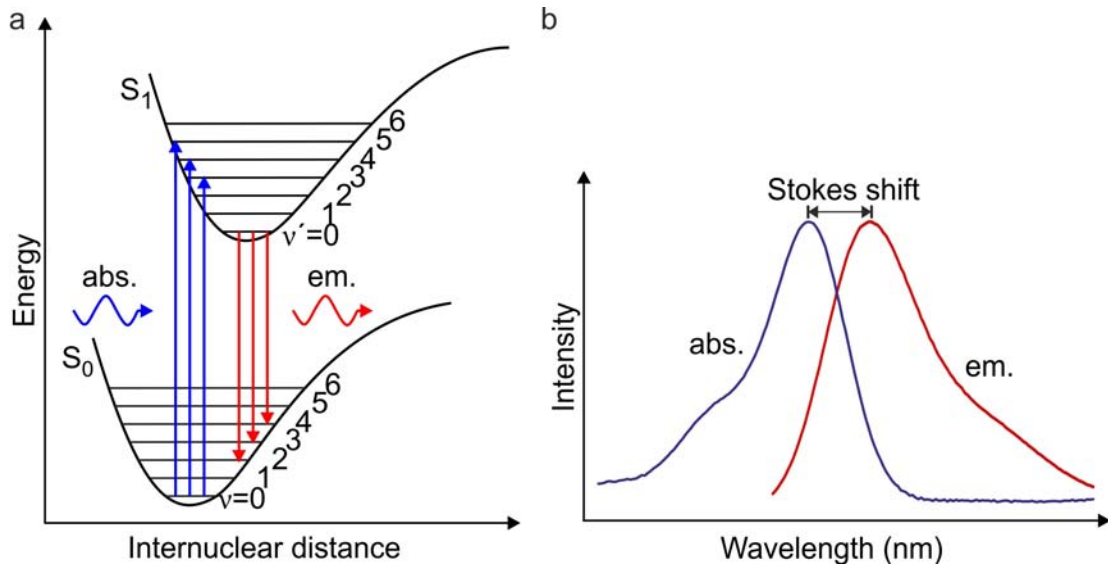


Figure 3.4: (a) Potential energy of the S_0 and S_1 state of a molecule as function of the internuclear distance. The vibronic levels are denoted as ν and ν' [77]. The transitions given by the Franck-Condon principle are indicated as vertical arrows, where the absorption of a photon is marked in blue and the emission is marked in red. (b) Resulting absorption and emission spectrum of dye molecules. The separation between the maxima is called Stokes shift.

second type of structural feature of dye molecules leading to increased spin-orbit coupling was found in chromophores where elements were substituted with heavy atoms [70].

Triplet states are extremely long-lived with lifetimes up to 100 μs due to the forbidden spin-flip transition to the ground state [77]. The radiative transition from T_1 to S_0 is often referred to as phosphorescence. The above discussed optical transitions and conversion processes between the energy states of dyes are summarized and visualized in Fig. 3.5. The application of dyes as four-level gain medium in optically pumped lasers is discussed in the following.

3.1.4 Dyes as gain medium

The essential building blocks of a laser (acronym for *light amplification of by stimulated emission of radiation*) are a light amplifying medium, a resonator for optical feedback and a pump to achieve population inversion of the gain medium. Population inversion via optical pumping is only possible in active materials based on

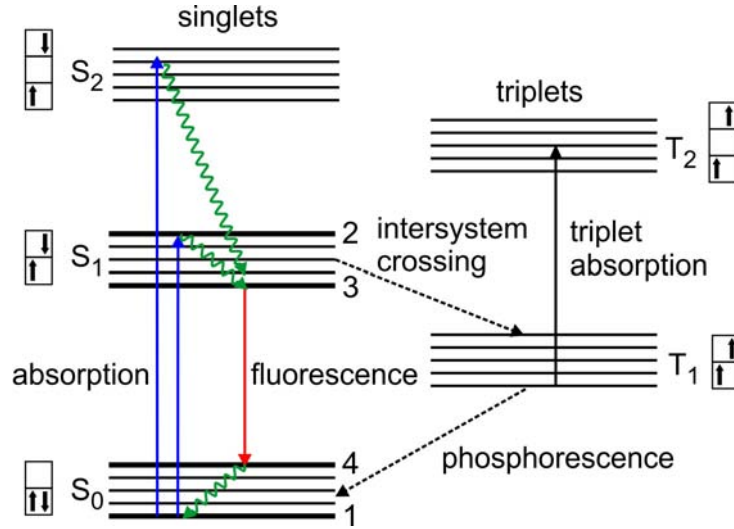


Figure 3.5: Energy diagram of the important states with spin configuration and processes involved in optical transitions of dye molecules. Solid arrows mark radiative transitions and broken lines indicate spin-forbidden transitions. Internal conversion processes are marked by green zig-zag lines. The four states involved in lasing are marked bold and numbered from one to four.

emitters with more than two energy levels, such as three- or four-level systems. Four-level gain media are especially efficient, as already the absorption of a single photon leads to an inverted population of this emitter. Laser dyes can be treated as four-level systems due to the vibrationally broadened electronic states. The four levels of a dye molecule involved in lasing are numbered in Fig. 3.5 from one to four². In principle, population inversion could also occur between the levels involved in phosphorescence, although lasing from these levels has not been reported yet due to losses arising from triplet-triplet absorption [70]. The non-radiative relaxation processes of the singlet states are much faster than the radiative transitions, which leads to an efficient build-up of an inverted population, resulting from accumulation of dye molecules in level 3 ($S_{1,\nu'=0}$) and quick depletion of level 4 with $S_{0,\nu>0}$. It is important to note that the energy difference between vibrational levels is around 125 meV, which is considerably higher than $k_B T \approx 25$ meV at room temperature. The higher vibronic levels of the singlet ground state are therefore not occupied at room temperature.

²Level 2 and level 4 in Fig. 3.5 can be any of the singlet states with $\nu' > 0$ and $\nu > 0$, respectively (see Fig 3.4).

Oscillation condition of dye lasers

For lasing operation, an additional prerequisite of the gain medium besides the correct lifetimes of the energy states is a high probability for stimulated emission. This is expressed in the following by the stimulated emission cross-section $\sigma_e(\lambda)$. This cross-section can be calculated by the following equation [70, 78]:

$$\sigma_e(\lambda) = \frac{\lambda^4 f(\lambda) \Phi_f}{8\pi c n^2 \tau} \quad (3.3)$$

The normalized photoluminescence (PL) spectrum is denoted as $f(\lambda)$ and the internal quantum efficiency is Φ_f . The vacuum speed of light is c , n is the refractive index of the gain medium and τ is the fluorescence lifetime of the transition. From equation 3.3 it can be seen that the stimulated emission cross-section is essentially governed by the PL spectrum and is several tens of nanometers broad for typical laser dyes [70]. The values of σ_e for dyes are in the order of 10^{-16} , which is several orders of magnitude higher than in rare-earth-doped crystals [77] and comparable to inorganic semiconductors, such as gallium arsenide [79].

In order to derive a simple oscillation condition for dye lasers, losses of the cavity and the self-absorption of the dye have to be considered in addition to the cross-section for stimulated emission introduced in equation 3.3. A dye molecule can be modeled as a four-level system, where n_1 is the number density (per unit volume) of molecules in the first excited singlet state and n_0 is the number density of molecules in the ground singlet state. The total number of dye molecules per unit volume is given by $n_t = n_0 + n_1$. To achieve lasing in a cavity with Q-factor Q including dyes as active material, the round-trip gain must overcome the total round-trip losses at the lasing wavelength λ [78]:

$$n_1 \sigma_e(\lambda) \geq \frac{2\pi n}{\lambda Q} + n_0 \sigma_a(\lambda) \quad (3.4)$$

The cross-section for absorption is denoted as $\sigma_a(\lambda)$. A minimum fraction of molecules $\gamma = n_1/n_t$ has to be excited to fulfill equation 3.4, which can be rewritten as [80]

$$\gamma(\lambda) \geq \frac{2\pi n / (\lambda Q n_t) + \sigma_a(\lambda)}{\sigma_a(\lambda) + \sigma_e(\lambda)} \quad (3.5)$$

The right side of equation 3.5 shows that the lasing threshold of dye lasers mainly depends on the Q-factor and the number density of dyes in the cavity. The lasing

occurs at wavelengths where $\gamma(\lambda)$ is minimal and can be calculated by inserting the cross-sections of absorption and stimulated emission into equation 3.5. The fact that a higher dye concentration results in a lower lasing threshold as predicted by equation 3.5 is somewhat misleading due to increased dye aggregation occurring at high concentrations, which can lead to fluorescence quenching. An overview of the most common degradation effects in dyes is given in the following section.

Influence of triplets and degradation mechanisms in dyes

The above discussed simple model of dyes as a four-level system neglects the influence of triplet states, which can be formed from excited singlet states by intersystem crossing (see Fig. 3.5). Triplet states reduce the lasing efficiency due to several different reasons. The most obvious reason is the depopulation of the upper lasing level $S_{1,\nu=0}$, which reduces the population inversion and thus the optical gain. Another loss mechanism associated with triplet formation is the absorption of photons contributing to stimulated emission by excitation of higher triplet states ($T_1 \rightarrow T_n$). The wavelength-dependent absorption cross-section of triplet states in typical laser dyes have significant spectral overlap with the stimulated emission cross-section and is around one order of magnitude smaller than σ_e [81]. Thus, for threshold reduction the amount of generated triplet states should be as low as possible. The population of triplet states can be held at an extremely low level by using a pulsed pump light. A plausible approximation for the length of pump pulses in time to avoid triplet formation can be derived by comparing the relevant time scale of the pump pulse with the rate of intersystem crossing. If the pumping light energy density reaches lasing threshold in a rise time which is small compared to the reciprocal intersystem crossing rate $k_{ST}^{-1} = 100$ ns of dyes [82], stimulated emission occurs faster than the formation of triplets [70]. Typical risetimes of pump pulses should therefore be in the order of several nanoseconds [25, 83] or shorter [84].

A further negative effect originating from triplet formation is the reaction of excited triplet states with oxygen in the environment. This photo-oxidation process leads to irreversible quenching of dyes and is even more pronounced at higher temperatures due to an increased mobility of the dye. The active material is heated during the optical pumping by non-radiative relaxation processes within the dye as discussed in section 3.1.3 [82]. This excess energy after excitation is dissipated as heat to the surrounding of the dye. For lasers with liquid dye solutions, this problem is overcome by continuously exchanging the dye solution in the pump beam. This can be performed either actively, using a fluidic pump [85], or, alternatively, by using diffusion for the exchange of dye molecules, which has the advantage of being a passive process and doesn't require an active exchange of the solution via fluidic

pumps [86]. In dye-doped polymers, dissipation of heat has to be as efficient as possible to obtain high operational lifetime. For this, the dye molecules have to be stably embedded in polymeric host matrices [74,87], e.g., by covalent linking of dye molecules to the polymer chain [88].

Further degradation of dyes occurs through formation of aggregates, such as dimers. These lower the quantum yield Φ_f , which is given by

$$\Phi_f = \frac{\tau}{\tau_{sp}} \quad (3.6)$$

The total lifetime of the S_1 state is τ and the spontaneous emission lifetime of the S_1 state is τ_{sp} . These lifetimes are connected by the relation [77]

$$\frac{1}{\tau} = \frac{1}{\tau_{sp}} + k_{ST} \quad (3.7)$$

Due to the short spontaneous emission lifetime resulting from the large oscillator strength of dyes, the total lifetime of the S_1 state is approximately given by τ_{sp} . The quantum yield of diluted dye solutions is therefore nearly unity [89]. If dyes are prepared as densely packed solid films or in solutions with dye concentrations above 10^{-3} mol/l, aggregation of dye molecules leads to severe fluorescence quenching [82,90]. The quantum yield Φ_f drops to values below 20% for dye concentrations above 10^{-2} mol/l [90]. Therefore, a separation of the dye molecules by a polymeric host matrix is important to prevent aggregation in order to obtain a high quantum yield.

3.2 Dye-doped microgoblet lasers

For the realization of microgoblet dye lasers, the laser dyes rhodamine 6G (rh6G) and pyromethene 597 (PM597) were doped into the PMMA host matrix. In the following section, first the doping process of PMMA with rh6G as well as the optical absorption and emission properties of the dye-doped polymer are discussed. Afterwards, the lasing properties, such as the concentration dependent lasing threshold and emission spectrum, of dye-doped microgoblets are presented.

3.2.1 Rhodamine-doped PMMA

The laser dye rhodamine 6G³ (Radiant Dyes) is not directly soluble in the solvent of PMMA (anisole), used for the fabrication of goblet resonators (section 2.2.1). Therefore, the dye is first dissolved in ethanol and subsequently added to the resist. To ensure a homogeneous distribution of dye molecules in the resist, the solution is stirred for 24 hours. Dye concentrations were chosen to be low enough to ensure that no non-radiative recombination processes from dye aggregation occur.

Absorption and fluorescence measurements of rh6G-doped PMMA films were performed to characterize the optical properties of rh6G molecules in the PMMA matrix and to determine the absorption and stimulated emission cross-section. For this, dye-doped PMMA was spin-coated onto cover slips. To ensure good comparability with the emission properties of dye-doped goblets, the parameters for the fabrication of the films with a thickness around 1 μm were the same as for the fabrication of goblet resonators (see section 2.2.1). The measurement of the absorption between 400 and 700 nm was carried out with the spectrophotometer Cary 100 (Varian) by measuring the intensity I_t transmitted through the 1 μm -thick film and comparing it to the incoming intensity I_0 . The absorbance or optical density A_λ of an absorbing medium with molar concentration C_0 and thickness d can then be determined by the following equation:

$$A_\lambda = -\log(I_t/I_0) = \varepsilon(\lambda)C_0d \quad (3.8)$$

The molar extinction coefficient is denoted as ε . As reference signal, the absorbance of a cover slip with a 1 μm -thick film of un-doped PMMA on a cover slip was used to eliminate the influence of the substrate and PMMA matrix. To determine the molar extinction coefficient from equation 3.8 from the measured absorbance, the concentration of the dye molecules in the spin-coated film has to be known. For this, it was assumed that 95 % of the solvents evaporate during baking of the film after spin-coating. The absorption cross-section σ_a is calculated by [70]

$$\sigma_a(\lambda) = 3.85 \times 10^{-21} \varepsilon(\lambda) \quad (3.9)$$

The calculated absorption cross-section σ_a of rhodamine 6G in PMMA, which was determined with a sample containing a dye concentration of 3 $\mu\text{mol/g}$ solid content, is depicted in Fig. 3.6 (b).

The fluorescence spectrum was measured using the fluorospectrometer Fluorolog-3

³The chemical structure of rhodamine 6G is depicted in Fig. 3.6 (a).

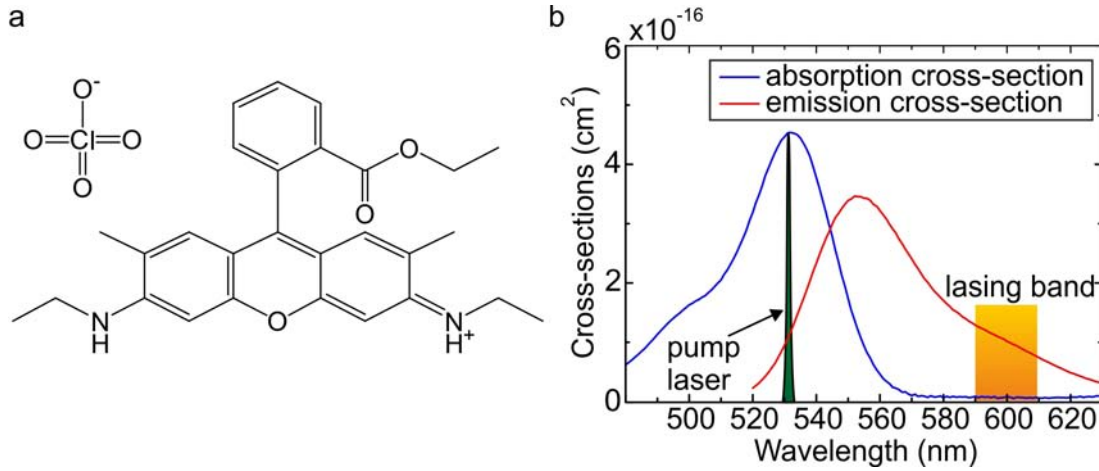


Figure 3.6: (a) Chemical structure of rhodamine 6G perchlorate [91]. (b) Absorption and emission cross-section of rhodamine 6G-doped PMMA. Furthermore, pump wavelength and lasing band of the microgoblet lasers are indicated [25,92].

(Horiba Jobin Yvon). The stimulated emission cross-section was calculated according to equation 3.3 by normalizing the fluorescence spectrum ($\int F(\lambda)d\lambda = 1$). For rhodamine 6G in PMMA, a quantum yield of $\Phi_f = 0.83$ and a spontaneous emission lifetime of $\tau_{sp} = 4$ ns were reported in literature [91]. The resulting stimulated emission cross-section $\sigma_e(\lambda)$ is depicted in Fig. 3.6 (b). The overall shape of the curves for σ_a and σ_e in Fig. 3.6 (b) are in good agreement with reports in literature [70,91]. The Stokes shift for rh6G inferred from Fig. 3.6 (b) is 21 nm. The strongest absorption occurs at $\lambda = 532$ nm, providing ideal pumping conditions at this wavelength for microgoblet lasers fabricated with rh6G-doped PMMA. Also indicated in Fig. 3.6 (b) is the lasing band at wavelengths between 585 and 610 nm, which is observed for these microgoblet lasers. The lasing does not occur at the maximum of σ_e due to the self-absorption of the dye in this region. A detailed discussion of the emission properties of microgoblet lasers is presented in the following section.

3.2.2 Rhodamine-doped microgoblets

Lithographic structuring of rh6G-doped microgoblets was performed with identical process parameters as discussed in section 2.2.1. Rhodamine molecules withstand temperatures around 140 °C without thermal destruction and bleaching [93]. Therefore, the thermal reflow step resulting in the formation of goblet-like resonators has no influence on the functionality of the dye.

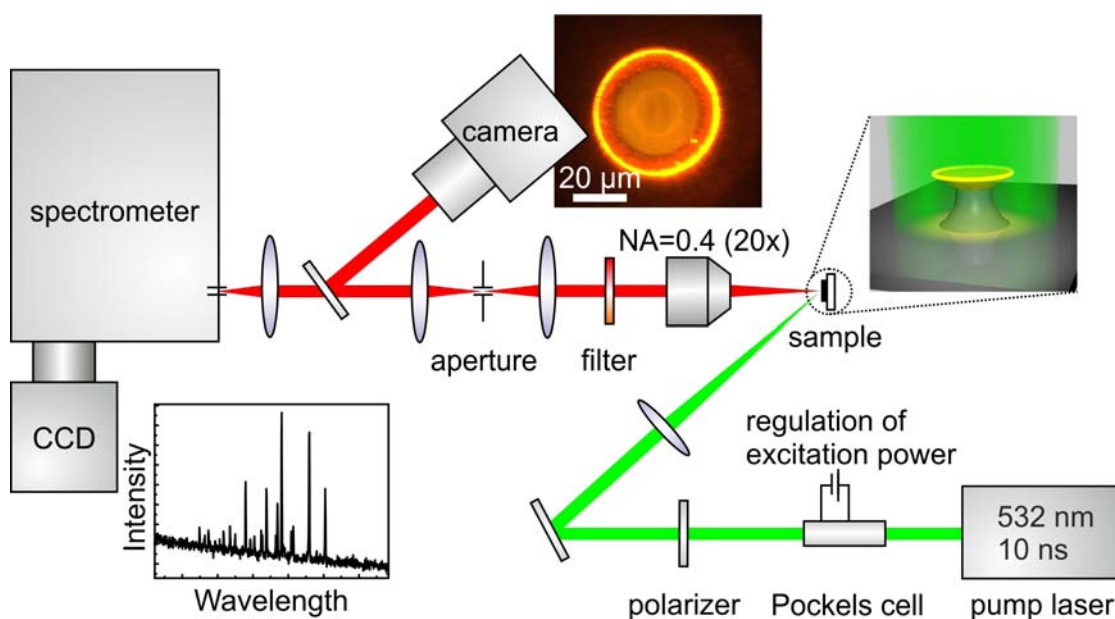


Figure 3.7: Microphotoluminescence (μ PL) setup for characterization of lasing in dye-doped microgoblets. The pump-laser beam is focused onto the sample at an angle of 45° . Emission from the sample is collected by a microscope objective and either monitored on a camera or spectrally analyzed on a CCD camera attached to a spectrometer.

Free-space excitation of microgoblet lasers

In order to invert the population of the dye ensemble along the circumference of the resonator where the WGMs propagate, the pump light can be coupled into the microcavity via tapered optical fiber coupling (see section 2.2.3). This provides for a very efficient way to couple the pump light into the resonator and enables low threshold lasing with efficient extraction of lasing modes out of the cavity via tapered fiber [94]. Despite these advantages of tapered optical fiber coupling, for practical applications free-space excitation of lasing is preferred, as alignment of the pump beam does not require the high positioning accuracy necessary for tapered-fiber alignment. The degradation of tapered fibers is a further drawback of this method. Free-space pumping results in simpler setups, lower costs and increased system robustness [95], especially for lasing operation in aqueous environments. Therefore, for characterization of the lasing in WGMs, a free-space excitation setup was used to optically pump the dye-doped microgoblets.

The microcavities were pumped with 10 ns pulses of a frequency-doubled neodymium-doped yttrium orthovanadate (Nd:YVO_4) laser at a pump wavelength of 532 nm and a repetition rate of 20 Hz. Excitation pulses with lengths shorter than 100 ns

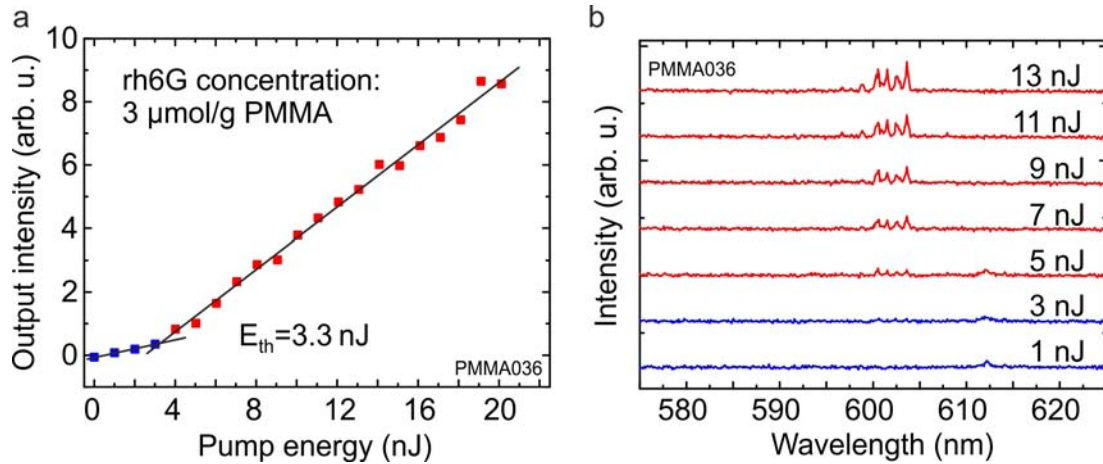


Figure 3.8: Lasing threshold and emission spectra of rhodamine 6G-doped microgoblet lasers. (a) Input-output curve of a microgoblet laser with a dye concentration of 3 $\mu\text{mol/g}$ solid PMMA. The lasing threshold is 3.3 nJ. Data points below and above the threshold are marked blue and red, respectively. (b) Emission spectra corresponding to data points in (a), where the spectra below and above the threshold are indicated in blue and red color.

prevent triplet formation in the dye molecules, as discussed in section 3.1.4. The pump pulses were focused onto the sample at an incident angle of 45° with respect to the substrate normal using a lens. The excitation power was varied with a Pockels cell in combination with a linear polarizer. The pump spot was chosen to have a diameter of approximately 100 μm on the sample surface in order to homogeneously pump the microgoblets. The output emission was collected perpendicular to the resonator with a microscope objective (NA = 0.4, 20x) and either imaged on a camera or analyzed in a spectrometer equipped with a CCD (charged coupled device) camera⁴. The overall spectral resolution was 60 pm (grating with 1200 lines/mm) or 30 pm (grating with 2400 lines/mm). A schematic illustration of the setup for free-space excitation is depicted in Fig. 3.7.

Lasing properties of dye-doped microgoblets⁵

By variation of the excitation energy of the pump laser, the output of the microcavity lasers as a function of the pump energy was recorded. A characteristic input-output

⁴Alternatively, the emission was collected in the plane of the resonator by a multi-mode fiber and directly sent to the spectrometer [25].

⁵The results presented in this section have been partly published in [25] and [92].

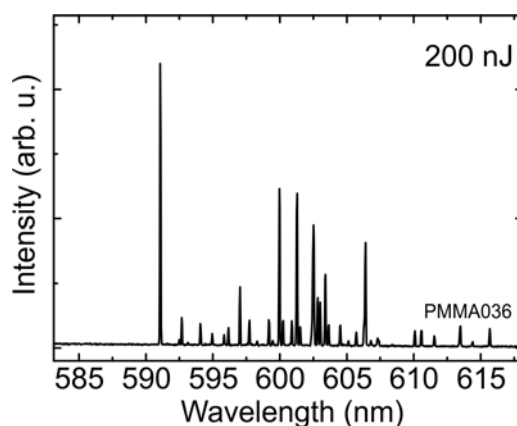


Figure 3.9: Lasing spectrum of a rh6G-doped microgoblet recorded at a pump energy of 200 nJ, far above the lasing threshold.

curve of a microgoblet dye laser with a rhodamine 6G concentration of 3 $\mu\text{mol/g}$ solid PMMA is shown in Fig. 3.8 (a). The output intensity at a certain pump energy was determined by integrating the intensity of a single lasing mode⁶. The onset of lasing was inferred from the superlinear increase of the intensity due to the transition from spontaneous to stimulated emission, resulting in a kink of the output emission. The lasing threshold E_{th} in Fig. 3.8 (a) was found to be 3.3 nJ. The corresponding lasing spectra for increasing pump energy below and above the threshold are depicted in Fig. 3.8 (b) by the blue and red curves, respectively. For pump energies above the threshold, several spectrally narrow lasing peaks appear in the spectrum. The broad gain spectrum and the small free spectral range at wavelengths around 600 nm render the microgoblet lasers multimode. A high resolution spectrum recorded at a pump energy far above the threshold (200 nJ) is shown in Fig. 3.9. The spectrum shows that lasing occurs in a multitude of cavity modes. The spectral distance between the lasing peaks is well below the free spectral range of 1.9 nm. This shows that at wavelengths around 600 nm – in addition to the fundamental modes – several higher order cavity modes in axial and radial direction of both polarizations are well confined in the microgoblets and contribute to the lasing spectrum.

To investigate the effect of dye concentration on the lasing properties, such as lasing threshold and emission spectrum, resonators containing four different concentrations of rh6G in PMMA with 1, 3, 6 and 16 $\mu\text{mol/g}$ solid PMMA were compared and the results are discussed in the following paragraphs.

The lasing thresholds of microgoblets with the four different dye concentrations are depicted in Fig. 3.10 (a), where an optimum dye concentration for low-threshold las-

⁶For this, typically the lasing mode with the lowest threshold was used.

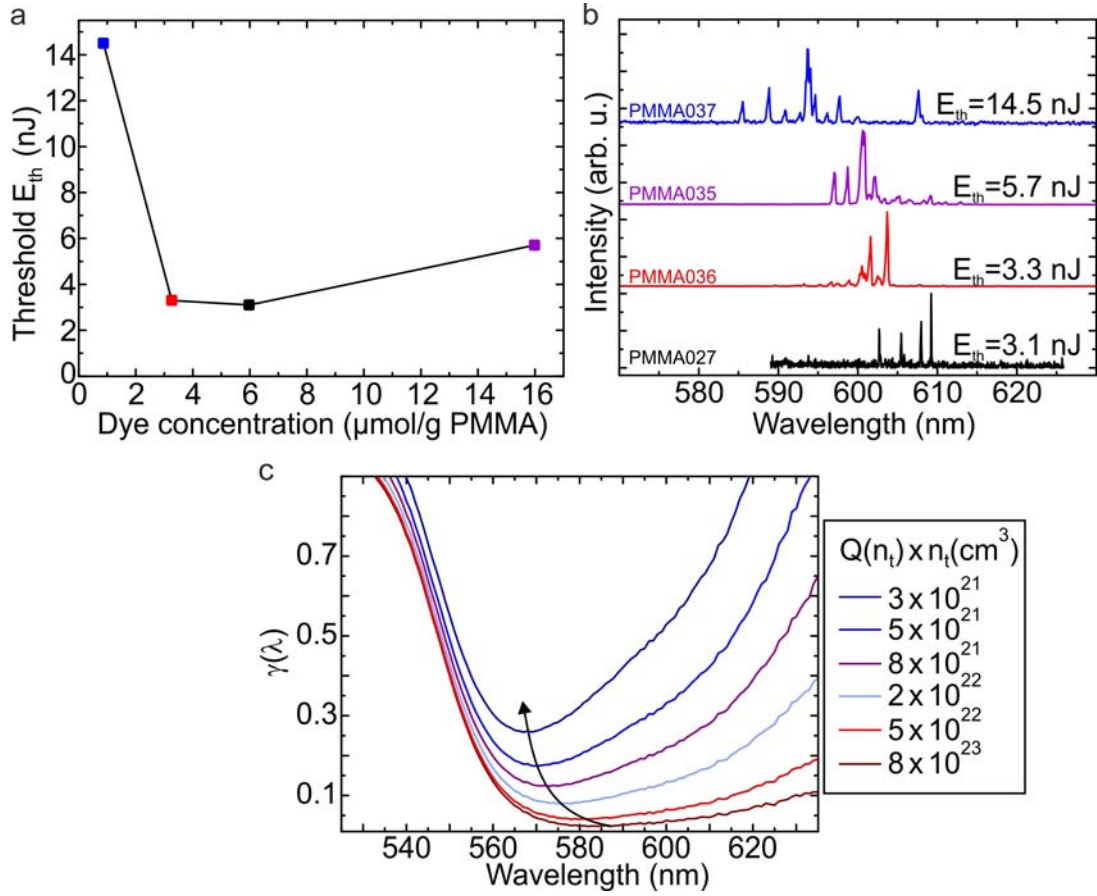


Figure 3.10: (a) Lasing thresholds and (b) emission spectra of the lasers strongly depend on the dye concentration. The emission spectra shift to shorter wavelengths for increasing lasing threshold, which can be explained by the theoretical dye laser model (equation 3.5). (c) Minimum fraction $\gamma(\lambda)$ of dye molecules in the S_1 state to achieve lasing for different values of $Q(n_t) \times n_t$ [92].

ing of about 3 to 6 $\mu\text{mol/g}$ solid PMMA can be inferred [92]. For higher and lower dye concentrations, the threshold increased to $E_{th} = 5.7$ nJ and $E_{th} = 14.5$ nJ, respectively. The increasing threshold with higher dye concentration can be explained by three effects. More dye molecules in the active region decrease the Q-factor of the cavity due to larger scattering or absorption losses and lead to an increased transparency condition (net gain equal to zero) because the threshold is proportional to the number of molecules in the active volume [94]. Furthermore, reduction in the internal quantum yield of dye molecules due to stronger dye aggregation at higher concentrations [90] can result in higher thresholds. The main reasons for the increase of the threshold at lower dye concentrations are the reduced absorption of pump energy in the 1 μm thick cavities using the free-space pumping scheme, along

with a smaller amount of total gain due to the reduced number of dye molecules [92].

Not only the lasing threshold but also the spectral laser emission was influenced by the dye concentration. Figure 3.10 (b) shows normalized emission spectra of microgoblets above the lasing threshold for the four investigated dye concentrations, where the corresponding lasing threshold of each spectrum is denoted on the right hand side. With increasing threshold the maximum of the gain envelope shifted to shorter wavelengths.

This effect can be explained qualitatively using the standard model of four-level dye lasing in a cavity, which was introduced in section 3.1.4. The model explains the dependency of the threshold – represented by $\gamma(\lambda)$ – for varying values of the total number density of dye molecules n_t and the cavity Q-factor (equation 3.5). In the regime, where losses due to surface scattering and absorption of the passive cavity are negligible, the quality factor $Q(n_t)$ at the lasing wavelengths is assumed to be limited by absorption/scattering losses caused by dye molecules and is therefore concentration dependent. For lower concentrations or lower Q-factors, $\gamma(\lambda)$ takes on higher values according to equation 3.5, indicating a higher lasing threshold. By inserting the measured cross-sections $\sigma_a(\lambda)$ and $\sigma_e(\lambda)$ into equation 3.5, the effect of Q-factor and dye concentration on the lasing wavelength can be studied. In Fig. 3.10 (c), $\gamma(\lambda)$ is plotted for different values of $Q(n_t) \times n_t$. Lower Q-factors or dye densities cause a shift of the optimum laser wavelength (the minimum of $\gamma(\lambda)$) to shorter wavelengths [78, 80]. Therefore, a strong decrease in Q-factor due to high dye concentration leads to a higher laser threshold and a blue-shifted emission spectrum. This effect can be observed in Fig. 3.10 (b), where the maximum of the laser spectrum of the cavity with highest dye concentration (purple curve) was clearly blue-shifted with respect to the spectra at lower concentrations and lower thresholds (red and black curves). For the sample with the lowest dye concentration and highest threshold (blue curve), the spectrum was seen to shift even further towards shorter wavelengths due to a very low number density n_t resulting in a lower $(Q(n_t) \times n_t)$ -factor compared to the other concentrations.

Although low lasing thresholds in the order of several nanojoule observed with rhodamine 6G as gain medium in PMMA microgoblets are a highly promising feature due to the possibility of using compact pump lasers, such as laser diodes [96], utilization of this type of dye also comprises several disadvantages. One main problem of rhodamine is the degradation due to photo-oxidation of the dye, resulting in a low operation lifetime, which is typically in the order of 10^3 - 10^5 pump pulses for commercially available rhodamine 6G in PMMA [97]. Due to this major drawback, the dye pyrromethene 597 as an alternative to rhodamine was integrated within the microgoblets. The optical properties of PM597-doped microgoblet lasers are presented in the following.

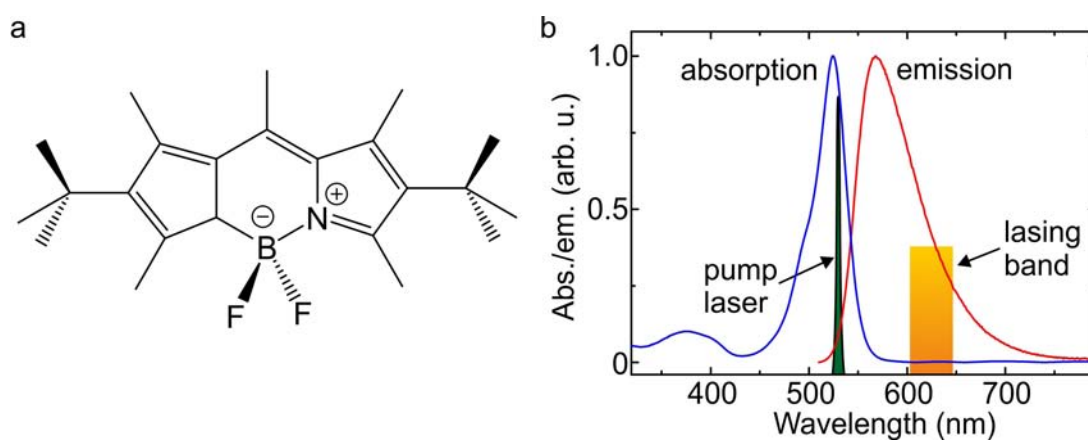


Figure 3.11: (a) Chemical structure of pyrromethene 597 [99]. (b) Normalized absorption and emission spectrum of PM597-doped PMMA.

3.2.3 Pyrromethene-doped microgoblets

Pyrromethenes (PM) are a laser dye family, which has been developed and investigated since the end of the 1980s. These dyes emit in the green-yellow and red part of the visible electromagnetic spectrum [98] with a high molar absorption coefficient (around $10^5 \text{ M}^{-1} \text{ cm}^{-1}$) and a near unity fluorescence quantum yield [99]. Compared to rhodamine, pyrromethene dyes have an improved laser performance due to three main reasons: (1) lower triplet-triplet absorption within the emission band of the S_1 state [100]; (2) lower tendency to self-aggregate in organic solvents, avoiding fluorescence quenching of the monomer emission; and (3) higher photo-stability, which improves the lifetime of the laser action. Owing to these advantageous properties, PM dyes have been widely studied and their successful incorporation into different solid matrices, e.g., polymers, sol-gels, etc., has been demonstrated [99].

From the PM family, the dye PM597⁷ was chosen for integration in PMMA microgoblets, due to its displaying an absorption band almost identical to that of rhodamine 6G. This enables efficient optical excitation with a pump laser at a wavelength of 532 nm. An advantage for preparation of PM597-doped PMMA compared to the doping of PMMA with rhodamine is the solubility of PM597 in anisole. Therefore, an additional solvent before admixture to PMMA was not needed and the dye was directly dissolved in the photoresist. Measurements of the absorption and emission spectrum of a 1 μm -thick PM597-doped PMMA film were performed analog to the above discussed case of rh6G. An example of a normalized absorp-

⁷The chemical structure of pyrromethene 597 is depicted in Fig. 3.11 (a).

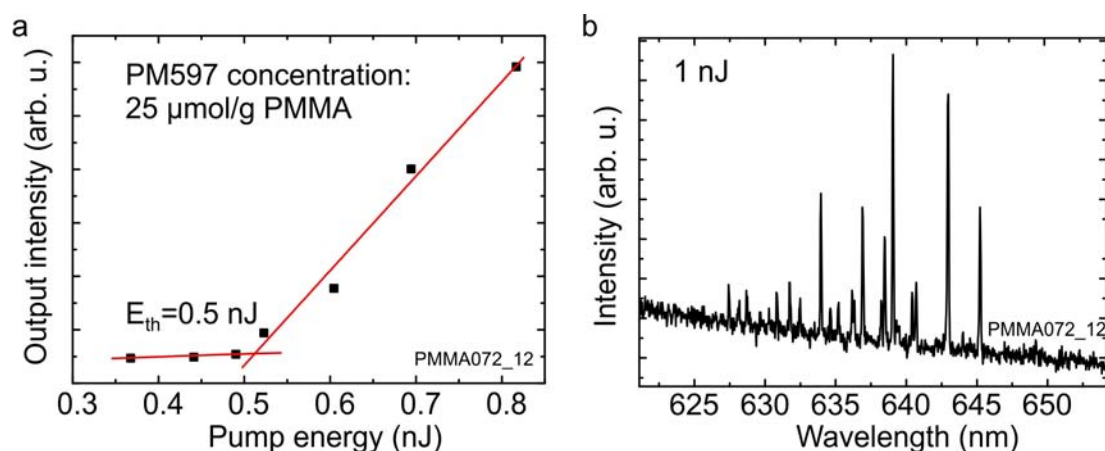


Figure 3.12: (a) Input-output curve of a PM597-doped microgoblet with a lasing threshold energy of 0.5 nJ. (b) Lasing spectrum recorded at a pump energy of 1 nJ. Multimode lasing occurs at wavelengths between 620 and 650 nm.

tion and emission spectrum of a PMMA film with a pyrromethene concentration of 13 $\mu\text{mol/g}$ solid PMMA is shown in Fig. 3.11 (b). The maximum absorption occurs at a wavelength of 525 nm and the maximum of the emission spectrum is at 568 nm. These values are in good agreement with measurements reported in literature [99]. The resulting Stokes shift of 43 nm is twice as large as for rh6G in PMMA (section 3.2.1). The larger Stokes shift significantly increases the lasing performance in highly concentrated PM solutions due to less reabsorption in the emission band [99]. This allows for fabrication of microgoblets with higher dye concentrations compared to rh6G without adverse effects on the lasing threshold.

The optical characterization of the PM597-doped microgoblets was performed with the same free-space excitation setup as for the rh6G samples (Fig. 3.7). The increase of lasing performance of PM597-doped microgoblets can clearly be seen in Fig. 3.12. In this case, the sample contained a dye concentration of 25 $\mu\text{mol/g}$ solid PMMA. The input-output curve with a lasing threshold energy of 0.5 nJ is shown in Fig. 3.12 (a). This is an improvement by a factor of six compared to the lowest observed threshold (3 nJ) of rh6G-doped microgoblets and can be attributed to the above discussed advantageous properties of pyrromethene dyes.

Lasing in PM597-doped microgoblets occurs at wavelengths between 620 and 650 nm. A lasing spectrum recorded at a pump energy of 1 nJ is shown in Fig. 3.12 (b). The gain spectrum is clearly red-shifted compared to the emission of rhodamine 6G-doped microgoblets (Fig. 3.9). A spectral distance of 2 nm between lasing modes can be partly identified in the spectrum, e.g., the distance between the two peaks on the right hand side of Fig. 3.12 (b), which corresponds to the free spectral range of the

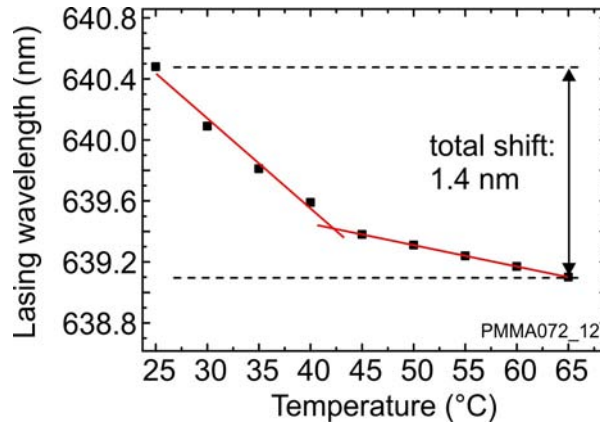


Figure 3.13: Shift of the lasing wavelength of a microgoblet laser for a temperature increase from 25 to 65 °C. A temperature difference of 40 °C results in a blue shift of the lasing wavelength of about 1.4 nm, due to the negative thermo-optic coefficient of PMMA.

cavity. At low pump energy, lasing most likely takes place in the fundamental cavity modes of both polarizations due to the highest modal gain compared to higher-order modes of the cavity.

Temperature dependency and operational lifetime of PM597-doped microgoblets

For possible future application of microgoblet lasers, temperature dependency and the operational lifetime are important quantities to characterize. These two application-oriented aspects of the operation of microgoblet lasers are discussed in the following paragraphs.

The effect of a temperature change on the wavelength of a laser depends on the temperature dependency of the cavity resonances. In the simplest case, resonances in polymeric microcavities are influenced by two effects: the temperature dependency of the refractive index and the thermal expansion of the cavity material. PMMA has a large (negative) thermo-optic coefficient $dn/dT = -105 \times 10^{-6}/\text{K}$ [101], which is more than two orders of magnitude larger than in silica ($dn/dT = 0.55 \times 10^{-6}/\text{K}$ [102]). An increasing temperature of the cavity should therefore result in a decrease of the refractive index and a blue shift of the resonance wavelength. Besides causing a decrease of the refractive index, increasing temperature also leads to expansion of the cavity material, which is described by the (positive) linear thermal expansion coefficient α , and leads to a red shift of the resonance. For PMMA, the thermal expansion coefficient has a value of $\alpha = 68 \times 10^{-6}/\text{K}$ [101]. In a first order approx-

imation the influence of both temperature effects on the resonance wavelength can be calculated by the following equation [102, 103]:

$$\lambda(\Delta T) = \lambda_0 \left(1 + \left(\alpha + \frac{dn}{dT}/n \right) \Delta T \right) \quad (3.10)$$

The reference wavelength without temperature change ΔT is denoted as λ_0 and the refractive index of the cavity material is n . If α and dn/dT are assumed to be temperature independent, equation 3.10 predicts a linear temperature dependency of the resonance wavelength.

To experimentally measure the temperature dependency of the lasing wavelength of PM597-doped microgoblets, the sample holder was equipped with a resistance thermometer (PT100) in combination with a Peltier element. The Peltier element was used to heat the sample to a temperature above room temperature. The electric current applied to the Peltier element was regulated by a proportional-derivative-integral (PID) controller to precisely control the temperature to an accuracy of 0.1 °C. The temperature dependency of a laser wavelength of an optically pumped microgoblet is depicted in Fig. 3.13. For temperatures between 25 and 40 °C the wavelength decreases linearly with a slope of -59 pm/°C, caused by the negative thermo-optic coefficient of PMMA. Above 40 °C the slope of $\lambda(T)$ changes to a value of -14 pm/°C, which is about a factor of four lower compared to temperatures below 40 °C. This strong change of the temperature dependency of the cavity resonances above 40 °C was also observed for passive microgoblets and cannot be explained solely by including the thermal expansion and thermo-optic effect in equation 3.10 [104]. A possible explanation for the deviation from equation 3.10 could be mechanical stress, which is deposited in the PMMA layer during the fabrication process (see section 2.2.1) and gives rise to birefringence within the cavity. This stress relaxes for temperatures above 40 °C, which changes the optical anisotropy within the PMMA layer [104], leading to strongly reduced temperature dependency of the lasing wavelength. This smaller temperature dependency is an advantage for applications requiring tracking of the lasing wavelength, as thermal fluctuations add noise to the spectral position of the laser line.

The second important aspect for the usability of microgoblet dye lasers in applications, such as biosensing, is the operational lifetime. Photo-oxidation of dyes embedded in solid matrices is typically the biggest issue for this type of solid-state laser (see section 3.1.4) [82, 100]. To investigate the operational lifetime of the PM597-doped microgoblets developed in this work, the emission spectrum of a PM597-doped microgoblet was measured during a time span of several hours using the free-space excitation setup (Fig. 3.7). Emission spectra were recorded continuously with an

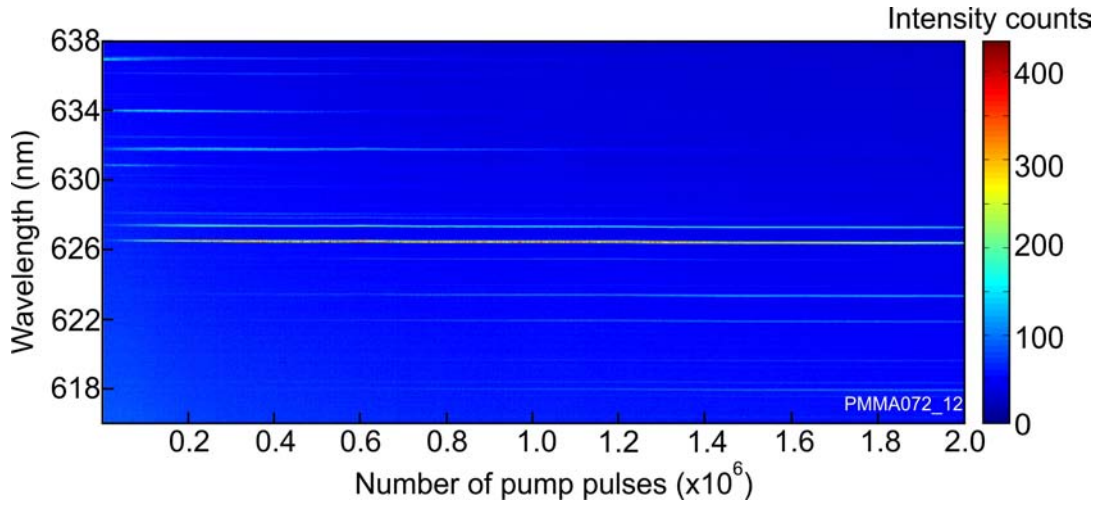


Figure 3.14: Emission spectrum of a PM597-doped microgoblet laser as function of the number of pump pulses. Lasing after more than 2×10^6 pump pulses could be observed and demonstrates the high operational lifetime of these lasers.

integration time of one second by pumping the microgoblet laser with a repetition rate of 100 Hz at a pump energy of several nanojoule. The lasing spectrum as function of the number of pump pulses is depicted in Fig. 3.14. After around 0.5×10^6 pump pulses, a blue shift of the envelope of the emission spectrum becomes apparent. This could be contributed to a bleaching of dyes, which are embedded loosely within the PMMA matrix, resulting in a shift of the gain spectrum to shorter wavelengths due to a decreasing number density of dye molecules contributing to lasing (see equation 3.5 and Fig. 3.10 (c)). After about 1×10^6 pump pulses, the envelope of the lasing spectrum remains relatively constant and lasing was observed after 2×10^6 pump pulses without decreasing emission intensity. This corresponds to a lowest boundary for the operation time of over five hours. This long operational lifetime is an ideal prerequisite for the utilization of microgoblet lasers in applications requiring long-term measurements over a time range of several hours. One application of microgoblet lasers investigated in this work is label-free detection of molecules, which is discussed in the next section.

3.3 Microgoblet lasers for label-free biosensing

In this section the utilization of microgoblet lasers for label-free biosensing is presented. At first, a general overview of optical biosensors is given, followed by a more specific discussion on sensors based on whispering-gallery modes and their applica-

tion for label-free detection of molecules. As the detection of molecules typically occurs in liquid solutions, a discussion of the lasing properties of microgoblets in aqueous environments is presented before the label-free detection of proteins with microgoblets is demonstrated.

3.3.1 Optical biosensors

Over the last years, optical biosensors have emerged as a versatile tool for the detection of chemical and biological analytes with applications in medicine, healthcare, environmental monitoring, homeland security etc. [27, 47, 105, 106]. They are robust with respect to electromagnetic interferences, are capable of performing remote sensing, and enable multiplexed detection with a single device [27]. Biosensors are classified by their different detection mechanisms as marker-based and label-free sensors. In fluorescence-based detection methods, either target or biorecognition molecules are labeled with a fluorescent marker. Fluorescent proteins are commonly used as markers. The presence of the molecules is therefore signalized by the fluorescence intensity of the label. Despite a sensitivity which can reach the single-molecule level [107], fluorescence-based methods have severe disadvantages. Firstly, the labeling process is laborious and the label can change the functionality of the molecule. Secondly, quantitative analysis is difficult due to an uncontrolled amount of fluorophores on each molecule [27]. On the other hand, label-free detection does not require modification of the target molecules, which ensures their functionality and reduces the effort for sample preparation.

Among label-free, optical detection methods, such as Raman spectroscopic detection, optical absorption detection and refractive index (RI) detection, the latter sensing method has attracted the most interest over the last years. RI sensors detect the RI of a bulk solution (refractometer) as well as the RI change induced by molecule binding. By removing the requirement for labels, RI-based sensing allows for real-time and direct detection of molecular interactions at a dielectric interface [47, 106]. RI sensors have been implemented based on several different photonic transduction methods and technologies, such as surface plasmons [108, 109], interferometers [110, 111], optical fibers [112], photonic crystals [113–115], and WGM microcavities [17, 116–119].

Among these different methods to detect refractive index changes, WGM resonators with high Q-factors have emerged as a highly promising and perhaps most sensitive type of label-free optical sensor. The sensitivity arises from the high Q-factor, which enables multiple interactions between the optical mode and the target molecules binding to the resonator surface [18]. In addition to high sensitivity, on-chip integration and wafer-scale fabrication methods of WGM resonators could lead to

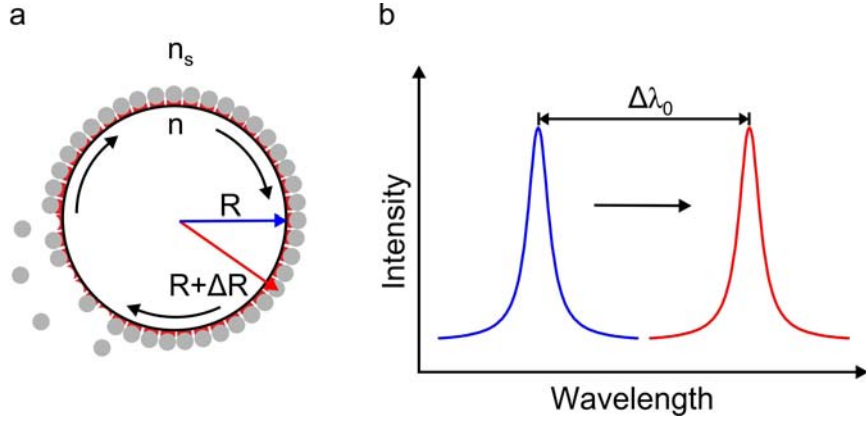


Figure 3.15: Scheme for label-free detection of molecules. (a) The binding of molecules to the surface increases the effective radius of the microcavity. (b) The increased cavity radius leads to a shift of the resonance $\Delta\lambda$ towards larger wavelengths.

the development of sensing systems that are small, portable and low cost [105]. These promising prospects have led to a quickly emerging research field based on whispering-gallery resonators, and first approaches to develop commercial products are evolving.

The basic sensing principle based on the interaction of the WGM with the analyte as well as important figures of merit of biosensors are described in the following.

3.3.2 High-Q WGMs for label-free molecule detection

WGM microcavities have been applied for the label-free detection of various different types of molecules, such as proteins [17, 116] and DNA [120], as well as microorganisms, like bacteria [117] or viruses [121]. The electric field of the mode polarizes each molecule that binds to the surface of the cavity. A fraction of the energy of the mode is lost by polarizing the molecule, leading to a shift in the resonant frequency. The simplest analytical expression explaining the interaction of molecules with the optical mode can be inferred from the resonance condition stated in equation 2.1. Here, the resonance wavelength λ_0 of a WGM either shifts by a change of the cavity radius R by a binding of molecules to the cavity surface or by a change of the refractive index n [121]:

$$\frac{\Delta\lambda_0}{\lambda_0} = \frac{\Delta R}{R} + \frac{\Delta n}{n} \quad (3.11)$$

The shift of the wavelength is denoted as $\Delta\lambda_0$ and the changes of the cavity radius and refractive index are ΔR and Δn , respectively. The refractive index difference Δn is given by the difference between the refractive index of the cavity and of the surrounding medium n_s : $\Delta n = n - n_s$. A simple schematic illustrating the shift of a resonance due to an increased cavity radius after binding of molecules is depicted in Fig. 3.15. Equation 3.11 states that wavelength shifts occur on length scales shorter than the evanescent-field decay length (binding of molecules to the resonator surface) or on length scales larger than the evanescent-field decay length (refractive index changes of the surrounding). The latter is often referred to as bulk refractive index sensitivity (BRIS). Both of these mechanisms, which lead to a spectral shift of the WGM, depend on the overlap of the optical mode with the surrounding medium, denoted as η . To account for this, the resonance condition stated in equation 2.1 has to be modified as follows [118]:

$$2\pi R (n_s \eta + n(1 - \eta)) \approx N_\phi \lambda_0 \quad (3.12)$$

The refractive index of the surrounding medium is denoted as n_s . The bulk refractive index sensitivity S is a measure describing how strong the resonance wavelength changes upon change of the surrounding medium and can be derived from equation 3.12 by taking the derivative of λ_0 with respect to n_s [118, 122]:

$$S = \left(\frac{d\lambda_0}{dn_s} \right) = \frac{2\pi R}{N_\phi} \eta \approx \frac{\lambda_0}{n_{eff}} \eta \quad (3.13)$$

where in the last step the relation $N_\phi \approx 2\pi R n_{eff} / \lambda_0$ was used instead of equation 2.1 to account for the effective refractive index of the mode n_{eff} . The BRIS according to equation 3.13 is proportional to the overlap of the optical mode with the analyte and is often quantified in the units of nanometer per refractive index unit (nm/RIU). It was shown that the wavelength shift for molecule attachment is linearly proportional to the BRIS of the WGM resonator and can be calculated by the following equation [118]:

$$\frac{\Delta\lambda_0}{\lambda_0} = \sigma_s \alpha_0 \frac{2\pi \sqrt{n^2 - n_s^2}}{\epsilon_0 \lambda_0^2} \frac{n}{n_s^2} S \quad (3.14)$$

where α_0 is the polarizability of the molecule and σ_s is the surface density of the molecules on the cavity. Due to this important relation in equation 3.14, the BRIS is an often used quantity for characterization of optical biosensors. Sensors with a high overlap of the mode with the surrounding medium have a high BRIS. Surface plasmon resonances (SPR) typically have a BRIS of several 1000 nm/RIU [122]. In

contrast, WGM resonators, which utilize the evanescent field to probe the surrounding medium, have a far lower BRIS in the order of 10 to 100 nm/RIU due to a low overlap of the mode with the analyte of typically several percent [122].

However, the BRIS alone is not sufficient for a quantitative characterization of the performance of a sensor. For this, a further measure has to be introduced which includes the resolution of the sensing system and various types of noise sources: the detection limit (DL) of the sensor. The detection limit describes the smallest RI change or the minimum amount of molecules that the sensor can accurately quantify. In general, the DL of a device is given by the ratio between sensor resolution R and the BRIS S [122]:

$$DL = \frac{R}{S} \quad (3.15)$$

A sensor with low detection limit needs a high BRIS in combination with a small resolution R . The resolution describes the smallest resolvable wavelength shift and is typically determined by the total noise variance 3σ . Three main factors contribute to the overall resolution: amplitude noise, temperature noise, and the spectral resolution. Temperature noise can be minimized by stabilizing the resonator temperature externally (e.g., by a thermo-electric temperature control) or by designing the resonator resonances to be temperature independent [17, 102]. The spectral resolution of the measurement system is limited by either the laser or the optical detection mechanism, depending on the measurement system. Using tunable, external cavity diode lasers with very small linewidths in the femtometer range, the influence of the laser itself can be neglected. On the other hand, if the cavity linewidth is measured by a spectrometer, the spectrometer resolution can limit the overall resolution of the sensor. Amplitude noise describes all the fluctuations which are added on top of the signal of the spectral mode profile and have their origin in jitter from the laser source, photodetectors, etc. This amplitude noise is inversely proportional to the Q-factor of the resonance [122]. This demonstrates the big advantage of sensors based on high-Q resonators: a high sensor resolution. If noise contributions from temperature can be neglected and the spectral resolution is high, the detection limit is inversely proportional to the Q-factor and to the overlap of the optical mode with the analyte:

$$DL \propto \frac{1}{\eta Q} \quad (3.16)$$

The product $\eta \times Q$ is the figure of merit, which has to be maximized for the development of high performance sensors. The ultimate limit of detection is the detection of

single molecules. This was experimentally demonstrated with WGM sensors using passive silica microtoroids with Q-factors above 10^8 [17]. Although the experimental data clearly suggests the observation of events corresponding to the binding of single molecules, the measured shifts are larger than theoretically expected from equation 3.14, and a discussion about the responsible mechanisms leading to these single molecule events is still ongoing in literature [123].

Active microcavities for label-free sensing

Despite these promising prospects of an extremely high sensitivity achievable with high-Q on-chip microcavities, the use of tapered optical fibers for the excitation of WGMs in microcavities with surface-tension induced cavity geometry is a major issue for the development of commercial products based on this technology. The tapered sections are extremely fragile and often degrade within several hours, such that light transmitted through the tapered section is almost completely attenuated. This degradation proceeds even faster in aqueous environments, which are unavoidable in biosensing applications. Furthermore, the nanometer positioning precision of the tapered section required to couple light into the resonator further complicates the development of a device which can be operated outside precisely controlled laboratory conditions as required, e.g., for a commercial product.

One solution to overcome the aforementioned technological difficulties of operating passive high-Q microresonators in aqueous environments is the use of active microcavities instead of passive ones, as already indicated in section 3.2.2. In addition to the possibility of using robust free-space excitation and detection of lasing modes, active microcavities in principle allow for an even higher detection sensitivity as compared to their passive counterparts. This originates from the narrower linewidths achievable with active cavities due to the compensation of propagation losses in the presence of gain. This idea was proposed by Guo et al. in 2006 [28] and demonstrated experimentally by He et al. four years later [29]. The measurements of He et al. clearly show a decreased linewidth of the resonances in the presence of gain [29]. The ultimate limit of the linewidth of a laser $\delta\omega_{osz}$ is given by the Schawlow-Townes limit [2]:

$$\delta\omega_{osz} = \frac{2\pi\hbar\omega_0(\delta\omega_0)^2}{P_{osz}} = \frac{2\pi\hbar\omega_0^3}{P_{osz}Q^2} \quad (3.17)$$

where the pump power of the lasing mode is given as P_{osz} and the linewidth of the cavity is $\delta\omega_0$. In toroidal microcavity lasers, Schawlow-Townes limited linewidths as narrow as 4 Hz have been observed [124], which is several orders of magnitude

smaller than the 300 kHz linewidth observed in a passive cavity with a Q-factor of 10^8 . Such measurements of the laser linewidth are generally performed using elaborate homodyne and heterodyne detection techniques [11, 125, 126].

To avoid complex measurements for tracking of the laser linewidth for detection of molecules, an alternative heterodyne method to detect the binding of molecules or nanoparticles with WGM microlasers was introduced by He et al. [29], which is based on the mode-splitting mechanism. Mode splitting has been explained as the result of coupling between degenerate clockwise (cw) and counterclockwise (ccw) propagating modes in WGM microcavities via back scattering [127]. This degeneracy lifting of WGMs with the azimuthal mode numbers $\pm N_\phi$ leads to the observation of duplets in the spectrum (compare Fig. 2.11 (b)) and was also observed in passive microgoblets [104]. The back-scattering mechanism occurs by Rayleigh scattering of light at single sub-wavelength particles or defects within the mode volume. Due to the small mode volumes and high Q-factors of WGM microcavities, a strong Purcell effect leads to a preferred scattering of the light into the optical mode propagating in the other direction. This results in a coherent energy exchange between cw and ccw mode [127–129]. In a microlaser, mode splitting can result in two closely spaced lasing modes [4, 29]. The interference of both split modes on a photodetector will result in a heterodyne beat note [29]

$$i(t) \propto P_1 + P_2 + 2\sqrt{P_1 + P_2} \cos(\Delta\omega t + \Delta\phi) \quad (3.18)$$

where P_1 and P_2 are the powers of the two split modes, and $\Delta\omega = |\omega_1 - \omega_2|$ and $\Delta\phi$ are the frequency and phase differences between the split modes, respectively. A schematic illustration of mode splitting caused by a scattering center and the resulting beat note is depicted in Fig. 3.16.

Heterodyne beat-note measurements are a simple and robust method for the detection of nanometer-sized objects [4, 29]. Without nanoparticles on the cavity the laser modes are not split and no beating is observable. The lasing modes split into two modes when a nanoparticle binds to the resonator, resulting in a beat note. The lasing spectrum and the frequency of the beat note change upon the binding of further nanoparticles. Environmental noise, such as temperature fluctuations, influences only the spectral position of the lasing modes, but not the beat note signal, because both modes are shifted equally. This makes the heterodyne beat-note detection scheme in combination with free-space excitation and detection of lasing modes robust with respect to environmental influences [4, 29], which is a highly promising prospect for future development of compact, portable optical sensing systems based on active WGM microcavities.

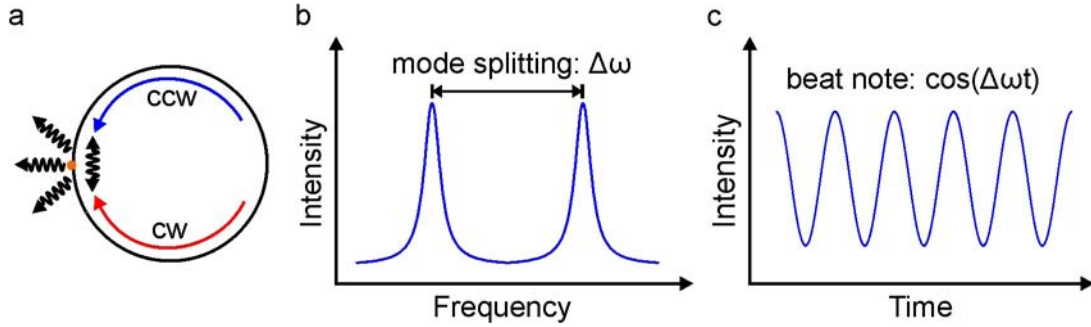


Figure 3.16: (a) A scattering center causes coherent coupling between cw and ccw propagating modes, which results in degeneracy lifting (mode splitting) of these modes. (b) The active microcavity emits in two modes separated by the frequency difference $\Delta\omega$. (c) Interference of both modes in a photodetector leads to a beat note signal proportional to $\cos(\Delta\omega t)$. (Adapted from [4, 129]).

3.3.3 Microgoblet lasers in aqueous environments

To demonstrate the applicability of dye-doped microgoblet lasers for biosensing experiments, the lasers were first operated and characterized in aqueous environments. To immerse the chip with resonators in water, the μ PL setup described in section 3.2.2 was complemented by a fluidic chamber with inlet and outlet ports for liquids on top of the sample holder (Fig. 3.17 (a)). This enabled filling of liquids and purging of the chamber (total volume 250 μ l) via syringes. A typical lasing spectrum of a PM597-doped⁸ microgoblet operated in water is depicted in Fig. 3.17 (b). The spectrum consists of evenly spaced lasing modes separated by a free spectral range of $\delta\lambda_{FSR} = 2$ nm. In comparison to the lasing spectrum in air (Fig. 3.12 (b)), the number of lasing modes is strongly reduced. This could be explained by the reduced refractive index contrast between PMMA and water ($\Delta n = 0.16$) compared to PMMA and air ($\Delta n = 0.49$), which leads to increased radiation losses of the WGMs as discussed in section 2.1.2. Especially the higher-order modes have an increased overlap with the surrounding water and suffer the highest reduction in Q-factor. Therefore, the lasing depicted in Fig. 3.17 (b) most likely occurred in the fundamental modes of the cavity⁹.

The lasing threshold for microgoblet operation in water was found to be $E_{th} = 1.6$ nJ. The corresponding input-output curve is shown in Fig. 3.18 (a). This threshold value

⁸The PM597 concentration was 25 μ mol/g solid PMMA.

⁹For pump energies far above the threshold, lasing also occurred in higher order cavity modes, which is manifested by a spectral spacing of the lasing well below the FSR of the cavity.

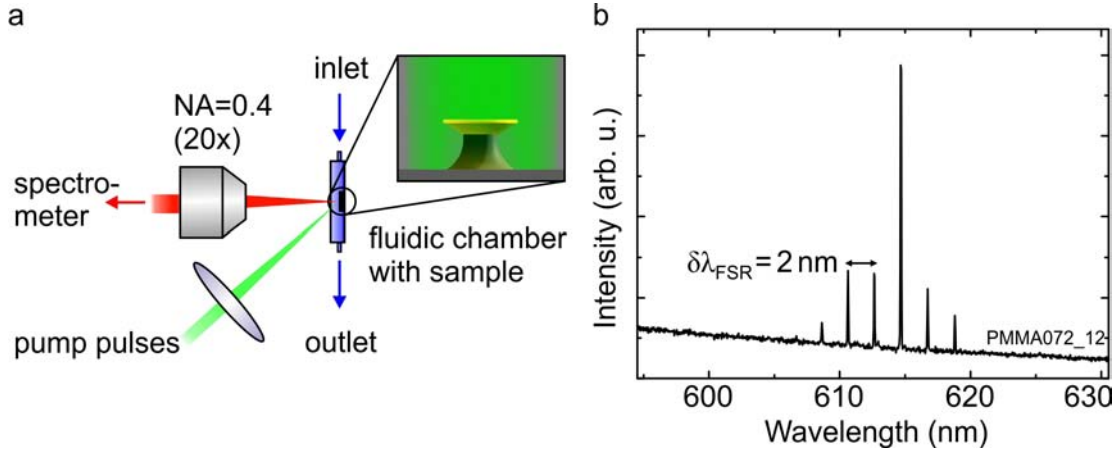


Figure 3.17: (a) The microphotoluminescence setup was complemented with a fluidic chamber for characterization of microgoblet lasers in aqueous environment. (b) Typical lasing spectrum of a PM597-doped microgoblet immersed in water. Evenly spaced lasing modes separated by the free spectral range of 2 nm suggest that lasing occurs in the fundamental cavity modes.

is about a factor three larger than that for operation of microgoblets in air (compare Fig. 3.12 (a)).

The reduced refractive index contrast in water leads to increased radiation losses, which were quantified by finite element simulations introduced in section 2.2.5. Calculations show that the radiation-limited quality factor of the fundamental modes at wavelengths between 600 and 630 nm in microgoblets with a radius of 20 μm takes on values between $Q_{\text{rad}} = 1 \times 10^7$ and 6×10^6 . In principle, additional losses could result from the absorption of water at the lasing wavelengths. The values for the absorption-limited quality factor in water at wavelengths between 600 and 630 nm are between $Q_{\text{abs}} = 7 \times 10^9$ and 4×10^7 (data of the wavelength-dependent absorption coefficient of water was taken from literature [130]). Losses originating from the imaginary part of the refractive index of water at wavelengths in the 600 nm wavelength region are therefore negligible compared to radiation losses. For future experiments, these radiation losses could be decreased by increasing the radius of the microgoblets.

The higher lasing threshold in an aqueous environment also becomes apparent by comparison of the spectral position of the lasing modes in air (Fig. 3.12 (b)) with the spectrum in water (Fig. 3.17 (b)). The envelope of the gain spectrum recorded in water is clearly blue-shifted by 20 nm compared to the spectrum recorded in air. This results from the lasing dynamics of dye lasers stated in equation 3.5, where a reduced Q-factor leads to a shift of the gain envelope towards shorter wavelengths (compare

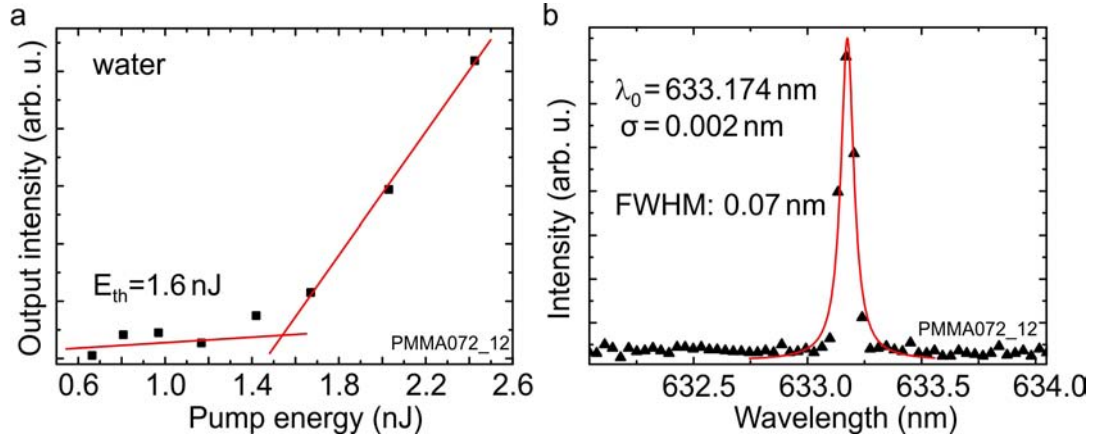


Figure 3.18: (a) The lasing threshold of PM597-doped microgoblets operated in water is $E_{th} = 1.6$ nJ, which is a factor three larger compared to the threshold during operation in air. (b) The linewidth of the lasing modes of a PM597-doped microgoblet in water is around 0.07 nm (FWHM) and limited by the spectrometer resolution. The standard deviation of the resonance position λ_0 inferred from the Lorentzian fit (red curve) is $\sigma = 0.002$ nm.

Fig. 3.10 (c)). The linewidth of microgoblet lasers operated in water is limited by the spectrometer resolution (grating with 1200 lines/mm) to values around 0.07 nm (FWHM), as exemplarily shown in Fig. 3.18 (b). The standard deviation of the spectral position of the resonance determined from the Lorentzian fit is $\sigma = 2$ pm. This statistical error results from the low number of data points available for the fit.

Sensing characteristics of microgoblet lasers

An important figure of merit for characterization of the sensing properties of microgoblet lasers is the bulk refractive index sensitivity, which is a measure for the overlap of the evanescent field with the surrounding medium (equation 3.13). To measure the BRIS of active microgoblets, the shift in the lasing wavelength for the changing refractive index of the surrounding medium was monitored. For this, solutions with different glucose concentrations, and therefore different refractive indices compared to pure water, were prepared. The refractive index of each glucose solution was determined by a refractometer (PAL-RI, ATAGO) at a wavelength of 589 nm, which is close to the lasing wavelengths of the microgoblets. To clearly identify the wavelength shift resulting from a change of the refractive index, time-resolved measurements of the lasing spectra were performed. For this, lasing spectra were recorded every two seconds, and the spectral position of a single lasing peak was tracked over time. Before measurement, samples were immersed in water for about 30 min in order to avoid wavelength shifts originating from swelling of PMMA as a

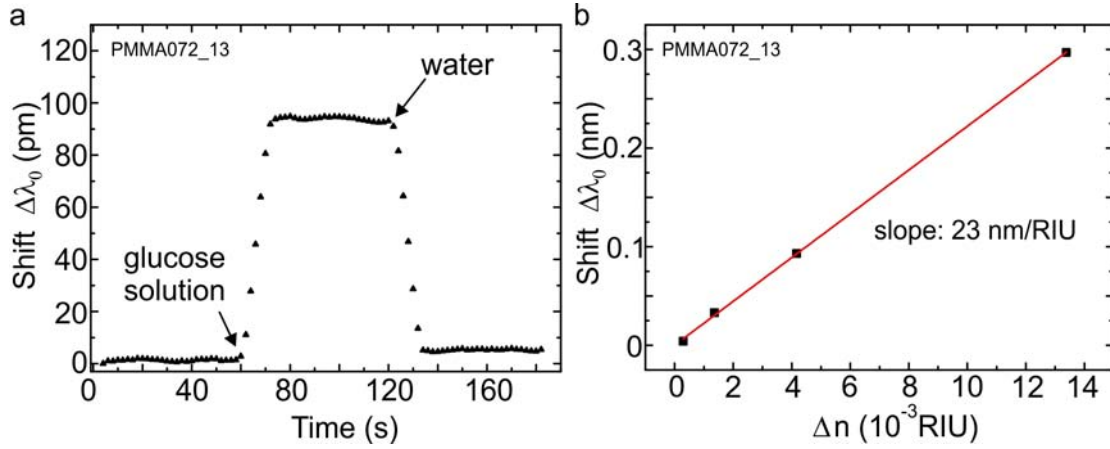


Figure 3.19: (a) Shift of the lasing wavelength over time. After 60 s, a glucose solution was injected into the fluidic chamber, which leads to a shift of the lasing wavelength of about 100 pm due to a refractive index change compared to pure water. After the fluidic chamber was purged with water, the lasing wavelength shifted back to the initial value. (b) Shift of the lasing wavelength for different refractive index changes Δn . The BRIS of microgoblet lasers is given by the slope of the linear fit, which is 23 nm/RIU.

result of water sorption. A time-resolved measurement is depicted in Fig. 3.19 (a). After 60 s, a glucose solution was injected into the fluidic chamber, which leads to a shift of the lasing wavelength of about 100 pm due to a refractive index change compared to pure water. After a measurement time of 120 s, the fluidic chamber was purged with water and the lasing wavelengths shifted back to the initial value. These experiments were performed for three different concentrations of glucose. The resulting wavelength shift for the different refractive index changes Δn is shown in Fig. 3.19 (b). The response of the microgoblet lasing wavelengths to changes of the surrounding refractive index is linear, as expected from equation 3.11. The BRIS is given by the slope of the linear regression in Fig. 3.19 (b), which has a value of $S = 23$ nm/RIU at a lasing wavelength around 630 nm.

From finite element simulations of microgoblets, the BRIS was directly determined to be 30 nm/RIU by solving equation 2.18 for two different indices of the surrounding medium. As stated in equation 3.13, the BRIS can also be determined from the overlap η of the mode with the environment, which was calculated numerically using the following expression:

$$\eta = \frac{\int_{env} \epsilon(\vec{r}) |\vec{E}(\vec{r})|^2 dV}{\int_{total} \epsilon(\vec{r}) |\vec{E}(\vec{r})|^2 dV} \quad (3.19)$$

where the integration of the electric density in the numerator is performed within the region surrounding the cavity and the denominator denotes the integration of the electric energy density within the entire computational domain. For a wavelength of 630 nm, the overlap factor (evanescent field) in microgoblets was calculated to be about $\eta = 6\%$, which results in a value of $S = 27 \text{ nm/RIU}$. This is in good agreement with the exact value of the BRIS (30 nm/RIU) determined from simulations. The deviation of both values is about 10% and proves that equation 3.13 is a good analytical expression for calculation of the BRIS. Comparison of the experimentally measured value of the BRIS ($S = 23 \text{ nm/RIU}$) with the simulated value reveals a discrepancy of around 25%. This difference most likely resulted from slight geometrical deviations of the simulated microgoblet cross-section from the fabricated structure. The BRIS of microgoblets is in the same order of magnitude as that of other sensors based on WGMs in solid-state microcavities reported in literature [118], where the evanescent wave probes the surrounding medium. The strong wavelength dependency of the BRIS makes a direct quantitative comparison with values reported in literature difficult, as most of the passive microcavities are characterized at wavelengths above 900 nm.

The detection limit of the dye-doped microgoblet lasers investigated in this work was limited by the resolution of the linewidth, which was measured using a spectrometer with a grating of 1200 lines/mm. As shown in Fig. 3.18 (b), the standard deviation for the spectral resonance position is $\sigma = 2 \text{ pm}$. Only shifts larger than $3\sigma = 6 \text{ pm}$ can be determined with this measurement method. The detection limit for changes in the bulk refractive index is therefore given by $DL = 3\sigma/S = 2.4 \times 10^{-4} \text{ RIU}$.

3.3.4 Label-free detection of proteins

In addition to the detection of changes of the refractive index, the evanescent field of microgoblet lasers can also be utilized for the label-free detection of molecules, such as proteins. Binding of a monolayer of molecules to the cavity surface can be considered as an effective increase of the radius of the microcavity, which results in a shift of the resonance wavelength (see equation 3.11 and equation 3.14). In first proof-of-principle experiments for characterization of the label-free molecule detection, the protein streptavidin (molecular weight about 60 000 g/mol) was detected via unspecific binding (physisorption) to the untreated PMMA surface of the microgoblets [131]. For first measurements streptavidin (stv) was dissolved in water to a concentration of 500 nM. The microgoblet laser was operated in water for about one minute to generate a baseline, before the stv solution was injected into the fluidic chamber. The time-resolved binding curve is depicted in Fig. 3.20 (a). After four minutes the shift saturates, which indicates that a maximum number of stv mole-

cules were adsorbed on the cavity surface leading to a total shift of 70 pm. After a measurement time of ten minutes, the fluidic chamber was purged with pure water to remove loosely bound molecules from the cavity surface and the remaining stv molecules in the solution. This rinsing process resulted in a decrease of the wavelength shift of about 10 pm. According to equation 3.14, the wavelength shift upon binding of a monolayer of molecules can be calculated, if the bulk refractive index sensitivity of the cavity, the surface density σ_s and the polarizability α_0 of the detected molecules are known. Using the data for the protein bovine serum albumin (BSA) – which has a molecular weight similar to that of streptavidin – with $\sigma_s = 2.9 \times 10^{12} \text{ cm}^{-2}$, $\alpha_0 = 4\pi\epsilon_0 \times 3.85 \times 10^{-21} \text{ cm}^3$ [118, 132] and $S = 23 \text{ nm/RIU}$ (see Fig. 3.19 (b)), a wavelength shift of $\Delta\lambda_0 = 180 \text{ pm}$ was calculated. Therefore, the total wavelength shift of 60 pm measured after purging with water corresponds to a surface coverage of around 33 %.

For streptavidin concentrations of 50 and 5 nM, the total wavelength shift decreases to values of 50 and 20 pm (Fig. 3.20 (b) and (c)), respectively. A summary of the wavelength shifts for the three concentrations is depicted in Fig. 3.20 (d), where the wavelength shift after a measurement time of four minutes as function of the concentration is plotted in a double-logarithmic scale. An additional measurement with a stv concentration of 0.5 nM was performed, which results in a wavelength shift of 2 pm after a time of four minutes. This shift is below the 3σ detection limit of 6 pm and is marked with a red dot in Fig. 3.20 (d). To roughly estimate the smallest measurable protein concentration, a linear behavior was assumed for values below 100 nM in Fig. 3.20 (d), where a guide for the eye is given by the dashed line. Above 100 nM the slope changes, which could result from saturation of the shift [118]. The lowest concentration which can be measured using microgoblet lasers in combination with a spectrometer with a certainty of 99.7 % is 2 nM. This value was inferred from the intersection point of the dashed line with the horizontal line $3\sigma = 6 \text{ pm}$ in Fig. 3.20 (d).

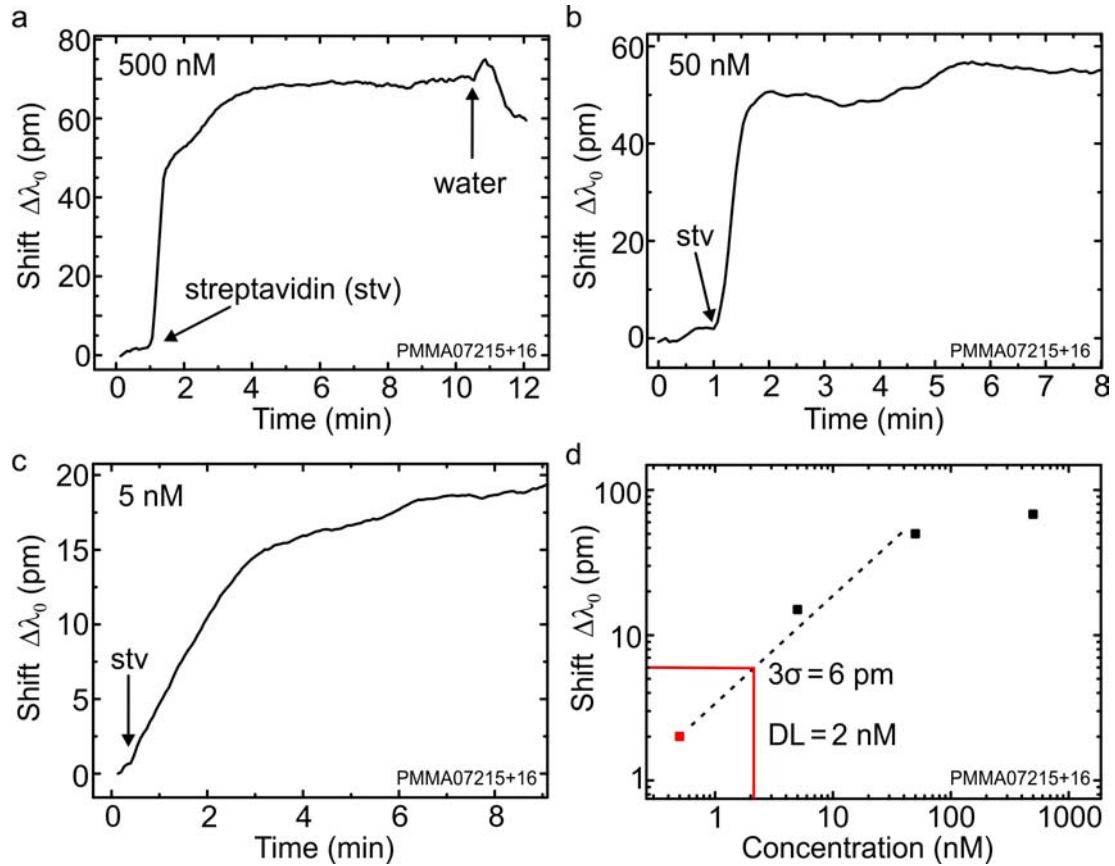


Figure 3.20: Label-free detection of streptavidin with microgoblet lasers. Time-resolved measurements and binding curves with stv concentrations of (a) 500 nM (b) 50 nM and (c) 5 nM show a resonance wavelength shift, which depends on the stv concentration. (d) Summary of the concentration-dependent wavelength shifts observed after a measurement time of four minutes on a double-logarithmic scale. The dashed line is a guide for the eye and indicates a linear decrease of $\Delta\lambda_0$ for concentrations below 100 nM. An additional measurement was performed at a concentration of 0.5 nM (marked by the red dot), which is below the detection limit of 2 nM.

3.4 Summary and conclusions

In this chapter, the fabrication of dye-doped PMMA microgoblets and the optical characterization of their lasing properties was presented. The lasing threshold and the spectral position of the gain curve strongly depended on the dye concentration. In these experiments the dye rhodamine 6G was used as gain medium. The concentration-dependent lasing properties were explained by a standard dye-laser model including a concentration-dependent Q-factor. The lowest lasing threshold of rh6G-doped microgoblets was 3 nJ. Integration of the dye pyrromethene 597 into the PMMA host matrix allowed for realization of microgoblet lasers with lasing thresholds as low as 0.5 nJ. In addition to a high lasing efficiency, PM597-doped microgoblets were found to have a long operational lifetime of more than 2×10^6 pump pulses, corresponding to a operation time of several hours. This operational lifetime of dye-doped microgoblets is sufficient for many applications, such as biosensing, where the detection of molecules typically occurs within a time frame of several seconds or minutes.

To demonstrate the applicability of these devices for label-free molecule detection, active microgoblets were operated in an aqueous environment. The lasing threshold increased to a value of 1.6 nJ due to additional radiation losses originating from a reduced refractive index contrast compared to that of operation in air. An important quantity for characterization of the sensing properties is the bulk refractive index sensitivity, which is a measure for the overlap of the optical mode with the surrounding environment. The BRIS of the investigated microgoblets was obtained from measurements of the shift of the lasing wavelength upon changes of the refractive index of the surrounding. A value of 23 nm/RIU was obtained for the BRIS at a lasing wavelength of 630 nm. Proof-of-principle experiments for the label-free detection of molecules were carried out by detecting the protein streptavidin, which binds unspecifically via physisorption to the cavity surface. The lowest detectable protein concentration was estimated to be 2 nM. In future experiments the detection limit could be improved significantly using self-heterodyne beat note measurements, discussed in section 3.3.2, instead of tracking the laser peak via spectrometer, where the linewidth of the microgoblet lasers is limited by the spectrometer resolution.

Chapter 4

Microgoblet lasers with extrinsic gain layer

Besides the integration of gain medium within the polymeric host matrix demonstrated for organic dyes in the previous chapter, active materials can be deposited on the surface of passive microgoblets after lithographic fabrication. This enlarges the spectrum of applicable gain media, as the materials do not have to be doped into PMMA. The intrinsic doping of the polymer matrix has the additional disadvantage that the gain medium is distributed on the entire substrate, which hinders the integration of different laser wavelengths as well as the simultaneous integration of active and passive devices on the same chip.

In the following chapter two different approaches for the realization of an extrinsic gain layer are presented. Both approaches enable the local integration of gain medium on a chip. In the first approach, dip-pen nanolithography (DPN) was utilized to coat the cavity circumference with a molecular ink. This ink consisting of phospholipids can be tailored to include a gain medium as well as biological recognition elements, in order to provide optical gain and molecular sensitivity at the same time. A second approach, which allows for high modal gain in WGM microcavities and therefore low-threshold lasing, is the deposition of a gain material with high refractive index onto the microgoblets. For this, an organic semiconductor was used. The modification of the optical modes in the presence of a coating with high refractive index was analyzed with finite element simulations and compared to experiments, where the effect of the gain layer thickness on the lasing properties was studied.

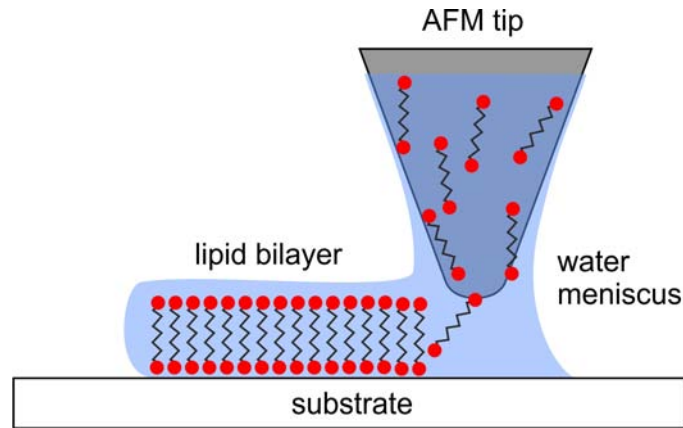


Figure 4.1: Dip-pen nanolithography with phospholipids: self-assembled layers of phospholipids are deposited on a substrate by a water meniscus between substrate and AFM tip.

4.1 Dip-pen nanolithography on microgoblets

In the previous chapter, proof-of-principle experiments for label-free detection of molecules were presented, where the protein streptavidin was unspecifically bound to the cavity surface. In general, a high specificity is a key property of label-free biosensors and can be achieved by applying surface immobilization chemistry where a high analyte capture efficiency and elimination of non-specific binding are major issues [27, 47, 106]. For biosensing experiments, the entire resonator surface is typically functionalized, although only a small fraction of the resonator surface is probed by the optical mode [133]. To reduce the number of binding sites which are not probed by the optical mode, only the circumference of the WGM resonators has to be prepared with a specific type of binding site. The same argument also holds for the deposition of active material on WGM resonators, where only gain medium along the circumference of the cavity contributes to the modal gain. One technique capable of depositing gain medium as well as biological recognition elements along the cavity circumference is dip-pen nanolithography. In the following sections the DPN technique is described, followed by results of the application of DPN for surface functionalization of microgoblets as well as for the deposition of gain medium.

4.1.1 DPN for surface functionalization of microgoblets

Dip-pen nanolithography, a method for directly depositing molecules from an ink-coated atomic force microscope (AFM) tip onto a substrate of interest, is a tool for

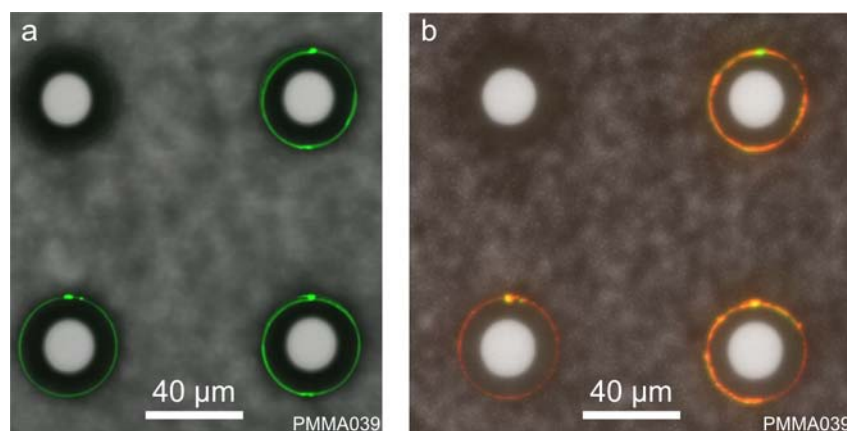


Figure 4.2: Functionalization of the microgloblet circumference with DPN. (a) The biotinylated DOPC ink is labeled with a green dye. The top left resonator serves as reference without functionalization. (b) Binding of red-labeled streptavidin to the green-labeled biotinylated structures results in an orange color along the microgloblet circumference.

creating microscale and nanoscale patterns of materials, such as small molecules and biological macromolecules, where linewidths below 20 nm were achieved for certain materials [134–136]. One class of molecules interesting for surface functionalization are phospholipids, which can be deposited by DPN with a lateral resolution down to 100 nm [137]. Phospholipids are an essential component of biological membranes and tend to self-assemble into two-dimensional bilayer sheets [137]. The structure of the phospholipid molecule generally consists of a hydrophobic tail (long fatty acid hydrocarbon chain) and a hydrophilic head, containing the negatively charged phosphate group. These molecules form bilayers in aqueous environments. After deposition via DPN (see Fig. 4.1), phospholipids form either single or multiple bilayers, depending on the relative humidity of the environment and the scanning speed of the AFM tip [137].

A commercial DPN instrument equipped with a camera and an environmental chamber (DPN 5000, NanoInk) was used to apply a surface functionalization along the circumference of microgloblets. The phospholipid 1,2-dioleoyl-*sn*-glycero-3-phosphocholine (DOPC) was used as carrier ink. DOPC was then admixed with lipids containing a biotinylated end group with a concentration of 4 mol% to provide biotin molecules on the microcavity surface for the detection of streptavidin. First functionalization experiments were performed with passive microgloblets. To visualize the position of biotin molecules on the microgloblets, the carrier ink was additionally doped with green fluorophore-labeled lipids (1 mol%). The ink was applied to the microgloblet surface at room temperature and 50 % relative humidity with a tip

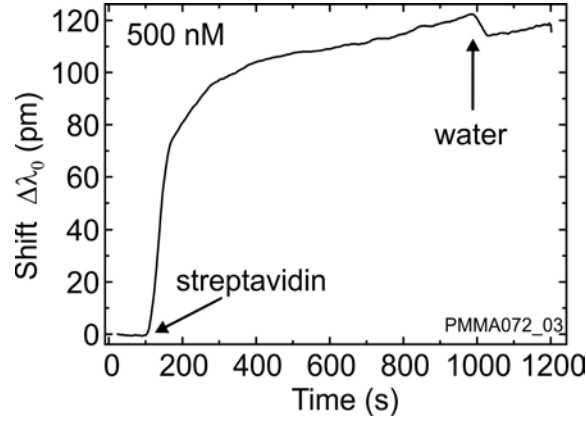


Figure 4.3: Time-resolved shift of the lasing mode of a dye-doped microgoblet with biotinylated circumference. The biotinylated phospholipids were applied using DPN. After a time of 1000 s the sample was purged with water, resulting in a slight decrease of the shift due to partly mobile lipid layers.

velocity of 10 $\mu\text{m/s}$. An image of the fluorescently labeled phospholipids along the circumference of three microgoblets after the writing process with DPN is depicted in Fig. 4.2 (a). One of the microgoblets is without functionalization as reference. The image was recorded by merging a bright field image with an image recorded in the green channel of a fluorescence microscope. After application of the biotinylated ink, the rest of the microgoblet surface was blocked with bovine serum albumin (BSA) to prevent unspecific binding of streptavidin in these regions. Streptavidin was labeled with a red dye (Cy3). The sample was immersed for 15 min in the streptavidin solution and washed afterwards. The coupling of streptavidin to the functionalized microgoblet circumference is visible in Fig. 4.2 (b), where the overlay of the green and red channel of the fluorescence microscope results in an orange-colored microgoblet circumference. Although the ink's adhesion to the goblets is based only on physisorption and not on covalent binding to the resonator surface, the lipid rings remained stable despite several washing and immersion steps, demonstrating sufficient stability of the ink on the three-dimensional goblet topology [138].

In addition to the characterization of the surface functionalization via fluorescence measurements, time-resolved measurements of the shift of the lasing modes upon binding of streptavidin using dye-doped microgoblets with biotinylated circumference were performed. The time-resolved shift of the lasing mode of a PM597-doped microgoblet with phospholipid functionalization is depicted in Fig. 4.3. Streptavidin with a concentration of 500 nM was injected after 100 s, which results in a total shift of about 110 pm. After 1000 s the sample was purged with pure water and the shift decreases slightly due to partly mobile lipid layers [139]. Compared to the detection

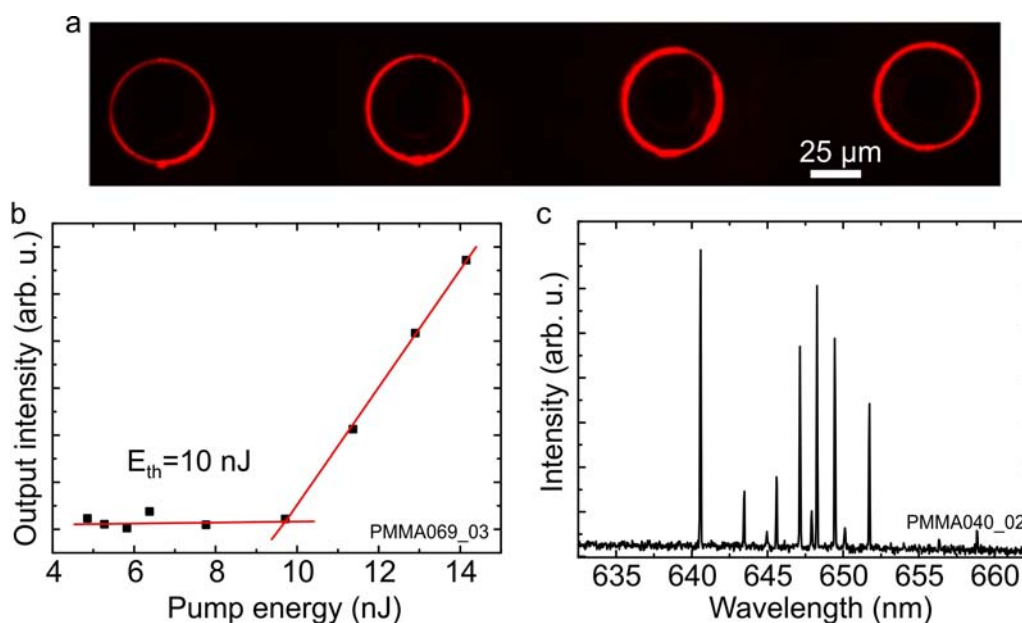


Figure 4.4: (a) Fluorescence from the dye-doped lipid ink, which was deposited along the circumference of passive microgoblets via DPN. (b) The lasing threshold was determined to be around 10 nJ. (c) The lasing occurs in multiple cavity modes with a spectral spacing smaller than the free spectral range of the cavity.

of streptavidin with a concentration of 500 nM without surface functionalization presented in section 3.3.4 (total shift of 70 pm), the shift increased by 60%. This can be contributed to an increased density of binding sites on the resonator surface.

4.1.2 DPN for active microgoblets

To demonstrate the deposition of an active medium on passive microgoblets via DPN, DOPC was admixed with a rhodamine-doped phospholipid (1 mol%). Based on atomic force microscope measurements on test structures written on planar PMMA, the realized ring heights on the goblet rims were inferred to average between 110 and 200 nm [138]. An image of the fluorescence of an array of dye-doped lipid rings on the microgoblets is depicted in Fig. 4.4(a). The gain material is only deposited along the circumference of the resonators, where the WGMs are located. The lasing was characterized with the optical setup presented in section 3.2.2. The input-output curve depicted in Fig. 4.4(b) demonstrates that, although the gain medium covers solely the goblet rims, efficient lasing activity is realized due to the low optical losses of the WGMs in the microgoblet cavity [138]. In air, the observed

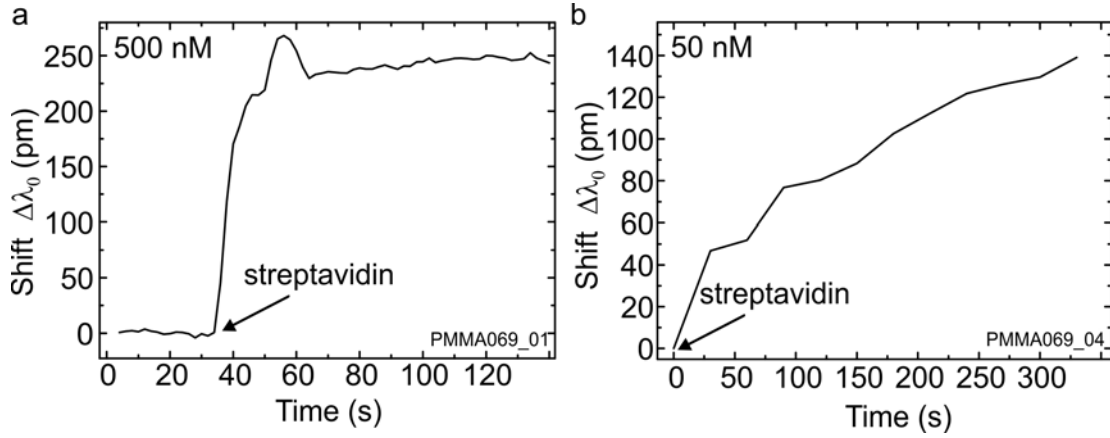


Figure 4.5: Detection of streptavidin in concentrations of (a) 500 nM and (b) 50 nM with microgoblet lasers, where the gain medium and biofunctionality were integrated simultaneously onto passive microgoblets via DPN.

lasing threshold was $E_{th} = 10$ nJ per pulse, which is only around three times higher than the values demonstrated in dye-doped goblet resonators. This can be explained by a thinner gain layer thickness and the fact that the gain medium - when deposited by DPN - is only in the evanescent field of the supported optical modes, leading to reduced modal gain, compared to a resonator consisting of a PMMA matrix entirely doped with gain medium [138]. A typical lasing spectrum above threshold of the DPN-fabricated lasers is shown in Fig. 4.4 (c). The lasing occurs in multiple cavity modes and is qualitatively very similar to the lasing emission from dye-doped micro-lasers presented in the previous chapter (compare Fig. 3.12 (b)). Due to a spectral spacing between the lasing modes, which is clearly below the free spectral range of the resonator ($\Delta\lambda_{FSR} \approx 1.9$ nm), lasing most likely occurs in fundamental and higher order modes of the cavity. A drawback of utilizing a phospholipid matrix as host for a gain medium is the high mobility of the dye molecules within the matrix. The high mobility of the molecules leads to agglomeration and therefore fluorescence quenching upon optical excitation. The lasers fabricated by DPN were found to have operational lifetimes in the order of 10^3 pump pulses. Nevertheless, this lifetime is sufficient for sensing applications, as demonstrated in the next section.

4.1.3 Integration of gain and biofunctionality in phospholipid-coated microgoblets

In the aforementioned sections, DPN was applied either for surface functionalization or for deposition of gain material. By doping the carrier ink with biotinylated lipids

and rhodamine-doped lipids simultaneously, both lasing and sensing functionality could be added to passive microgoblets in a single fabrication step via DPN. The time-resolved shifts of microgoblet lasers – realized with this multi-functional ink with 4 mol% of biotinylated lipids and 1 mol% of dye-doped lipids – upon exposure to streptavidin solutions with concentrations of 500 and 50 nM are depicted in Fig. 4.5 (a) and (b), respectively. The total shifts resulting from the binding of streptavidin to the resonator surface inferred from Fig. 4.5 were 250 and 140 pm. These measurements prove that specific detection of molecules is feasible using passive microgoblets, where the functionality (lasing and sensing) was integrated by deposition of phospholipid ink via DPN. The shift of 250 pm for a streptavidin concentration of 500 nM (Fig. 4.5 (a)) is higher than the theoretically predicted shift of 180 nm, which was calculated assuming binding of a monolayer of molecules to the resonator surface (compare section 3.3.4). This could be explained by the three-dimensional structure of the multiple lipid bilayers, which enables binding of streptavidin molecules within several layers of the lipid ink. This effect is referred to as intercalation [139] and increases the sensitivity by at least 33%, in comparison to monolayer binding with optimum surface coverage.

4.1.4 Summary and conclusions

Dip-pen nanolithography was applied as fabrication technique to integrate gain onto pre-fabricated passive microgoblets made of PMMA. For this, a dye-doped ink based on phospholipids was employed as gain medium. The ink was added to the WGM resonators in a highly material-saving manner by solely coating the circumference of the resonators. Despite a highly efficient gain medium (rhodamine), lasing thresholds were found to be around 10 nJ for the DPN-fabricated lasers, which is around a factor of three higher compared to the intrinsically rhodamine-doped microgoblet lasers presented in the previous chapter (section 3.2.2). This can be explained by the lower gain experienced by WGMs in the ink-coated goblets, as the interaction of the modes with the gain medium only occurs via evanescent field.

Besides integration of gain, DPN allows for surface functionalization of microgoblets. Furthermore, even the simultaneous integration of gain and biofunctionality is feasible with this technique. To realize devices capable of lasing action and analyte-molecule selectivity in one single fabrication step, a lipid mixture consisting of three different components (carrier, dye-doped and biotinylated lipids) was employed. With these devices, the detection of streptavidin (500 nM) resulted in a shift of the lasing wavelength of 250 pm, which is more than a factor of three larger than for microgoblet lasers without surface functionalization (see section 3.3.4) and partly results from intercalation, a process observed in lipid multilayers [139].

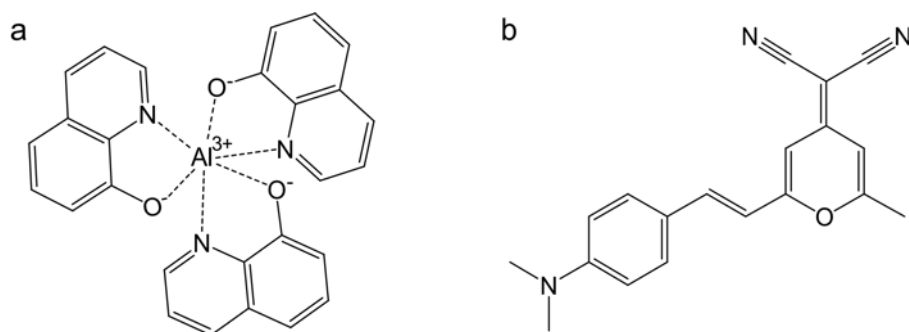


Figure 4.6: Chemical structure of the molecules (a) Alq₃ and (b) DCM.

As phospholipids are readily available with a large number of different functional head groups, diverse combinations of surface functionalization and lasing wavelengths can potentially be integrated on one single chip and fabricated in a flexible and material-saving manner [138].

4.2 Low-threshold lasing in organic semiconductor microgoblets

One of the major issues for the development of low-threshold lasers utilizing an extrinsic gain layer is the inherently small overlap of the WGMs of the passive resonator with the gain medium. This results in a low modal gain and fairly high lasing thresholds despite an efficient gain medium and a high-Q resonator, as discussed in the previous chapter for the case of dye-doped lipids on microgoblets. One possibility to overcome this limitation imposed on the lasing performance of WGM lasers with extrinsic gain layer is the employment of a gain material with a refractive index higher than the refractive index of the material of the passive cavity, such as organic semiconductors.

In this work, the organic semiconductor tris(8-hydroxyquinoline) aluminum (Alq₃) doped with the laser dye 4-dicyanomethylene-2-methyl-6-(p-dimethylaminostyryl)-4H-pyran (DCM) was investigated as gain medium on top of goblet microcavities. The influence of the film thickness of the Alq₃:DCM layer on the lasing properties was investigated by numerical analysis using finite element simulations. The numerical calculations were validated experimentally by optical characterization of the lasing performance of microgoblet devices with different gain layer thicknesses. In the following sections, the numerical treatment, as well as the experimental findings concerning the lasing properties of organic semiconductor microgoblets, is presented.

4.2.1 Guest-host organic semiconductors

The guest-host system Alq₃:DCM is a widely used organic solid-state gain medium [82, 140], where the small molecule host (Alq₃) is doped with the laser dye DCM. The chemical structures of both molecules are depicted in Fig. 4.6. This guest-host system is efficient gain medium due to overlapping absorption and emission spectra of DCM and Alq₃, respectively. This allows for an efficient fluorescence resonant energy transfer (FRET)¹ from the excited host to the dye dopant [82]. FRET is based on dipole-dipole interaction and the rate of this process τ_{dd}^{-1} for a distance r between donor and acceptor can be calculated as follows [141, 142]:

$$\tau_{dd}^{-1}(r) = \frac{1}{\tau_D} \left(\frac{r_0}{r} \right)^6 \quad (4.1)$$

where τ_D is the fluorescence lifetime of the donor and r_0 is the Förster radius. For distances $r < r_0$, τ_{dd} is far shorter than the fluorescence lifetime of the donor, so that the non-radiative Förster transfer is the dominating de-excitation mechanism in the donor molecule. For Alq₃, the fluorescence lifetime is around 15 ns [142]. For DCM-doped Alq₃, $r_0 = 3.2$ nm, which corresponds to three Alq₃ molecular diameters (1 nm) [142]. The timescale of the FRET mechanism is therefore between 20 ps and 2 ns.

Organic guest-host systems possess several advantages compared to utilizing a single type of dye molecule as gain medium. Firstly, energy transfer allows for separate modification and optimization of the optical properties of the guest and host molecules [142]. For example, the electron transporting Alq₃ cannot be directly used as gain medium, due to the low internal quantum efficiency of only 35% [142]. Hence, population inversion has not been achieved yet in undoped Alq₃ films [142]. On the other hand, DCM molecules have a quantum efficiency of around 100% and are a widely used gain medium [142]. Additionally, doping results in low concentrations of light-emitting dye molecules, which strongly reduces the quenching effects originating from agglomeration [142]. Another advantage resulting from FRET is the shift of luminescence to higher wavelengths, compared to the absorption band. The absorption band of Alq₃ (around 400 nm) and the emission band of DCM (around 600 nm) are spectrally separated by 200 nm, which strongly reduces the parasitic effect of self-absorption in this four-level laser system [142].

¹This process is often referred to as Förster energy transfer.

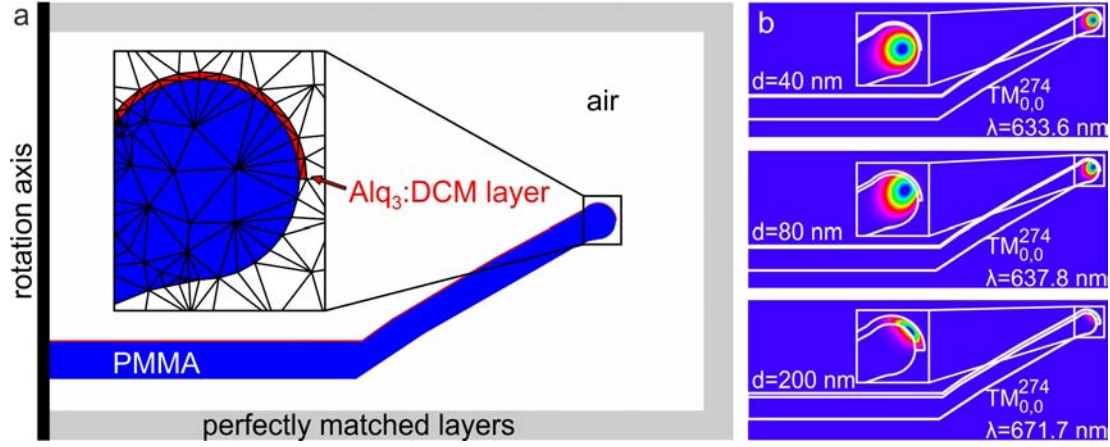


Figure 4.7: (a) Setup of the computational domain for simulation of the Alq₃:DCM layer on top of PMMA microgoblets. (b) Calculations of the $TM_{0,0}^{274}$ mode for the three gain-layer thicknesses $d=40$, 80, and 200 nm [65].

4.2.2 Simulation of WGMs with organic gain layer²

In order to numerically analyze the influence of an additional organic semiconductor coating with higher refractive index ($n(\text{Alq}_3:\text{DCM}) = 1.72$) than the PMMA cavity ($n(\text{PMMA}) = 1.49$) on the optical modes, finite element simulations were performed (compare section 2.2.5). An enlarged view of the resonator rim including the Alq₃:DCM layer and the triangulation of the structure is shown in Fig. 4.7 (a). The Alq₃:DCM layer covers the upper half of the microresonator due to deposition of gain material from above by thermal evaporation. The effect of the gain layer with high refractive index on the WGMs for three different thicknesses $d = 40$, 80 and 200 nm, which were also fabricated and characterized, is illustrated in Fig. 4.7 (b). For a thickness of $d = 40$ nm, the depicted intensity distribution of the fundamental $TM_{0,0}^{274}$ mode sparsely overlaps with the gain layer. The same WGM in a cavity with an 80 nm-thick Alq₃:DCM layer is located closer to the cavity surface, thus having a larger overlap with the active material. For a gain layer thickness of 200 nm, the mode is guided in the high index material, resulting in a significantly larger confinement factor of the mode in the gain layer, which is advantageous for reducing the lasing threshold due to a high modal gain.

In order to derive a quantitative method for determining the cutoff thickness, above which the mode is guided in the gain layer, the effect of an increasing gain-layer thickness on the resonance wavelengths, the mode volumes and the filling factors of

²The results presented in this section have been published in [65].

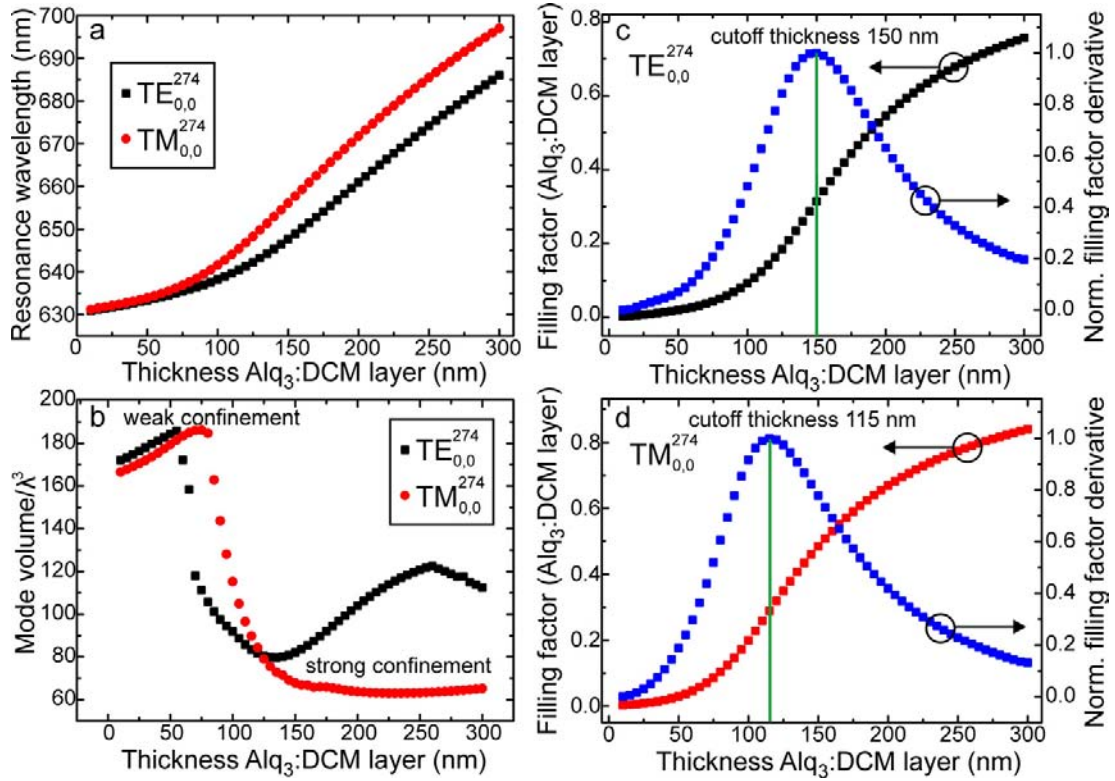


Figure 4.8: Results of finite element calculations showing (a) the resonance wavelengths, (b) the mode volumes and the filling factors of the (c) TE_{0,0}²⁷⁴ and (d) TM_{0,0}²⁷⁴ modes as function of the Alq₃:DCM-layer thickness [65].

the WGMs were investigated in finite element simulations, in which the gain-layer thickness is varied between 5 and 300 nm in steps of 5 nm. As already noted in Fig. 4.7 (b), the resonance wavelength of the same WGM increases with increasing thickness of the Alq₃:DCM layer, as the mode is shifted to the gain layer and thus propagates along a slightly larger radius with a higher effective refractive index. This property is depicted in more detail in Fig. 4.8 (a). Above a thickness of approximately 75 nm, the splitting between TE and TM polarization increases, which also indicates a movement of the WGM intensity distribution towards the cavity surface, as shown in Fig. 4.7 (b). Besides the effect of an increasing resonance wavelength, a change in the mode volume with increasing thickness of the gain layer can be observed in Fig. 4.7 (b). The mode volume as function of the Alq₃:DCM-layer thickness for the TM/TE_{0,0}²⁷⁴ mode is shown in Fig. 4.8 (b). For both modes, the mode volume drops above a certain gain-layer thickness, due to the localization in the Alq₃:DCM. This enables identification of a weak and a strong confinement regime, indicated in Fig. 4.8 (b). For the TM_{0,0}²⁷⁴ mode, the mode volume drops by a factor of three through the transition from weak to strong confinement. Although a change in resonance

wavelength and mode volume of the WGMs for larger thicknesses indicates guidance of the modes in the gain layer, a quantitative cut-off criterion cannot be inferred from these quantities. For this, the filling factor of the mode in the gain layer, defined as fraction of the electric energy density in the gain layer and the total electric energy density is investigated [143]:

$$F_g = \frac{\int_{gain} \epsilon(\vec{r}) |\vec{E}(\vec{r})|^2 dV}{\int_{total} \epsilon(\vec{r}) |\vec{E}(\vec{r})|^2 dV} \quad (4.2)$$

where the integration of the electric density in the numerator is performed within the gain layer and the denominator denotes the integration of the electric energy density within the entire computational domain. In this case, the filling factor F_g is a direct measure of the modal gain. The filling factor as function of the Alq₃:DCM-layer thickness for the fundamental TE and TM mode is depicted in Fig. 4.8 (c) and Fig. 4.8 (d), respectively. For both polarizations, the value of F_g is below 0.1 for gain-layer thicknesses under 100 nm. Above 100 nm, the filling factor strongly increases until saturation occurs for thicknesses above around 200 nm at values of $F_g = 0.8$. The strongest change in the filling factor occurs in the region where the mode changes its localization from the PMMA layer to the Alq₃:DCM layer. To visualize this, the derivative of the filling factor with respect to the thickness of the Alq₃:DCM layer is depicted in Fig. 4.8 (c) and Fig. 4.8 (d). The derivative of the filling factor has a maximum at a certain thickness, which can be identified as the cutoff thickness. Below and above this thickness the change in F_g drops as the mode is either guided in the PMMA or in the Alq₃:DCM layer. The cutoff thickness takes on values of 115 and 150 nm for the analyzed fundamental TM and TE modes, which feature resonance wavelengths within the spectral gain region of Alq₃:DCM.

4.2.3 Lasing properties of organic semiconductor microgoblets³

In order to experimentally investigate the simulated effects of the identified regimes of low and high modal gain on the lasing threshold, samples with gain-layer thicknesses of 40 (weak mode confinement below cutoff), 80 (transition region) and 200 nm (strong mode confinement above cutoff) were fabricated. Thermal co-evaporation of the organic semiconductor Alq₃ and the laser dye DCM (2.5 wt. %) on top of the microresonators was performed in a high vacuum evaporation chamber at a pressure

³The results presented in this section have been published in [65].

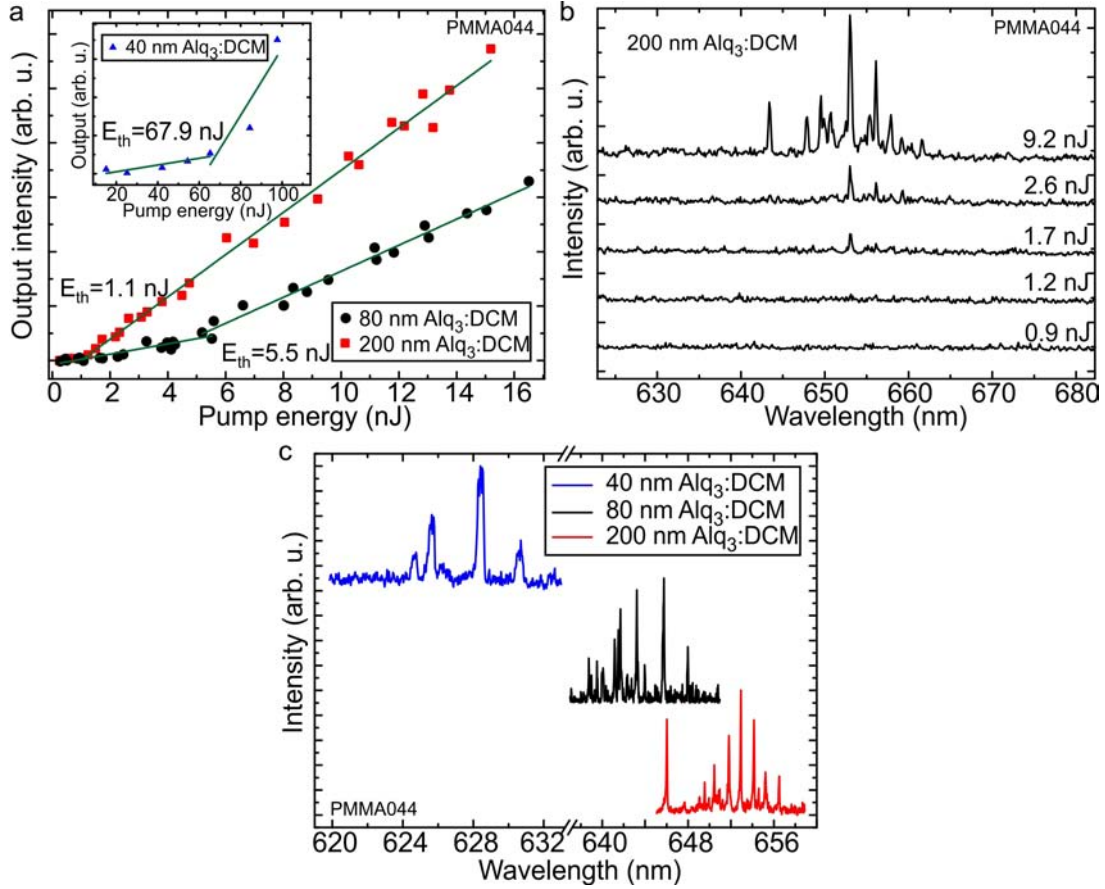


Figure 4.9: (a) Input-output curves of microgloblet lasers with lasing thresholds of 67.9, 5.5 and 1.1 nJ covered with 40, 80 and 200 nm Alq₃:DCM, respectively. (b) Emission spectra for increasing pump energy of the microgloblet laser with 200 nm Alq₃:DCM layer. (c) Comparison of the laser emission above threshold for the three Alq₃:DCM-layer thicknesses shows a red-shifted gain spectrum for thicker gain layers [65].

of 10^{-6} mbar. Afterwards, the samples were encapsulated in a quartz cuvette under nitrogen atmosphere in order to prevent photo-oxidation of the active material under optical excitation.

The microcavities were optically pumped from above using a neodymium-doped yttrium lithium fluoride (Nd:YLF) laser with pulse lengths < 5 ns at 349 nm. The emitted whispering-gallery laser light is collected in the plane of the microcavity by a multi-mode optical fiber connected to a spectrometer with CCD camera.

The input-output curves of optically pumped PMMA microgloblets covered with a 40, 80 and 200 nm thick Alq₃:DCM layer are shown in Fig. 4.9 (a), where the lasing threshold energies E_{th} were determined by the onset of a superlinear output. For

every excitation pump energy, a spectrum was acquired and integrated over the dominant laser line to obtain the output intensity. For the sample with 200 nm of Alq₃:DCM on top of the microcavities, the lasing threshold energy was found to be as low as 1.1 nJ per pulse. The corresponding emission spectra for increasing pump energy are depicted in Fig. 4.9 (b), showing the appearance of multiple lasing modes above threshold. As this gain-layer thickness is above cutoff, the lasing modes are guided in the high index material, resulting in a large filling factor of the modes in the gain layer. Based on typical values for the absorption of Alq₃ [144], the 200 nm thick gain layer is assumed to be nearly homogeneously pumped, so that many emitted photons experience amplification. This leads to a high modal gain and a reduced lasing threshold. For comparison with the regime below cutoff, two further Alq₃:DCM thicknesses (40 and 80 nm) were characterized. For a thickness of 80 nm, the lasing threshold ($E_{th} = 5.5$ nJ) increases by a factor of 5 compared to the threshold above cutoff and even increases to a value of approximately 67.9 nJ (factor of more than 60 compared to the sample with 200 nm Alq₃:DCM) for an Alq₃:DCM layer of 40 nm (see Fig. 4.9 (a)). Besides the effect of higher modal gain, increasing filling factors of the modes in the Alq₃:DCM layer lead to enhanced scattering of the WGMs at the DCM molecules and the inhomogeneities of the active medium. The low losses of the pristine cavity with Q-factors above 10^6 are assumed to be negligible compared to the loss mechanisms caused by the active layer. Therefore, the Q-factors of the Alq₃:DCM-covered microcavities are assumed to be reduced for increasing gain-layer thicknesses due to increased surface-scattering losses. Nevertheless, the measured lasing thresholds decrease with increasing gain-layer thickness, indicating an overcompensation of a decreased Q-factor by a strongly increased modal gain.

The low lasing threshold observed for microgoblets coated with 200 nm Alq₃:DCM enabled utilization of a low-cost and compact blu-ray laser diode as pump source. The laser diode was designed to operate at an output power of 150 mW (cw) at a wavelength of 405 nm, which is in the absorption band of Alq₃. By driving the laser diode with a pulsed current source with 20 ns pulses at a repetition rate of 500 Hz, pulse energies around 9 nJ were generated. This energy was sufficient to operate the organic semiconductor microgoblet laser above threshold. Further details on experiments with laser-diode operation of microgoblet lasers can be found in [96].

Besides the lasing threshold, the spectral position of the lasing spectrum was found to be influenced by the thickness of the gain layer. The envelope of the laser emission is shifted to larger wavelengths for increasing Alq₃:DCM-layer thicknesses (corresponding to decreasing lasing thresholds), shown in Fig. 4.9 (c). The observed behavior is attributed to increased absorption of dye molecules for thicker gain layers, due to an increased filling factor of the modes in the gain layer, and results in red-shifted net gain spectra of the laser dye. This is accompanied by a decrease of the lasing

thresholds due to an increased concentration of dye molecules within the WGMs. The same dependency between lasing spectrum and lasing threshold was also found for the dye-doped microgoblet lasers, discussed in section 3.2.2, and explained by the dye laser model stated in equation 3.5. To implement varying Alq₃:DCM-layer thicknesses into the dye laser model, the model could be modified such that the thickness of the gain layer enters equation 3.5 by a number density of dye molecules in the optical mode $n_t(d)$, which depends on the filling factor and therefore on the thickness of the gain layer.

4.2.4 Summary and conclusions

In summary, the organic semiconductor Alq₃:DCM with high refractive index was integrated as gain medium on top of passive, high-Q microgoblet cavities to overcome the inherent limitation of high lasing thresholds with extrinsic gain medium, resulting from a low modal gain. The effect of the additional gain layer on the WGMs was investigated numerically using finite element simulations. These simulations revealed that for increasing thickness of the gain layer, the filling factor of the mode in the gain layer increases continuously. A criterion for the cutoff thickness, above which the mode can be considered as guided in the gain layer, was found to be the maximum of the derivative of the filling factor with respect to the gain-layer thickness. For TE and TM modes the cutoff thickness was determined as 150 and 115 nm, respectively. Above the cutoff thickness, the modes can be considered as strongly confined, as the mode volume drops by a factor of three through the transition from weak to strong confinement for the case of TM modes. Microgoblet devices with different gain-layer thicknesses below and above cutoff were fabricated and characterized. The lowest lasing threshold was found to be 1.1 nJ for an Alq₃:DCM-layer thickness of 200 nm, which is above the cutoff thickness. This low threshold observed for microgoblet lasing modes in the strongly confined regime allows for optical pumping using a compact and low-cost laser diode, which is promising for the development of ultra-compact, integrated photonic devices.

Chapter 5

Photonic molecule lasers for enhanced light-matter interaction

In the previous chapters, the feedback mechanism of the presented microlasers is based on WGMs propagating in a single microgoblet cavity. The interaction of WGMs with the surrounding environment in these solid-state cavities occurs via the evanescently decaying electric field outside of the dielectric structure. The interaction of the mode with the environment is weak, as only a fraction of the energy density (in the order of several percent) of the WGMs (see section 3.3.2) is located in the evanescent field. The development of nano- and microstructures with enhanced light-matter interaction for applications such as cavity quantum electrodynamics (c-QED) or biosensing is therefore a major issue.

In this work, two different experimental approaches allowing for increased light-matter interaction in WGM microcavities were investigated. The first approach was based on cavities with liquid core to guide light, which were made of a nanoporous polymer. The interaction between optical mode and liquid analyte is strongly increased, as light and analyte are guided within the same physical volume, and the bulk refractive index sensitivity was found to be strongly increased compared to microgoblets. Details of the fabrication and optical properties of these nanoporous ring resonators are presented in appendix A and were published in [145]. A second method investigated in this work, which allows for an increased overlap of the modes with the environment, is the utilization of two optically coupled microcavities, which are often referred to as a photonic molecule (PM) [31].

The following chapter begins with an overview of the optical properties and applications of photonic molecules and photonic-molecule lasers. Subsequently, a lithographic fabrication method for the realization of strongly coupled polymeric mi-

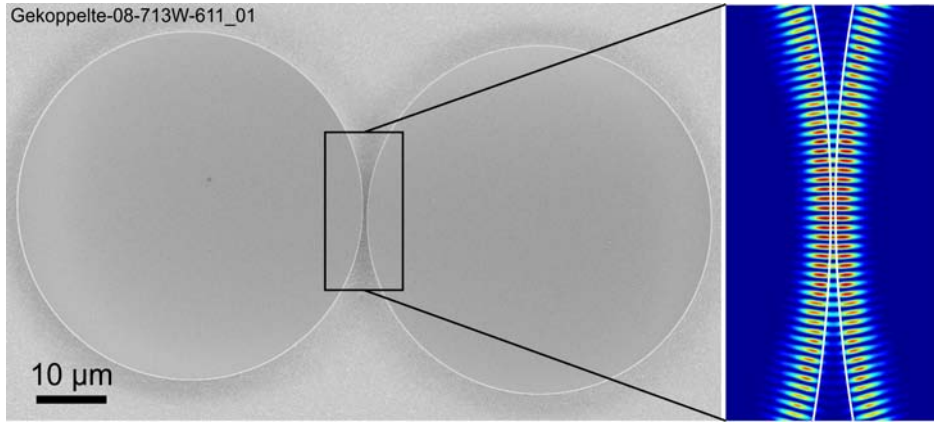


Figure 5.1: Scanning electron micrograph of a photonic molecule consisting of two coupled PMMA microdisks with radii of 25 μm . For coupling-gap sizes below 150 nm, field enhancements of the TE modes in the coupling zone can be observed, as shown in the distribution of the electric energy density on the right-hand side, which was inferred from finite element simulations.

rod disks is presented, which enabled coupling-gap sizes below 150 nm. The lasing properties of dye-doped PMs were investigated using spatially resolved microphotoluminescence (μPL) spectroscopy. This technique allowed for the direct imaging of WGMs in the photonic molecules, which were utilized for investigation of the so-called Vernier effect. Finally, PM lasing was investigated in aqueous environments, where single-mode lasing as well as an increased bulk refractive index sensitivity compared to single microcavities was observed, demonstrating the large potential of PMs for sensing applications.

5.1 Whispering-gallery modes in photonic molecules

Single microcavities are often referred to as photonic atoms, as the properties of the confined optical states are very similar to those of electrons in atoms [146]. For single spherical microcavities it was shown that the spatial distribution of the WGMs can be described by three quantum numbers n , l , and m , just like in the quantum mechanical description of the electronic orbitals in a hydrogen atom [147]. Optically coupled resonators are therefore often termed photonic molecules, due to the analogy between the optical modes of the coupled resonator system and the wavefunction of electrons in molecules [147], where electrons form bonding and antibonding molecu-

lar orbitals. The splitting of degenerate atomic states into bonding and antibonding orbitals occurs through interaction of atoms for small separation distances, such that the atomic orbitals overlap. In photonic molecules, bonding and antibonding modes with separation-dependent splitting were first observed by Bayer et al. in a pair of coupled pillar cavities [148]. In the meantime, photonic molecules have been realized in various photonic structures, such as photonic crystals [149] and WGM resonators like spheres [150–152] or disks [153]. In this work, photonic molecules consisting of two coupled PMMA microdisks standing on silicon pedestals were investigated. An image of such a PM is depicted in Fig. 5.1, showing a scanning electron micrograph of two coupled microdisks with radii of 25 μm .

Compared to single microcavities, PMs have the advantage that, besides the resonator geometry of the single cavity, the coupling-gap size can be additionally utilized to tailor the optical density of states. One application where utilization of PMs is beneficial is lasing. Here, PMs have two main advantages compared to single microcavities. Firstly, the radiation of PM lasers in the far field can be designed to be directional in the plane of the resonator [154]. A second advantage of PM lasers is the reduction of the spectral density of lasing modes without decrease of the Q-factor, which can be achieved by coupling two resonators with different radii (size-mismatched PM). The lasing emission can be tailored to be single mode [155, 156]. In addition to the density of states, also the spatial distribution of modes in PMs can be altered compared to single cavities. The evanescent coupling of TE modes for sufficiently small coupling-gap sizes can result in a significant field enhancement in the coupling gap region [32]. An example for such a TE mode with significant field enhancement is depicted on the right side of Fig. 5.1, showing the energy density of the mode in the coupling region. The overlap of the optical mode with the environment is significantly enlarged in this region. This could make photonic molecules attractive for applications where a large light-matter interaction is required, such as c-QED and biosensing [31].

5.1.1 Classification of supermodes in PMs

In contrast to single WGM microcavities, where the modes are totally classified by the three mode numbers N_ϕ , N_ρ , and N_z , PMs are additionally classified by their parity with respect to the PM axes. Similar to the case of electronic states in molecules, modes in PMs can be described by superposition of the two basis functions Ψ^+ and Ψ^- , which are standing waves that are phase shifted by $\phi = \pi/(2N_\phi)$ and are either symmetric (Ψ^+) or antisymmetric (Ψ^-) with respect to the plane of the major molecule axis. The resulting four linear combinations of the basis functions

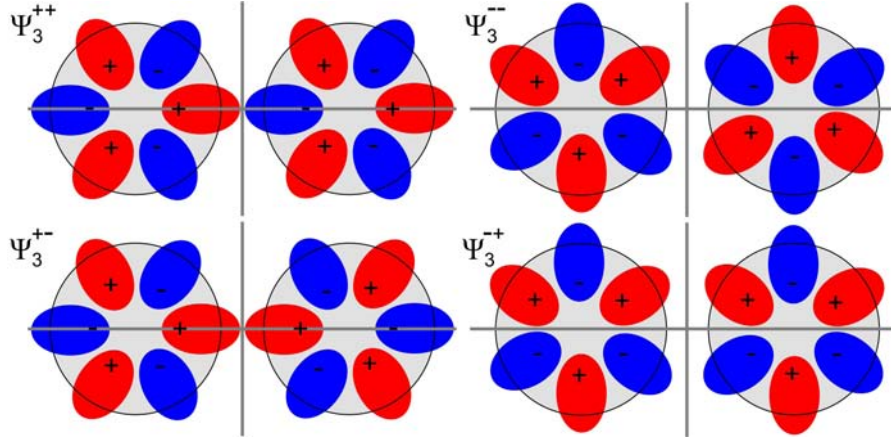


Figure 5.2: Visualization of the symmetry properties of the modes in photonic molecules for $N_\phi = 3$ [69]. The symmetry axes are marked by gray lines. In this case, the modes Ψ_3^{+-} and Ψ_3^{-+} are symmetric with respect to the vertical symmetry axis of the PM.

are:

$$\begin{aligned}
 \Psi_{N_\phi}^{++} &= \Psi_{N_\phi}^+ + \Psi_{N_\phi}^+ \\
 \Psi_{N_\phi}^{+-} &= \Psi_{N_\phi}^+ - \Psi_{N_\phi}^+ \\
 \Psi_{N_\phi}^{-+} &= \Psi_{N_\phi}^- + \Psi_{N_\phi}^- \\
 \Psi_{N_\phi}^{--} &= \Psi_{N_\phi}^- - \Psi_{N_\phi}^-
 \end{aligned} \tag{5.1}$$

An example for the case $N_\phi = 3$ is shown in Fig. 5.3, where the symmetry axes of the photonic molecule are marked by gray lines. The major PM axis is marked by the horizontal gray line. For odd (even) values of N_ϕ , $\Psi_{N_\phi}^{++}$ is antisymmetric (symmetric) and $\Psi_{N_\phi}^{+-}$ is symmetric (antisymmetric) with respect to the vertical PM axis. For small coupling-gap sizes the constructive (destructive) interference of the symmetric (antisymmetric) modes with respect to the vertical PM axis will result in the formation of bonding (antibonding) modes [157]. For large coupling-gap sizes, all the fields in equation 5.1 are degenerate. The degeneracy is lifted for small coupling-gap sizes, when the modes are delocalized in both microcavities. These modes are then called supermodes [31].

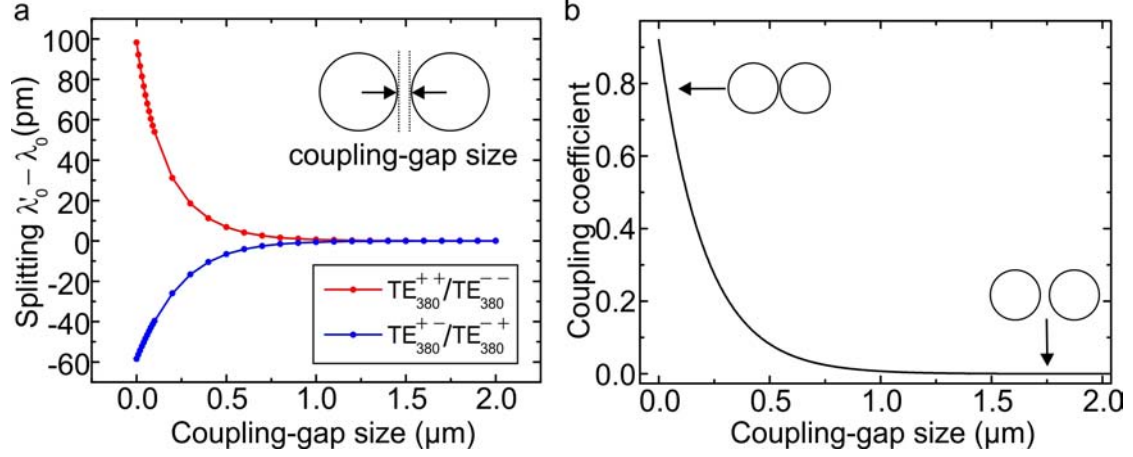


Figure 5.3: (a) Splitting between the resonance wavelength $\lambda'_0 = \{\lambda^{++}, \lambda^{+-}, \lambda^{-+}, \lambda^{--}\}$ and λ_0 with $N_\phi = 380$ for decreasing coupling-gap size of a photonic molecule consisting of two coupled resonators. The bonding (antibonding) modes are shifted towards larger (shorter) wavelengths for decreasing coupling-gap size [69]. (b) The inter-cavity coupling coefficient is strongly increased for coupling-gap sizes below 1 μm .

5.1.2 Supermodes in coupled polymeric microdisks

To investigate the effect of a decreasing coupling-gap size on the supermodes of PMs consisting of two coupled polymeric microdisks, finite element simulations were performed. Simulations of coupled resonators could not be performed by using the symmetry considerations of single resonators (compare section 2.2.5), due to the lack of a rotational symmetry of the entire PM. This results in a strongly increased computational effort compared to the case of single resonators. In order to reduce the computational costs as much as possible, only two resonators with identical geometry were simulated. This allows for using both PM axes (compare Fig. 5.2) as symmetry axes, which reduces the computational domain to 25% of the entire PM. Furthermore, the three-dimensional calculation was mapped onto two dimensions, by using an effective refractive index for the resonator material PMMA, which takes the finite height of the resonator in the direction orthogonal to the plane of the PM into account. Further details of the simulation method can be found elsewhere [69].

The single resonators of the simulated PM consisting of two identical microdisks had a radius of 55 μm . The coupling-gap size was varied between 2 μm and 0 in order to analyze the coupling-dependent spatial distribution of the energy density and the splitting between the bonding and antibonding modes. As field enhancements were only expected for TE modes, the fundamental modes $\{\text{TE}^{++}, \text{TE}^{+-}, \text{TE}^{-+}, \text{TE}^{--}\}$ with $N_\phi = 380$ and $N_\rho = 0$ were investigated. The resonance wavelength of these

modes for infinitely large coupling gap was $\lambda_0 = 1283$ nm. The resonance wavelengths split into the four wavelengths $\lambda'_0 = \{\lambda^{++}, \lambda^{+-}, \lambda^{-+}, \lambda^{--}\}$ for decreasing coupling-gap size. The splitting of the resonance wavelengths $\lambda'_0 - \lambda_0$ for decreasing coupling-gap size is depicted in Fig. 5.3 (a). In this case the medium surrounding the PM was air. The resonance wavelengths of the modes TE^{++} and TE^{--} are shifted to larger wavelengths for decreasing coupling-gap size. The energy of these modes is therefore decreased and the modes can therefore be considered as bonding modes of the photonic molecule. Analog to the case of electrons in molecules, the photons of bonding modes have an increased probability to be located in the coupling gap, which can result in field enhancements (compare Fig. 5.1). On the other hand, the modes TE^{+-} and TE^{-+} shift towards shorter wavelengths and are therefore considered as antibonding modes. From Fig. 5.3 (a) it can be concluded that the coupling-gap size needed to achieve significant splitting between bonding and antibonding modes in coupled polymeric microdisks has to be smaller than the resonance wavelength of the single resonator (in this case $\lambda_0 = 1283$ nm).

To determine the value of the inter-cavity coupling coefficient κ , which is a measure for the coupling strength between the two resonators forming the PM (see section 2.2.2), analytical calculations were performed. The coupling coefficient determines the fraction of the amplitude of the electric field which is coupled from one resonator to the other. An analytic expression for the coupling between two waveguides was derived by Little et al. [158], which can also be used to calculate the coupling strength between resonators [69]. The results for the calculation of κ for the PM consisting of two coupled microdisks with radii of $55 \mu\text{m}$ and a resonance wavelength of $\lambda_0 = 1300$ nm are depicted in Fig. 5.3 (b). For coupling-gap sizes below $1 \mu\text{m}$, the value of the coupling coefficient was found to be strongly increased, which is in good agreement with the observation of splitting between bonding and antibonding modes for coupling-gap sizes below $1 \mu\text{m}$ in Fig. 5.3 (a).

5.2 Fabrication of polymeric photonic molecules¹

The results from the previous section show, that in order to fabricate photonic molecules with strong inter-cavity coupling, sub-wavelength coupling-gap sizes are required. To realize PMs with coupling-gap sizes smaller than $1 \mu\text{m}$, two different approaches can be used: the photonic molecules can be either assembled manually or fabricated by lithographic structuring on a single substrate. The manual assembly of PMs consisting of two microcavities has been demonstrated for various different

¹The results presented in this section have been published in [159].

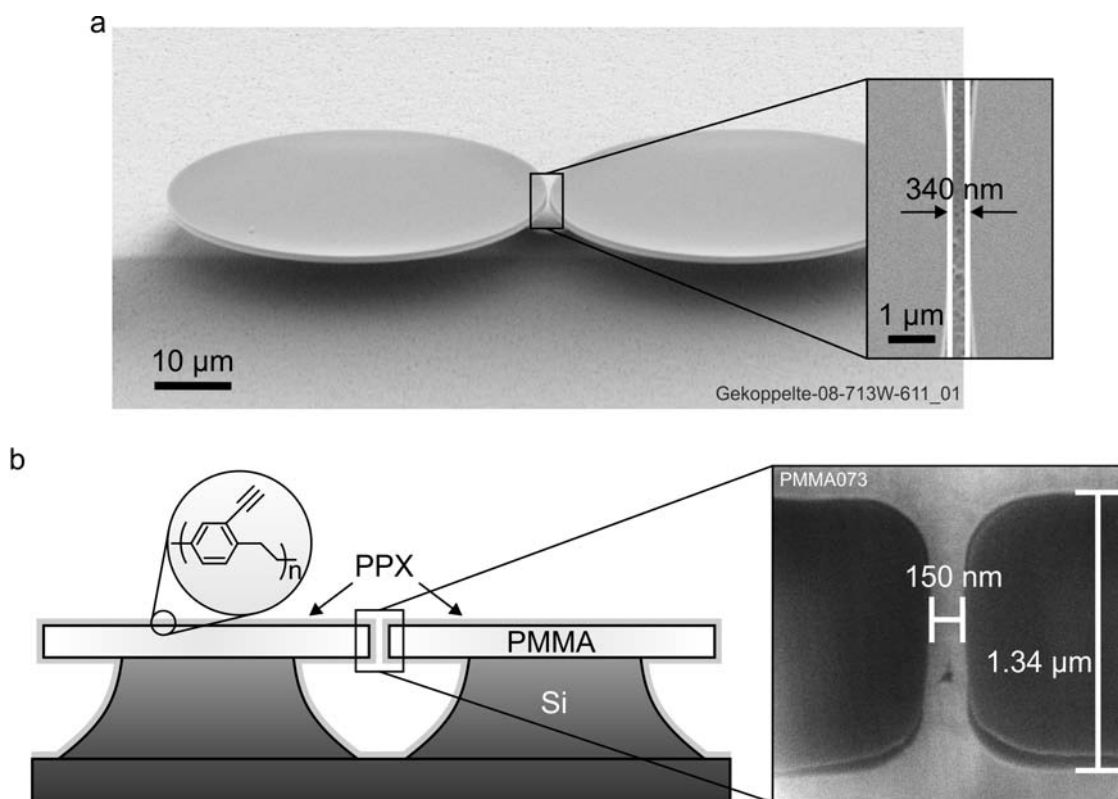


Figure 5.4: (a) Scanning electron micrograph of a photonic molecule consisting of two coupled microdisk resonators standing on silicon pedestals, each with radius of 25 μm, and with a coupling-gap width of 340 nm structured by e-beam lithography. (b) Deposition of an additional layer of PPX after the lithographic structuring can significantly decrease the coupling gap width below 150 nm. The inset shows a scanning electron micrograph of the cross-section of the coupling region at the minimal distance between the microdisks, which was fabricated by a focused ion beam cut [159].

cavity geometries, such as microtoroids [160,161], microdisks [162] and microgloblets [163]. One advantage of these systems is the possibility to tune the coupling-gap size. This allows for the precise investigation of the coupling-dependent properties of the modes of PMs, such as the coupling-dependent splitting of bonding and antibonding modes [161,163]. An additional advantage is the possibility to couple two high-Q resonators [160,163]. The main disadvantages of the flexible arrangement of coupled resonators is the lack of mechanical stability and the high positioning accuracy needed to adjust the coupling gap. The number of resonators which can be coupled simultaneously using manual alignment is therefore limited to two or three.

To overcome these disadvantages of manually arranged PMs, lithographic structuring of PMs was investigated in this work. Lithography furthermore enables precise

definition of the geometry of the structure and ensures large-scale production capability. The structuring of coupled polymeric microdisks was performed with the same fabrication process as used for the realization of PMMA microgloblets (see section 2.2.1), except that the thermal reflow was not carried out. A thermal reflow step would result in coupling-gap sizes of at least one micrometer, which is too large for achievement of strongly coupled resonators (compare Fig. 5.3 (a)). To achieve coupling between two microdisks, the sidewalls of the closely structured microdisks have to be vertical, such that the mode is located at the outer edge of the resonator. Angled sidewalls would lead to a shift of the mode towards the center of the resonator [41], which would decrease the coupling strength. With a PMMA thickness of about $1.2\ \mu\text{m}$, coupling-gap sizes as small as $340\ \text{nm}$ with vertical sidewalls were achieved by electron beam lithography. This corresponds to a microstructure aspect ratio (AR) of about 4:1. Scanning electron micrographs of a fabricated photonic molecule consisting of two PMMA microdisks is shown in Fig. 5.4 (a). The inset shows an enlarged view of the region of the coupling gap including the minimal distance between the resonators, which was measured to be $340\ \text{nm}$.

The finite element simulations of coupled microdisks showed that even smaller coupling-gap sizes (smaller than $200\ \text{nm}$) are needed to achieve significant field enhancements of TE modes in the coupling region [69]. For this, an additional process step subsequent to the lithographic structuring was developed, which resulted in the achievement of aspect ratios considerably above the resolution limit of conventional e-beam lithography with PMMA. Therefore, chemical vapor deposition (CVD) was employed to polymerize an additional, about $100\ \text{nm}$ thick layer of poly(*p*-xylylene) (PPX) with a functional alkyne group onto the resonators. Details of this CVD process have been described in literature [164]. PPX is a transparent polymer [165], which is often marketed under the name parylene, and is assumed to form a homogeneous layer on the PMMA resonators as well as on the surrounding silicon substrate. A schematic of the cross-section of the coupled resonators with parylene layer is depicted in Fig. 5.4 (b). With additional PPX layer, coupling-gap sizes below $150\ \text{nm}$ were realized. A scanning electron micrograph of a focused ion beam cut of the coupling region at the minimal distance between the two microdisks is shown in the inset of Fig. 5.4 (b). In this case, the coupling-gap size was measured to be $150\ \text{nm}$. The aspect ratio of the microstructure, here with a microdisk thickness of $1.34\ \mu\text{m}$, was 9:1. This is an improvement of more than a factor of two compared to the devices without additional polymer layer.

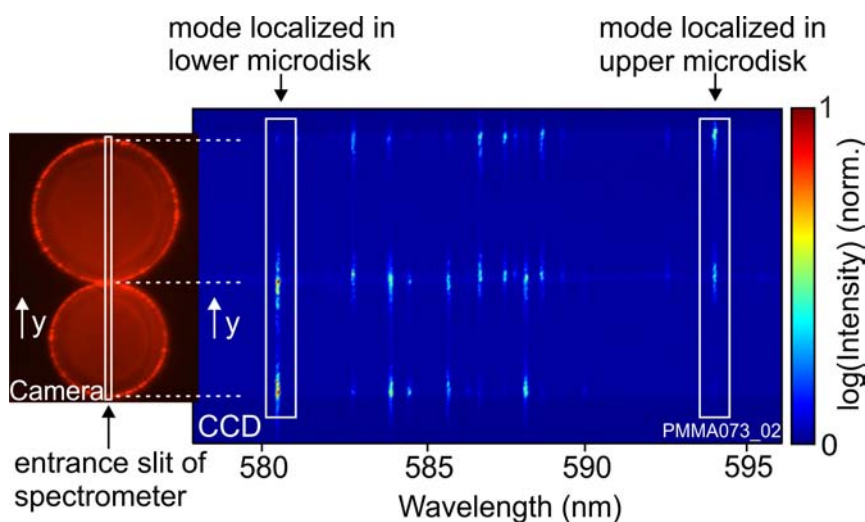


Figure 5.5: Images of WGM lasing in size-mismatched PMs (disk radii: 20 and 25 μm) with a coupling gap of 200 nm, made by the camera in front of the spectrometer and the CCD behind the spectrometer of the μPL setup. The camera in front of the spectrometer was used for the two-dimensional imaging of the spectrally integrated photoluminescence. The CCD behind the spectrometer detected the spectrally resolved photoluminescence with a spatial resolution in the vertical dimension. The emitted lasing spectra of both cavities vary due to their different sizes and weak inter-cavity coupling. Examples for modes, which are localized in either of the cavities, are marked with white rectangles [159].

5.3 Spectroscopy of supermode lasing²

Investigation of the optical properties of supermodes in coupled polymeric microdisks, such as the influence of the inter-cavity coupling strength on the mode localization, was performed using μPL spectroscopy of active PMs. This characterization method has the advantage that the localization of modes in the photonic molecules can be directly imaged without the use of elaborate and slow scanning techniques, such as near-field scanning optical microscopy (NSOM) [166].

For fabrication of active PMs, the dye PM597 was mixed into the PMMA resist with a concentration of 25 $\mu\text{mol/g}$ solid PMMA, which was also used for fabrication of dye-doped microgoblet lasers (compare section 3.2.3), before lithographic structuring. In order to excite and spatially resolve the lasing emission of the fabricated PM lasers, the μPL setup depicted in Fig. 3.7 and described in section 3.2.2 was used. In addition to spectrally resolving the emission from the sample, the setup also spatially resolved the emitted light along the vertical direction, denoted as y-axis

²The results presented in this section are submitted for publication [159].

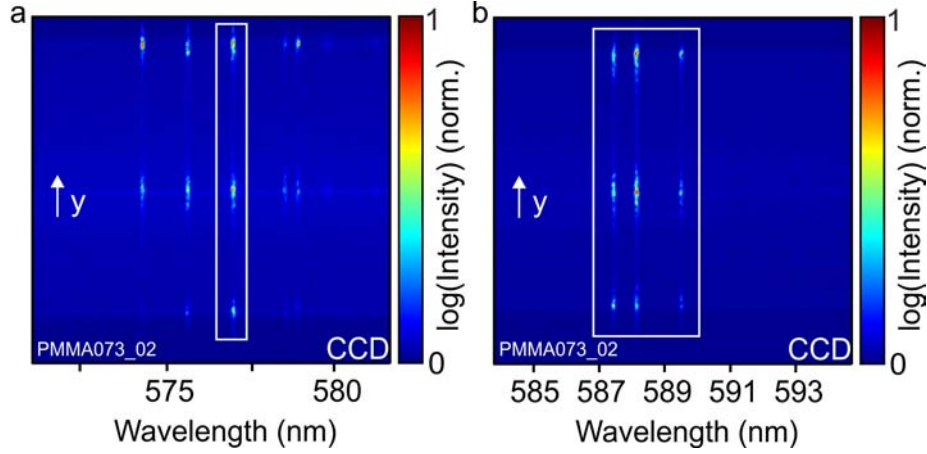


Figure 5.6: Section of the lasing spectrum of a PM (a) with a coupling-gap width of 120 nm and (b) without coupling gap, where the resonators are just in contact. For increased inter-cavity coupling, delocalized lasing modes exist (marked by a solid white rectangle) [159].

in Fig. 5.5. By aligning the spectrometer entrance slit with the PM's major axis (compare Fig. 5.5), the emission from a several micrometer wide strip of the central region of the PM was imaged onto the CCD behind the spectrometer. This allowed for simultaneous recording of the WGM lasing from both ends of the PM as well as from the coupling region, resulting in three vertically separated lasing spectra on the CCD camera attached to the spectrometer.

An example for spatially resolved lasing spectra of a PM consisting of two coupled microcavity lasers with radii of 20 and 25 μm and with a coupling gap of around 200 nm is depicted in Fig. 5.5. In this case, the sample was pumped with an energy of 30 nJ per pulse. Comparison of the lasing spectra from both ends of the PM in Fig. 5.5 clearly shows that both microcavities supported different lasing modes with differing gain spectra and differing cavity modes. Two examples of cavity modes, which were localized in solely one of the microdisks, are marked by solid white rectangles in Fig. 5.5. These lasing modes with high intensity in one cavity showed only weak photoluminescence intensity in the other cavity. Despite weak optical coupling between the resonators, no significant field build-up in the other microdisk occurred. This can be attributed to the different cavity sizes and hence differing resonance wavelengths of both resonators. Both microdisks can therefore be considered as independent lasers.

The mode localization in the investigated PMs was found to change for coupling-gap widths smaller than 200 nm, where lasing modes with equal intensities at both ends

of the PM were observed. An example for this case is depicted in Fig. 5.6 (a). Here, the coupling-gap width of the PM was 120 nm. A lasing mode (marked by a solid white rectangle) with high relative intensities in both cavities was observed and can thus be considered as a delocalized supermode, which extends over both resonators by the tunneling of photons in the coupling region. The other lasing modes depicted in Fig. 5.6 (a) showed weak PL in the lower microdisk, indicating that the modes were only resonant in the upper cavity. For even smaller coupling gaps, the number of delocalized lasing modes increased. A part of the lasing spectrum recorded for a PM where the resonators were just in contact is shown in Fig. 5.6 (b). Here, all observed lasing modes were delocalized in both cavities due to the strong optical coupling.

5.4 Vernier effect in photonic molecule lasers³

In addition to the localization of lasing modes, also the number of lasing modes in size-mismatched microdisks strongly depends on the coupling-gap width. A reduction of lasing modes through coupling of resonators with different free spectral ranges is termed the Vernier effect [155, 156, 167, 168]. A schematic explaining this effect is depicted in Fig. 5.7 (a). Due to the different free spectral ranges of both cavities, the resonances of both cavities are only identical for a single wavelength (marked gray). This mode experiences low optical losses in both cavities. Strong coupling of these size-mismatched cavities therefore results in high losses of those modes which are only resonant in either of the cavities. In this case, the coupling to the other cavity is an additional loss mechanism. On the other hand, modes which are resonant in both cavities do not experience this additional energy loss. In active PMs, the modes which are resonant in both cavities have a reduced lasing threshold compared to the modes which are only resonant in either of the cavities. The Vernier effect can therefore be utilized for realization of single-mode lasers [155, 156]. The extended free spectral range $\delta\lambda_{FSR,V}$ of the PM due to the Vernier effect is then given by the following expression [155, 156]:

$$\delta\lambda_{FSR,V} = \frac{\lambda^2}{\pi n_{eff}(D_1 - D_2)} \quad (5.2)$$

where D_1 and D_2 are the diameters of the coupled resonators. In this work, coupled microdisks with diameters of $D_1 = 50 \mu\text{m}$ and $D_2 = 40 \mu\text{m}$ were investigated. The ratio of the diameters is therefore $D_1/D_2 = 5/4$. This allows for a high interstitial

³The results presented in this section are submitted for publication [159].

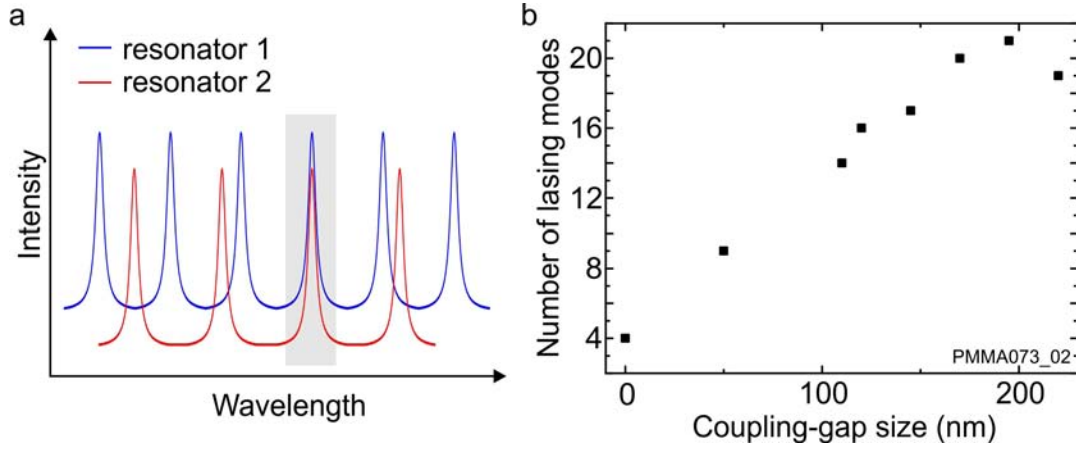


Figure 5.7: (a) Schematic of the Vernier effect resulting from coupling of resonators with different free spectral ranges. The resonances of both cavities are only identical for a single wavelength (marked gray). This mode has low losses in both cavities. (b) Investigation of the coupling-dependent Vernier effect in size-mismatched PMs with radii of 20 and 25 μm . The number of lasing modes strongly decreased for coupling-gap widths below 150 nm [159].

peak suppression without splitting of the resonance. More information for the ideal design of a Vernier filter can be found in literature [168, 169]. The extended free spectral range in this case was $\delta\lambda_{FSR,V} \approx 8 \text{ nm}$ at a wavelength of 600 nm, which is about a factor of four larger compared to the case of a single microcavity.

To study the coupling dependency of the Vernier effect, size-mismatched PM lasers with coupling-gap widths varying from 0 to 200 nm in steps of about 25 nm were investigated. A quantitative analysis of the suppression of lasing modes of the PMs was performed by counting the total number of laser modes in the spectrum acquired by pumping all PMs with an energy of 30 nJ. These PMs with varying coupling-gap widths were all fabricated on a single substrate using the fabrication method described in section 5.2. The effect of a decreasing coupling gap on the number of lasing modes of the PM is depicted in Fig. 5.7 (b), where the number of lasing modes includes the modes of both microdisks. For coupling gap widths above 150 nm the number of lasing modes was almost constant and no suppression of laser modes could be observed. Below 150 nm a significant decrease of the number of lasing modes was observed. Decreasing the coupling-gap width resulted in an increase of coupling loss and hence in a decrease of the Q-factor of the WGMs. This resulted in an increased lasing threshold, causing suppression of lasing modes which were not resonant in both cavities. Comparison of the number of modes for the largest and smallest coupling-gap widths showed a decrease up to a factor of five. This

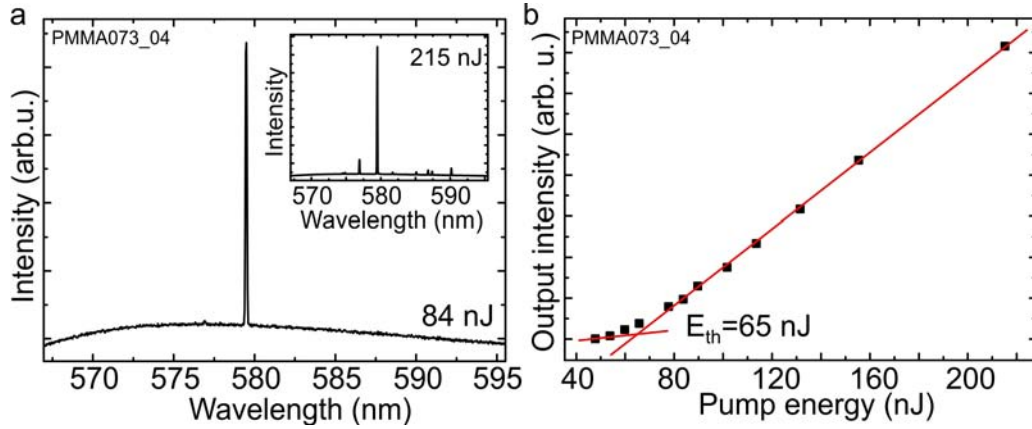


Figure 5.8: (a) Single-mode lasing from size-mismatched PMs in aqueous environment. (b) The lasing threshold for the laser mode is around 65 nJ. The coupling-gap width of the PM in this case was around 300 nm [159].

indicates that efficient suppression of laser modes in size-mismatched cavities only occurs above a certain coupling strength and seems to have a threshold-like behavior. The coupling constant κ (describing the inter-cavity coupling strength) was found to strongly increase above 150 nm and took on values from 0.05 to 0.2 for coupling-gap widths from 150 nm to 0. The threshold-like behavior of the suppression of lasing modes in size-mismatched PMs can therefore be directly related to an increase of the inter-cavity coupling strength. The observation of the Vernier effect in PMs for coupling-gap widths below 150 nm is therefore consistent with the measurement of delocalized lasing modes (compare section 5.3) in the regime of strong coupling.

5.5 Photonic molecules for sensing applications⁴

To determine whether the modes in the experimentally realized strongly coupled PMs have an increased overlap with the environment as predicted in theory [30,31] and to demonstrate the potential use of these devices for sensing applications, the lasing properties of PMs were investigated in aqueous environments. The lower refractive index contrast between cavity and aqueous solution reduces the overall number of lasing modes compared to the situation in air, as already discussed for the case of single resonators in section 3.3.3. Furthermore, the evanescent fields of the WGMs are extended further into the aqueous medium, leading to a stronger coupling between the resonators. In water, delocalized lasing modes were observed

⁴The results presented in this section are submitted for publication [159].

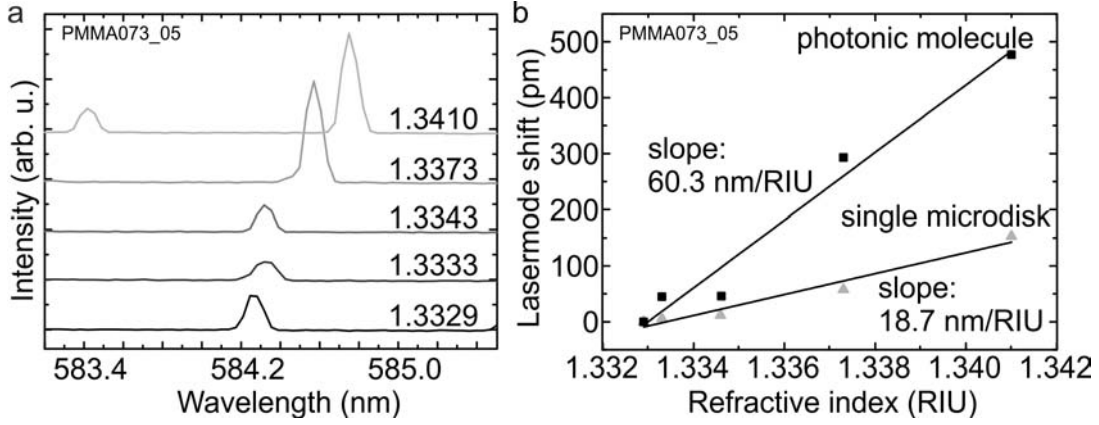


Figure 5.9: (a) Section of the spectrum of a PM laser recorded for different refractive index solutions denoted on the right hand side. The lasing mode shifts towards longer wavelengths for increasing refractive index. (b) The bulk refractive index sensitivity of a PM ($S \approx 60$ nm/RIU) was found to be about a factor of three larger than for a single resonator ($S \approx 19$ nm/RIU).

for coupling-gap widths of 300 nm and smaller. Additionally, pronounced single-mode lasing was achieved. A lasing spectrum showing single-mode operation is depicted in Fig. 5.8 (a), recorded at a pump energy of 84 nJ. The single-mode lasing was still apparent at higher pump energies, indicating a very efficient suppression of lasing modes. The inset of Fig. 5.8 (a) depicts a lasing spectrum recorded at a pump energy of 215 nJ, which is more than three times the value of the lasing threshold of 65 nJ, determined from the input-output characteristics of the laser mode at 579 nm (Fig. 5.8 (b)). Although several side modes appeared at high pump energies, the intensity of the dominating lasing mode was still more than six times higher than the most intense side mode. This indicates that almost all the pump energy was transferred into the dominating mode, due to effective suppression of side modes.

To analyze the overlap of the supermodes with the surrounding medium, measurement of the bulk refractive index sensitivity of PMs was performed analog to the case of single microgoblet lasers (compare section 3.3.3). For this, size-matched PMs (resonator radii of 25 μm) were used. A section of the lasing spectra of a strongly coupled PM, where the microdisks are just in contact, for different refractive index surroundings is shown in Fig. 5.9 (a). The depicted supermode shifted towards longer wavelengths for increasing refractive index of the surrounding. The shift of this lasing mode for varying refractive index is depicted in Fig. 5.9 (b). A bulk refractive index sensitivity of $S = 60.3$ nm/RIU was inferred from the slope of the linear fit. As reference, the shift of a single microdisk with a radius of 25 μm without parylene layer is also shown in Fig. 5.9 (b). The BRIS of the single microdisk was

$S = 18.7 \text{ nm/RIU}$ and therefore about a factor of three lower than for the supermode of the PM. This could indicate that the supermodes of PMs have an increased overlap with the environment. To validate this first finding, additional measurements have to be performed to entirely exclude that the increased BRIS stems from an uncontrolled modification of the parylene layer in aqueous environments, such as swelling, rather than from the advantageous spatial distribution of modes in strongly coupled photonic molecules.

5.5.1 Summary and conclusions

In this chapter the lasing properties of two optically coupled microdisks forming a photonic molecule as well their application for sensing were investigated. To realize coupling-gap widths below 200 nm, which allow for strong inter-cavity coupling, a fabrication step involving chemical vapor deposition of an additional polymer layer after the lithographic structuring was developed. Aspect ratios of the microstructure in the coupling region above 9:1 were achieved, which is significantly higher than using solely e-beam lithography. The spatial distribution of supermodes in active PMs were studied via μPL spectroscopy. With this method, the localization of the lasing modes in PMs was analyzed. The lasing modes were found to be delocalized in both cavities for strong inter-cavity coupling, which occurred in PMs with coupling-gap widths below 150 nm. In the regime of strong optical coupling, the Vernier effect was demonstrated using size-mismatched PMs consisting of two coupled microdisk lasers with different free spectral range, which enabled significant suppression of lasing modes. In aqueous environments, single-mode lasing was achieved and first indications of an increased bulk refractive index sensitivity of supermodes compared to modes in photonic atoms were observed. This originates from an enlarged overlap of the electric field of supermodes with the surrounding environment.

Chapter 6

Summary

In the focus of this work was the development of efficient, on-chip laser sources based on polymeric whispering-gallery-mode resonators with high quality factors in combination with organic gain materials. A promising application of these devices is the label-free detection of molecules. Within this work, two different photonic microstructures with promising optical properties for sensing applications were developed, optically characterized and utilized for sensing experiments: microgoblet resonators and photonic molecules consisting of two coupled microdisks.

To realize microlasers with highly desirable properties, such as a low lasing threshold and spectrally narrow laser lines, two main issues had to be addressed. Firstly, the dominating surface-scattering loss mechanism in lithographically structured microcavities had to be reduced. For this, polymeric microgoblets were developed as a type of optical whispering-gallery-mode microcavity with high quality factor. The surface-tension induced, goblet-shaped cavity geometry was fabricated by thermal reflow of PMMA microdisks standing on silicon pedestals [23]. The low glass-transition temperature of PMMA enabled thermal reflow at temperatures slightly above 100 °C, which is around one order of magnitude lower compared to temperatures needed for reflow of SiO₂, and allows for large-scale fabrication of these polymeric devices. The reflow process resulted in a smooth cavity surface and strongly reduced surface-scattering losses. The Q-factors of the passive PMMA cavities took on values as high as 3×10^6 , which was around one order of magnitude larger than before thermal reflow. The high optical quality of polymeric microgoblet resonators and the simple integration of gain medium within polymeric host matrices formed an ideal basis for the development of on-chip lasers with low thresholds.

The second objective, which had to be addressed within this work besides a high resonator quality, was the integration of an efficient gain medium within the cavity.

Organic laser dyes were found to be a suitable gain medium, due to good compatibility with polymeric host matrices, high internal quantum yield, and a large oscillator strength. In this work, the dyes rhodamine 6G and pyrromethene 597 were employed as gain media within microgoblets. The lasing properties were characterized using a free-space excitation and detection setup with a pump laser with nanosecond pulses in the quasi-cw regime. The lasing threshold and the spectral position of the gain curve of dye-doped microgoblet lasers were found to strongly depend on the dye concentration. These concentration-dependent lasing properties were explained by a standard dye-laser model including a concentration-dependent Q-factor. The lowest lasing threshold of rhodamine-doped microgoblets was 3 nJ [25]. Even lower lasing thresholds of 0.5 nJ were achieved for microgoblet lasers doped with pyrromethene 597. In addition to a high lasing efficiency, pyrromethene-doped microgoblets were found to have an operational lifetime of more than 2×10^6 pump pulses, corresponding to an operation time of several hours at a repetition rate of several Hertz. This operational lifetime is sufficient for many applications, such as biosensing, where the detection of molecules typically occurs within a time frame of several seconds or minutes.

To demonstrate the applicability of dye-doped microgoblet lasers for label-free molecule detection, these devices were operated and characterized in aqueous environments. Due to additional radiation losses originating from a reduced refractive index contrast compared to operation in air, the lasing threshold of pyrromethene-doped microgoblets increased to a value of 1.6 nJ. An important quantity for characterization of the sensing properties is the bulk refractive index sensitivity (BRIS), which is a measure for the overlap of the optical mode with the surrounding environment [118]. A value for the BRIS of 23 nm/RIU was obtained at a lasing wavelength of 630 nm. This is in good agreement with the value of the BRIS inferred from finite element simulations. First proof-of-principle experiments for the label-free detection of molecules were carried out by detection of the protein streptavidin. For this, the binding of molecules to the resonator surface was monitored by recording the time-resolved shift of the lasing mode. Without surface functionalization, shifts of around 70 pm were measured for a streptavidin concentration of 500 nM. The lowest detectable protein concentration using the spectrometer-based detection setup was estimated to be 2 nM.

Besides integration of gain within the polymeric host matrix, two different fabrication techniques for the realization of an extrinsic gain layer on microgoblets were investigated. Both approaches allow for the local deposition of an active material onto a chip. In the first approach, dip-pen nanolithography was applied to integrate gain on passive microgoblets. For this, a rhodamine-doped ink based on phospholipids was employed as gain medium. The ink was added to the WGM resonators in

a material-saving manner by solely coating the circumference of the resonators. The values of the lasing threshold of these devices were about 10 nJ, which is around a factor of three higher compared to the microgoblet lasers where the polymer was intrinsically doped with rhodamine. The increased threshold can be explained by the lower modal gain experienced by WGMs in the ink-coated goblets, as amplification of the modes only occurs within the evanescent field.

The aforementioned limitation of a low modal gain originating from an extrinsic gain layer was overcome by utilizing an active medium with high refractive index. In a second approach for the realization of an extrinsic gain layer, the organic semiconductor Alq₃:DCM was evaporated onto passive microgoblet cavities. The effect of an additional organic layer with high refractive index on the optical properties of the WGMs was investigated numerically using finite element simulations. These simulations revealed that, for increasing thickness of the gain layer, the filling factor of the mode in the gain layer increases continuously. A criterion for the cutoff thickness, above which the mode can be considered as guided in the gain layer, is the maximum of the derivative of the filling factor with respect to the gain-layer thickness. Above this cutoff thickness, the modes can be considered as strongly confined in the gain layer, as the mode volume decreases by a factor of three through the transition from weak to strong confinement. To experimentally validate these findings, microgoblet lasers with Alq₃:DCM-layer thicknesses below and above cutoff were fabricated and their lasing properties characterized. The lowest measured value of the lasing threshold was 1.1 nJ for an Alq₃:DCM-layer thickness of 200 nm, which is above the cutoff thickness [65]. The high modal gain of lasing modes in the strongly confined regime in combination with the efficient gain medium Alq₃:DCM allowed for lasing operation using a compact and low-cost laser diode as pump source [96].

In addition to lasers based on microresonators with high quality factors, photonic molecules (PMs) formed by coupled microdisks were investigated as resonator structure for lasers in this work. Numerical simulations have predicted highly promising optical properties of photonic molecules for sensing applications [170], such as an increased overlap of the electric field with the surrounding medium [30]. In this work, the lasing properties of two optically coupled microdisks forming a photonic molecule as well their application for sensing were investigated. To realize coupling-gap widths below 200 nm, which allow for strong inter-cavity coupling, a fabrication step involving chemical vapor deposition of an additional polymer layer after the lithographic structuring was developed. Aspect ratios of the microstructure in the coupling region above 9:1 were achieved, which is significantly higher than using solely e-beam lithography. The spatial distribution of supermodes in active PMs were studied via microphotoluminescence spectroscopy. With this method, the localization of the lasing modes was analyzed. The lasing modes were found to be

delocalized in both cavities for strong inter-cavity coupling, which occurred in PMs with coupling-gap widths below 150 nm. In the regime of strong optical coupling, the Vernier effect was demonstrated using size-mismatched PMs consisting of two microdisks with different free spectral ranges, which enabled significant suppression of lasing modes. In aqueous environment, single-mode lasing was achieved and first indications of an increased bulk refractive index sensitivity of supermodes compared to modes in photonic atoms were observed.

Conclusions and Outlook

The operation of polymeric microgoblet lasers – with lasing thresholds in the order of several nanojoule – using a compact and low-cost laser diode demonstrates that these on-chip lasers are a highly efficient source of coherent light. In combination with the demonstrated applicability for label-free biosensing, these lasers could form the basis for the development of compact integrated systems for the label-free detection of molecules. In future experiments the detection limit could be improved significantly using self-heterodyne beat note measurements, discussed in section 3.3.2, instead of tracking the laser peak via spectrometer, where the linewidth of the microgoblet lasers is limited by the spectrometer resolution. These on-chip microgoblet lasers realized on a low-cost polymer-on-silicon platform can be fabricated on a large scale and could pave the way for the development of compact and possibly even hand-held devices for the highly sensitive, label-free detection of single molecules, which is the ultimate goal for label-free biosensors [27].

The polymeric photonic molecules developed in this work could be advantageous for a multitude of applications requiring strong light-matter interaction besides sensing, such as cavity quantum electrodynamics. A promising experimental realization could involve the placement of emitters in the coupling-gap region, where significant field enhancements can be expected. The presented lithographic fabrication method of PMs could allow for realization of large arrays of strongly coupled, on-chip cavities with precisely defined coupling-gap sizes, which is of great interest for the investigation of new regimes in quantum optics [14,171]. Furthermore, the additional polymer layer involved in the fabrication of PMs not only reduces the coupling-gap width but also provides chemical end-groups on the PM surface and the surrounding silicon and can thus serve as the starting layer for the surface functionalization for the label-free detection of target molecules as well as for the solventless adhesive bonding of additional microfluidic elements onto the silicon substrate [172], making the presented approach highly interesting for the realization of integrated optofluidic devices.

Appendix A

Nanoporous liquid-core lasers¹

As already discussed in chapter 5, the interaction of WGMs with the surrounding environment in the solid-state cavities presented in the previous chapters occurs via the evanescently decaying electric field outside of the dielectric structure. An interesting class of microcavities which allow for a high overlap of the optical modes with the analyte are liquid-core waveguides (LCW) or resonators. In these optofluidic structures, the liquid analyte forms the core of the waveguide, enabling increased light-matter interaction [46, 173]. A promising approach for the realization of LCWs is based on nanoporous polymers (NP) [174, 175]. The waveguide core consists of a NP with hydrophilic end-groups infiltrated by a liquid and the cladding is formed by a hydrophobic NP without liquid. Therefore, the core is a solid-liquid alloy and these waveguides are termed solid-liquid core waveguides (SLCWs). The refractive index contrast between core and cladding in this configuration is around 0.16 RIU [175]. Therefore, LCWs are suitable for the fabrication of optofluidic microcavities. In the following chapter, the investigation of optofluidic ring resonator lasers based on LCWs for sensing applications is presented.

For the fabrication of liquid-core ring resonators, polymer films consisting of nanoporous 1,2-polybutadiene were used. Details of the preparation of these films have been described in previous work [175, 176]. The typical pore diameter is around 14 nm and the porosity of the material is ca. 44% [174]. In order to hydrophilize the hydrophobic surface of the nanopores, photo-grafting of thiol compounds containing hydrophilic groups onto the inner surface of the nanopores was applied. As exposure method to define hydrophilic regions within nanoporous polybutadiene, direct

¹The work on optofluidic ring resonators was performed in collaboration with the Department of Micro- and Nanotechnology/DTU Nanotech at the Technical University of Denmark (DTU). The results presented in this chapter have been published in [145].

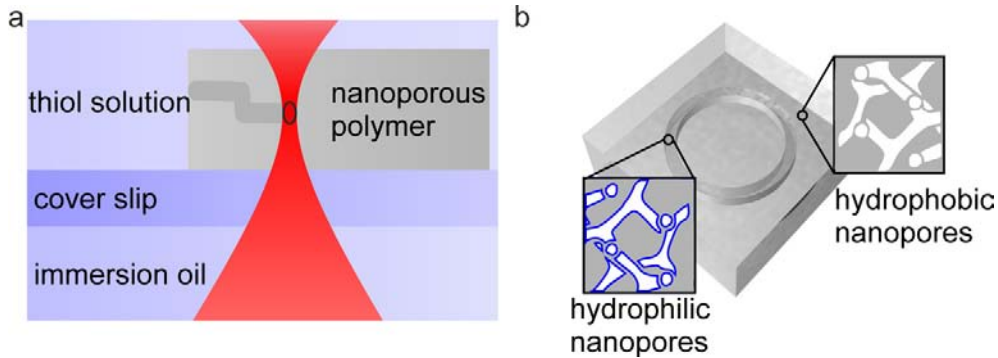


Figure A.1: (a) Schematic of the layer system used for fabrication of nanoporous ring resonator lasers via DLW. (b) Schematic of the sample after the exposure. The exposed areas contain hydrophilic nanopores and are embedded within the hydrophobic nanoporous polymer [145].

laser writing (DLW) based on two-photon absorption was applied². This exposure technique allows for three-dimensional control of the resonator geometry with a lateral resolution of several hundred nanometers [177]. During the exposure via DLW, the NP was immersed in a thiol solution containing a photoinitiator for initiation of the reaction of mercaptosuccinic acid with the inner surface of the nanopores. A schematic of the layer system used for the exposure is depicted in Fig. A.1 (a). The laser beam passes the immersion oil and the cover slip before it is focused into the transparent polymer sample, which is immersed in the thiol solution. Rings with a diameter of $150\ \mu\text{m}$ and a width of $5\ \mu\text{m}$ with a thickness of $10\ \mu\text{m}$ were exposed. A schematic of such a ring after the exposure is shown in Fig. A.1 (b). The exposed ring contains hydrophilic nanopores and are embedded within the hydrophobic nanoporous polymer.

After the lithographic definition of the hydrophilic rings, the entire polymer matrix was doped with the laser dye rhodamine 6G. In order to guide light in the liquid-core resonator, the exposed ring has to be infiltrated with water. A waterfilm on top of the substrate is already sufficient to cause condensation of evaporated water within the ring and to infiltrate the hydrophilic nanopores (see Fig. A.2 (a)). The infiltrated region has a refractive index of 1.42, which is about 0.16 RIU higher than the hydrophobic regions without water and thus sufficient to guide light [178]. A microscope image of an exposed ring with a water film on top of the sample is

²The utilization of direct laser writing for fabrication of polymeric microdisks in silicon was also investigated in this work. The Q-factors of these cavities can reach values above 10^6 [45].

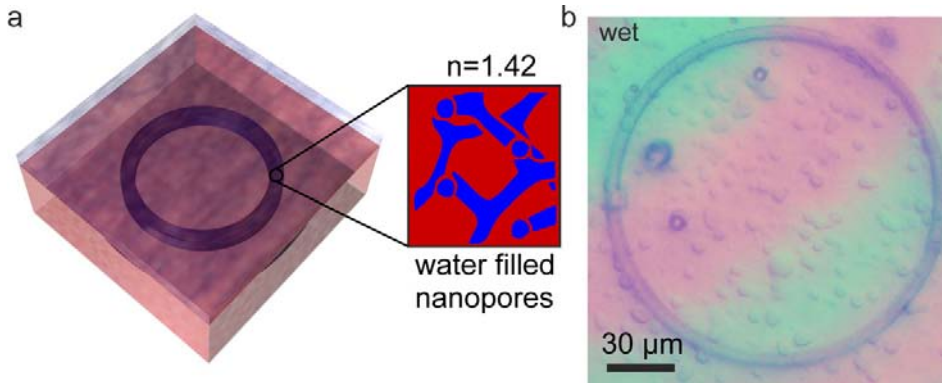


Figure A.2: (a) Schematic and (b) microscope image of a sample with a waterfilm on top, resulting in an infiltrated ring with increased refractive index compared to the surrounding polymer matrix [145].

depicted in Fig. A.2 (b), where the uptake of water in the ring leads to an enhanced contrast.

The dye-doped samples infiltrated with water were pumped from the top at a wavelength of 532 nm with 8 ns pulses (repetition rate 10 Hz). The output emission was collected at the edge of the chip in the plane of the resonator with a multimode optical fiber and analyzed in a spectrometer. Spectra of the laser output for increasing pump fluence are depicted in Fig. A.3 (a). Above a pump fluence of $12 \mu\text{J}/\text{mm}^2$ several sharp lasing modes appeared in the spectrum due to amplification of WGMs by the dye. The output intensity as function of increasing excitation pump fluence is exemplarily shown in Fig. A.3 (b) for the grey marked mode in Fig. A.3 (a). The input-output curve has a kink at a threshold pump fluence of $19 \mu\text{J}/\text{mm}^2$. The observation of lasing clearly demonstrates that light was guided within the liquid-core resonator.

To investigate the sensitivity of a liquid-core WGM laser, tuning of the lasing modes was performed by changing the liquid core's refractive index. The response of the nanoporous liquid-core laser with a radius of $75 \mu\text{m}$ to changing refractive index surroundings was measured by infiltrating the sample with different concentrations of glucose dissolved in water and taking a laser spectrum for every concentration. The shift (in comparison to pure water) of a single laser mode is depicted in Fig. A.4. The slope of the linear fit was measured to be $169 \text{ nm}/\text{RIU}$. This value is around one order of magnitude larger than for solid-state WGM microcavities with comparable radius and wavelength [179] and demonstrates the high potential of liquid-core resonators for sensing applications due to the strongly increased overlap of the modes with the analyte in comparison to evanescent-wave sensors.

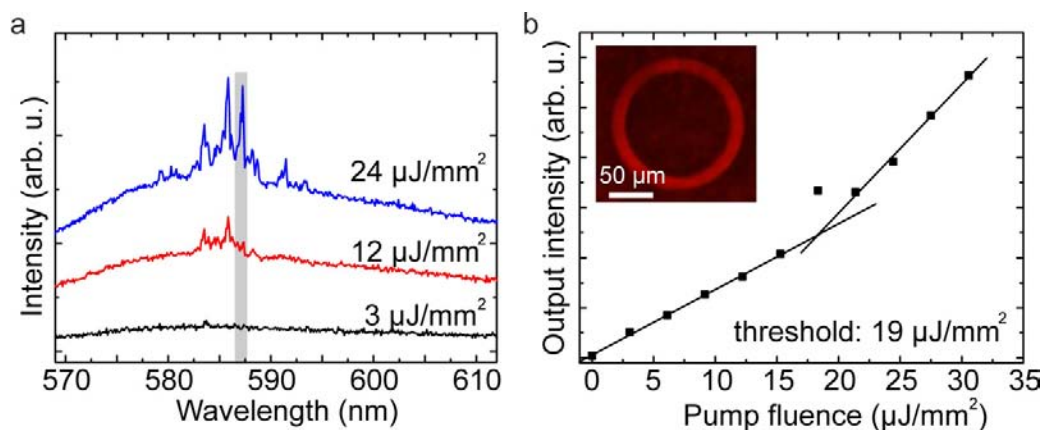


Figure A.3: (a) Output spectrum of an optically pumped dye-doped liquid-core ring resonator laser for different pump fluencies. (b) Input-output curve of the grey marked mode in (a) at 587 nm with a threshold pump fluence of 19 $\mu\text{J}/\text{mm}^2$ [145].

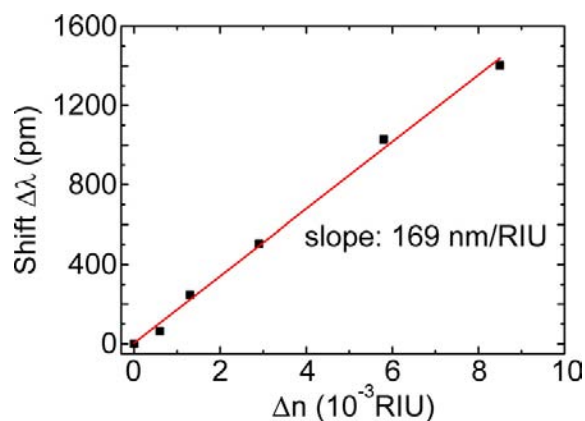


Figure A.4: Shift of the lasing mode of a liquid-core ring resonator for changing refractive index surrounding using different glucose concentrations compared to pure water. The bulk refractive index sensitivity of the liquid-core laser is 169 nm/RIU [145].

Publications

Journal articles

1. **Polymeric photonic molecule super-mode lasers on silicon**, T. Grossmann, T. Wienhold, U. Bog, T. Beck, C. Friedmann, H. Kalt, T. Mappes, *submitted to Light:Science and Application* (18.09.2012).
2. **Biosensing with microlasers created by highly localized multipurpose surface functionalization**, U. Bog, T. Laue, T. Grossmann, T. Beck, T. Wienhold, M. Hirtz, H. Fuchs, H. Kalt, T. Mappes, *submitted to Small* (26.09.2012).
3. **Flexible coupling of high-Q goblet resonators for formation of tunable photonic molecules**, T. Beck, S. Schloer, T. Grossmann, T. Mappes, H. Kalt, *Optics Express* **20**, 22012, 2012.
4. **Direct laser writing for nanoporous liquid core laser sensors**, T. Grossmann, M.B. Christiansen, J. Peterson, H. Kalt, T. Mappes, A. Kristensen, *Optics Express* **20**, 17467, 2012.
5. **Direct laser writing for active and passive high-Q polymer microdisks on silicon**, T. Grossmann, S. Schleede, M. Hauser, T. Beck, M. Thiel, G. von Freymann, T. Mappes, H. Kalt, *Optics Express* **19**, 11451, 2011.
6. **Strongly confined, low-threshold laser modes in organic semiconductor microcones**, T. Grossmann, S. Klinkhammer, M. Hauser, D. Flöss, T. Beck, C. Vannahme, T. Mappes, U. Lemmer, H. Kalt, *Optics Express* **19**, 10009, 2011.
7. **Diode-pumped organic semiconductor microcone laser**, S. Klinkhammer, T. Grossmann, K. Lüll, M. Hauser, C. Vannahme, T. Mappes, H. Kalt, U. Lemmer, *IEEE Photonics Technology Letters* **23**, 489, 2011.

8. **Low-threshold conical microcavity dye lasers**, T. Grossmann, S. Schlee-de, M. Hauser, M.B. Christiansen, C. Vannahme, C. Eschenbaum, S. Klinkhammer, T. Beck, J. Fuchs, G.U. Nienhaus, U. Lemmer, A. Kristensen, T. Mappes, H. Kalt, *Applied Physics Letters* **97**, 063304, 2010.
9. **High-Q conical polymeric microcavities**, T. Grossmann, M. Hauser, T. Beck, C. Gohn-Kreuz, M. Karl, H. Kalt, C. Vannahme, T. Mappes, *Applied Physics Letters* **96**, 013303, 2010.

Patent applications

1. **Mikrooptisches Element, mikrooptisches Array und mikrooptisches Sensorsystem**, T. Mappes, T. Wienhold T. Grossmann, T. Beck, M. Brammer, H. Kalt, *German patent application DE102011107360A1*, 2011.
2. **Mikrooptisches Bauelement und Verfahren zu seiner Herstellung**, T. Grossmann, M. Hauser, C. Vannahme, T. Mappes, T. Beck, H. Kalt, *European patent application EP09010782A2, and US patent application US02011-0044581A1*, 2011.

Contributions to international conferences

1. **On-chip integrated lasers for biophotonic applications**, T. Mappes, T. Wienhold, U. Bog, X. Liu, S. Klinkhammer, U. Lemmer, C. Vannahme, A. Kristensen, T. Grossmann, T. Beck, H. Kalt, *International Symposium on Optomechatronic Technologies, Paris, France, October 2012, invited*.
2. **Coupled polymeric microcavities**, T. Beck, S. Schloer, T. Grossmann, M. Mai, H. Kalt, *11th International Workshop on Nonlinear Optics and Excitation Kinetics in Semiconductors, Stuttgart, September 2012*.
3. **Integrated lasers for polymer lab-on-a-chip systems**, T. Mappes, C. Vannahme, T. Grossmann, T. Beck, T. Wienhold, U. Bog, F. Breithaupt, M. Brammer, X. Liu, S. Klinkhammer, M. Hirtz, T. Laue, M.B. Christiansen, A. Kristensen, U. Lemmer, H. Kalt, *CLEO 2012: Laser Science to Photonic Applications, San Jose, California, USA, May 2012, invited*.
4. **Microoptical device for efficient read-out of active WGM resonators**, T. Wienhold, M. Brammer, T. Grossmann, M. Schneider, H. Kalt, T. Mappes,

SPIE Photonics Europe, Brussels, Belgium, April 2012, Proceedings of SPIE 8428, 842812, 2012.

5. **Low-threshold polymeric microgoblet lasers**, T. Grossmann, M. Hauser, T. Beck, S. Klinkhammer, C. Vannahme, U. Lemmer, T. Mappes, H. Kalt, *492. WE-Heraeus-Seminar on Micro- and macro-cavities in classical and non-classical light, Bad Honnef, October 2011, invited*.
6. **Integrated lasers for biophotonic lab-on-a-chip systems in polymer**, T. Mappes, C. Vannahme, T. Grossmann, S. Klinkhammer, M. Hauser, T. Beck, T. Wienhold, M.B. Christansen, A. Kristensen, H. Kalt, U. Lemmer, *17th Microoptics Conference, Sendai, Japan, October 2011, invited*.
7. **On-Chip lasers for biophotonic lab-on-a-chip applications**, T. Mappes, C. Vannahme, T. Grossmann, S. Klinkhammer, M. Hauser, T. Beck, U. Bog, T. Wienhold, M.B. Christansen, A. Kristensen, U. Lemmer, H. Kalt, *III International Symposium Topical Problems Of Biophotonics 2011, St.-Petersburg - Nizhny Novgorod, Russia, July 2011, invited*.
8. **Numerical analysis and optimization of microresonators**, D. Floess, T. Grossmann, M. Hauser, T. Beck, T. Mappes, H. Kalt, *Matheon-Workshop: 4th Annual Meeting Photonic Devices, Freie Universität Berlin, February 2011, invited*.
9. **Lasing in dye-doped high-Q conical polymeric microcavities**, T. Grossmann, S. Schleede, M. Hauser, M. B. Christiansen, C. Vannahme, C. Eschenbaum, S. Klinkhammer, T. Beck, J. Fuchs, G. U. Nienhaus, U. Lemmer, A. Kristensen, T. Mappes, H. Kalt, *LASE SPIE Photonics West, San Francisco, Kalifornien, USA, January 2011, Proceedings of SPIE 7913*, 79130Y, 2011.
10. **PMMA-microcone resonators for biosensing applications**, T. Beck, M. Hauser, T. Grossmann, S. Schleede, J. Fischer, C. Vannahme, T. Mappes, H. Kalt, *BiOS SPIE Photonics West, San Francisco, Kalifornien, USA, January 2011, Proceedings of SPIE 7888*, 78880A, 2011, *invited*.
11. **Optofluidic lab-on-a-chip systems with integrated lasers**, T. Mappes, C. Vannahme, T. Grossmann, S. Klinkhammer, M. Hauser, T. Wienhold, M. B. Christiansen, A. Kristensen, H. Kalt, U. Lemmer, *1st EOS Conference on Optofluidics (EOSOF 2011), Munich, May 2011, invited*.
12. **High-Q polymeric microcavity for biosensing**, T. Beck, M. Hauser, T. Grossmann, D. Floess, T. Mappes, H. Kalt, *CLEO 2011: Laser Science to Photonic Applications, Baltimore, Maryland, USA, May 2011*.

13. **Low-threshold whispering-gallery dye lasers by planar and 3D lithography on silicon**, T. Grossmann, S. Schleede, M. Hauser, T. Beck, M. Thiel, G. von Freymann, T. Mappes, H. Kalt, *CLEO 2011: Laser Science to Photonic Applications, Baltimore, Maryland, USA, May 2011*.
14. **Low-threshold lasing in organic semiconductor microcones**, T. Grossmann, S. Klinkhammer, M. Hauser, T. Beck, K. Lüll, D. Floess, C. Vannahme, T. Mappes, U. Lemmer, H. Kalt, *CLEO 2011: Laser Science to Photonic Applications, Baltimore, Maryland, USA, May 2011*.
15. **High-Q polymeric whispering-gallery-mode resonators on silicon**, T. Grossmann, M. Hauser, T. Beck, S. Schleede, D. Floess, M. Thiel, S. Klinkhammer, C. Vannahme, G. von Freymann, T. Mappes, U. Lemmer, H. Kalt, *International Conference on Fundamental Optical Processes in Semiconductors, North Carolina, USA, August 2011*.
16. **Fabrication and characterization of high-Q conical polymeric microcavities**, M. Hauser, T. Grossmann, S. Schleede, J. Fischer, T. Beck, C. Vannahme, T. Mappes, H. Kalt, *SPIE Photonics Europe, Brussels, Belgium, April 2010, Proceedings of SPIE 7716, 77161Z, 2010*.
17. **Integrated photonic lab-on-chip systems for biomedical applications**, T. Mappes, C. Vannahme, S. Klinkhammer, U. Bog, M. Schelb, T. Grossmann, M. Hauser, H. Kalt, U. Lemmer, *SPIE Photonics Europe, Brussels, Belgium, 12.-16. April 2010, Proceedings of SPIE 7716, 77160R, 2010, invited*.
18. **High-Q polymeric microcavities towards biosensing applications**, T. Grossmann, M. Hauser, S. Schleede, J. Fischer, T. Beck, H. Kalt, C. Vannahme, T. Mappes, R. Diehl, K. Busch, *OSA Optics Photonics Congress - Advanced Photonics and Renewable Energy, June 2010 Karlsruhe*.
19. **WGM-resonators for optical sensing**, H. Kalt, T. Grossmann, M. Hauser, S. Schleede, J. Fischer, T. Beck, C. Vannahme, T. Mappes, *OSA Optics Photonics Congress - Advanced Photonics and Renewable Energy, June 2010 Karlsruhe, invited*.
20. **High-Q polymeric microcavities**, M. Hauser, T. Grossmann, S. Schleede, J. Fischer, T. Beck, C. Vannahme, T. Mappes, H. Kalt, *CLEO/QELS 2010: Laser Science to Photonic Applications, San Jose, California, USA, May 2010*.
21. **High-Q polymeric microcavities for parallel molecule detection**, T. Grossmann, M. Hauser, T. Beck, J. Fischer, S. Schleede, H. Kalt, C. Vannahme, T. Mappes, *Matheon-Workshop: Annual Meeting Photonic Devices, Freie Universität Berlin, February 2010, invited*.

References

- [1] A. Einstein, “Strahlungs-Emission und -Absorption nach der Quantentheorie,” *Verhandlungen der Deutschen Physikalischen Gesellschaft* **18**, 318–323 (1916).
- [2] A. L. Schawlow and C. H. Townes, “Infrared and optical masers,” *Physical Review Letters* **112**, 1940–1949 (1958).
- [3] T. Maiman, “Stimulated optical radiation in ruby,” *Nature* **187**, 493–494 (1960).
- [4] L. He, S. K. Özdemir, J. Zhu, W. Kim, and L. Yang, “Detecting single viruses and nanoparticles using whispering gallery microlasers,” *Nature Nanotechnology* **6**, 428–432 (2011).
- [5] M. Khajavikhan, A. Simic, M. Katz, and J. Lee, “Thresholdless nanoscale coaxial lasers,” *Nature* **482**, 204–207 (2012).
- [6] C. Garrett, W. Kaiser, and W. Bond, “Stimulated Emission into Optical Whispering Modes of Spheres,” *Physical Review* **124**, 1807–1809 (1961).
- [7] I. Protsenko, P. Domokos, V. Lefevre-Seguin, J. Hare, J. Raimond, and L. Davidovich, “Quantum theory of a thresholdless laser,” *Physical Review A* **59**, 1667–1682 (1999).
- [8] S. Noda, “Seeking the ultimate nanolaser,” *Science* **314**, 260–261 (2006).
- [9] P. Del’Haye, A. Schliesser, O. Arcizet, T. Wilken, R. Holzwarth, and T. J. Kippenberg, “Optical frequency comb generation from a monolithic microresonator,” *Nature* **450**, 1214–1217 (2007).
- [10] T. Carmon and K. J. Vahala, “Visible continuous emission from a silica microphotonic device by third-harmonic generation,” *Nature Physics* **3**, 430–435 (2007).

- [11] T. Lu, L. Yang, T. Carmon, and B. Min, “A Narrow-Linewidth On-Chip Toroid Raman Laser,” *IEEE Journal of Quantum Electronics* **47**, 320–326 (2011).
- [12] W. von Klitzing, R. Long, V. Ilchenko, J. Hare, and V. Lefèvre-Seguin, “Tunable whispering gallery modes for spectroscopy and CQED experiments,” *New Journal of Physics* **3**, 14.1–14.14 (2001).
- [13] T. Aoki, B. Dayan, E. Wilcut, W. P. Bowen, A. S. Parkins, T. J. Kippenberg, K. J. Vahala, and H. J. Kimble, “Observation of strong coupling between one atom and a monolithic microresonator,” *Nature* **443**, 671–674 (2006).
- [14] S. Bose, D. Angelakis, and D. Burgarth, “Transfer of a polaritonic qubit through a coupled cavity array,” *Journal of Modern Optics* **54**, 2307–2314 (2007).
- [15] P. Rabiei, W. H. Steier, C. Zhang, and L. R. Dalton, “Polymer micro-ring filters and modulators,” *Journal of Lightwave Technology* **20**, 1968–1975 (2002).
- [16] V. R. Almeida, C. A. Barrios, R. R. Panepucci, and M. Lipson, “All-optical control of light on a silicon chip,” *Nature* **431**, 1081–1084 (2004).
- [17] A. Armani, R. Kulkarni, S. Fraser, R. Flagan, and K. Vahala, “Label-free, single-molecule detection with optical microcavities,” *Science* **317**, 783–787 (2007).
- [18] F. Vollmer and S. Arnold, “Whispering-gallery-mode biosensing: label-free detection down to single molecules,” *Nature Methods* **5**, 591–596 (2008).
- [19] M. L. Gorodetsky, A. A. Savchenkov, and V. S. Ilchenko, “Ultimate Q of optical microsphere resonators,” *Optics Letters* **21**, 453–455 (1996).
- [20] M. L. Gorodetsky and V. S. Ilchenko, “Optical microsphere resonators: optimal coupling to high-Q whispering-gallery modes,” *Journal of the Optical Society of America B: Optical Physics* **16**, 147–154 (1999).
- [21] D. K. Armani, T. J. Kippenberg, S. M. Spillane, and K. J. Vahala, “Ultra-high-Q toroid microcavity on a chip,” *Nature* **421**, 925–928 (2003).
- [22] T. J. Kippenberg, S. M. Spillane, and K. J. Vahala, “Demonstration of ultra-high-Q small mode volume toroid microcavities on a chip,” *Applied Physics Letters* **85**, 6113–6115 (2004).
- [23] T. Grossmann, M. Hauser, T. Beck, C. Gohn-Kreuz, M. Karl, H. Kalt, C. Van-nahme, and T. Mappes, “High-Q conical polymeric microcavities,” *Applied Physics Letters* **96**, 013303 (2010).

-
- [24] A. L. Martin, D. K. Armani, L. Yang, and K. J. Vahala, “Replica-molded high-Q polymer microresonators.” *Optics Letters* **29**, 533–535 (2004).
- [25] T. Grossmann, S. Schleede, M. Hauser, M. B. Christiansen, C. Vannahme, C. Eschenbaum, S. Klinkhammer, T. Beck, J. Fuchs, G. U. Nienhaus, U. Lemmer, A. Kristensen, T. Mappes, and H. Kalt, “Low-threshold conical microcavity dye lasers,” *Applied Physics Letters* **97**, 063304 (2010).
- [26] C. Ahn, J.-W. Choi, G. Beaucage, J. Nevin, J.-B. Lee, A. Puntambekar, and R. Lee, “Disposable smart lab on a chip for point-of-care clinical diagnostics,” *Proceedings of the IEEE* **92**, 154–173 (2004).
- [27] X. Fan, I. M. White, S. I. Shopova, H. Zhu, J. D. Suter, and Y. Sun, “Sensitive optical biosensors for unlabeled targets: a review.” *Analytica chimica acta* **620**, 8–26 (2008).
- [28] J. Yang and L. Guo, “Optical sensors based on active microcavities,” *IEEE Journal of Selected Topics in Quantum Electronics* **12**, 143–147 (2006).
- [29] L. He, S. Özdemir, J. Zhu, and L. Yang, “Ultrasensitive detection of mode splitting in active optical microcavities,” *Physical Review A* **82**, 053810 (2010).
- [30] S. V. Boriskina, “Spectrally engineered photonic molecules as optical sensors with enhanced sensitivity: a proposal and numerical analysis,” *Journal of the Optical Society of America B* **23**, 1565–1573 (2006).
- [31] S. V. Boriskina, “Photonic Molecules and Spectral Engineering,” in “Photonic Microresonator Research and Applications,” , vol. 156 of *Springer Series in Optical Sciences*, I. Chremmos, O. Schwelb, and N. Uzunoglu, eds. (Springer US, Boston, MA, 2010), chap. 16, pp. 393–421.
- [32] K. Hiremath, J. Niegemann, and K. Busch, “Analysis of light propagation in slotted resonator based systems via coupled-mode theory,” *Optics Express* **19**, 8641–8655 (2011).
- [33] J. S. T. Gehler, *Physikalisches Wörterbuch*, vol. 8 (Schwickert Verlag, Leipzig, 1836).
- [34] Lord Rayleigh, “The Problem of the Whispering Gallery,” *Philosophical Magazine* **20**, 1001–1004 (1910).
- [35] Lord Rayleigh, “Further applications of Bessel’s functions of high order to the Whispering Gallery and allied problems,” *Philosophical Magazine* **27**, 100–109 (1914).
-

- [36] R. D. Richtmyer, “Dielectric Resonators,” *Journal of Applied Physics* **10**, 391–398 (1939).
- [37] Y. Panitchob, G. Murugan, M. Zervas, P. Horak, S. Berneschi, S. Pelli, G. Nunzi Conti, and J. Wilkinson, “Whispering gallery mode spectra of channel waveguide coupled microspheres,” *Optics Express* **16**, 11066–11076 (2008).
- [38] A. Ashkin and J. M. Dziedzic, “Observation of optical resonances of dielectric spheres by light scattering,” *Applied Optics* **20**, 1803–1814 (1981).
- [39] M. Borselli, T. J. Johnson, and O. Painter, “Beyond the Rayleigh scattering limit in high-Q silicon microdisks: theory and experiment,” *Optics Express* **13**, 1515–1530 (2005).
- [40] M. Soltani, S. Yegnanarayanan, and A. Adibi, “Ultra-high Q planar silicon microdisk resonators for chip-scale silicon photonics,” *Optics Express* **15**, 4694–4704 (2007).
- [41] H. Lee, T. Chen, J. Li, K. Y. Yang, S. Jeon, O. Painter, and K. J. Vahala, “Chemically etched ultrahigh-Q wedge-resonator on a silicon chip,” *Nature Photonics* **6**, 369–373 (2012).
- [42] S. Spillane, T. Kippenberg, and K. Vahala, “Ultrahigh-Q toroidal microresonators for cavity quantum electrodynamics,” *Physical Review A* **71**, 13817 (2005).
- [43] A. M. Armani, A. Srinivasan, and K. J. Vahala, “Soft Lithographic Fabrication of High Q Polymer Microcavity Arrays,” *Nano Letters* **7**, 1823–1826 (2007).
- [44] M. Hentschel, “Billiards für Licht,” *Physik Journal* **10**, 39–43 (2011).
- [45] T. Grossmann, S. Schleede, M. Hauser, T. Beck, M. Thiel, G. von Freymann, T. Mappes, and H. Kalt, “Direct laser writing for active and passive high-Q polymer microdisks on silicon.” *Optics Express* **19**, 11451–11456 (2011).
- [46] X. Fan and I. M. White, “Optofluidic microsystems for chemical and biological analysis,” *Nature Photonics* **5**, 591–597 (2011).
- [47] M. S. Luchansky and R. C. Bailey, “High-Q Optical Sensors for Chemical and Biological Analysis.” *Analytical Chemistry* **84**, 793–821 (2011).
- [48] I. H. Agha, J. E. Sharping, M. A. Foster, and A. L. Gaeta, “Optimal sizes of silica microspheres for linear and nonlinear optical interactions,” *Applied Physics B* **83**, 303–309 (2006).

-
- [49] B. E. A. Saleh and M. C. Teich, *Fundamentals of Photonics* (John Wiley & Sons, 2007), 2nd ed.
- [50] J. D. Jackson, *Classical Electrodynamics* (John Wiley & Sons, 1999), 3rd ed.
- [51] B. Min, “Ultrahigh-Q microtoroid on-chip resonators for low threshold micro-lasers,” Dissertation, California Institute of Technology, Pasadena, California (2006).
- [52] Y. Takezawa, N. Taketani, S. Tanno, and S. Ohara, “Empirical estimation method of intrinsic loss spectra in transparent amorphous polymers for plastic optical fibers,” *Journal of Applied Polymer Science* **46**, 1835–1841 (1992).
- [53] T. Knoche, L. Muller, R. Klein, and A. Neyer, “Low loss polymer waveguides at 1300 and 1550 nm using halogenated acrylates,” *Electronic Letters* **32**, 1284–1285 (1996).
- [54] A. Dupuis, N. Guo, B. Gauvreau, A. Hassani, E. Pone, F. Boismenu, and M. Skorobogatiy, “Guiding in the visible with ”colorful” solid-core Bragg fibers,” *Optics Letters* **32**, 2882–2884 (2007).
- [55] M. L. Gorodetsky, A. D. Pryamikov, and V. S. Ilchenko, “Rayleigh scattering in high-Q microspheres,” *Journal of the Optical Society of America B* **17**, 1051–1057 (2000).
- [56] J. E. Mark, ed., *Polymer Data Handbook* (Oxford University Press, Inc., 1999).
- [57] Y. Okada and Y. Tokumaru, “Precise determination of lattice parameter and thermal expansion coefficient of silicon between 300 and 1500 K,” *Journal of Applied Physics* **56**, 314–320 (1984).
- [58] D. Daly, R. F. Stevens, M. C. Hutley, and N. Davies, “The manufacture of microlenses by melting photoresist,” *Meas. Sci. Technol.* **1**, 759–766 (1990).
- [59] S. Spillane, T. Kippenberg, O. Painter, and K. Vahala, “Ideality in a Fiber-Taper-Coupled Microresonator System for Application to Cavity Quantum Electrodynamics,” *Physical Review Letters* **91**, 2–5 (2003).
- [60] T. J. Kippenberg, A. D. K. Spillane S. M., B. Min, L. Yang, and K. J. Vahala, “Fabrication, coupling and nonlinear optics of ultra-high-Q micro-sphere and chip-based toroid microcavities,” in “Optical Microcavities,” , vol. 5 of *Advanced Series in Applied Physics*, K. J. Vahala, ed. (World Scientific, 2004).
- [61] H. A. Haus, *Waves and Fields in Optoelectronics*. (Prentice-Hall, 1984).
-

- [62] A. Yariv, “Universal relations for coupling of optical power between microresonators and dielectric waveguides,” *Electronics Letters* **36**, 321–322 (2000).
- [63] T. J. Kippenberg, “Nonlinear Optics in Ultra-high-Q Whispering-Gallery Optical Microcavities,” Dissertation, California Institute of Technology, Pasadena, California (2004).
- [64] G. Brambilla, F. Xu, and X. Feng, “Fabrication of optical fibre nanowires and their optical and mechanical characterisation,” *Electronics Letters* **42**, 9–10 (2006).
- [65] T. Grossmann, S. Klinkhammer, M. Hauser, D. Floess, T. Beck, C. Vannahme, T. Mappes, U. Lemmer, and H. Kalt, “Strongly confined, low-threshold laser modes in organic semiconductor microgloblets.” *Optics Express* **19**, 10009–10016 (2011).
- [66] P. Henzi, K. Bade, D. G. Rabus, and J. Mohr, “Modification of polymethylmethacrylate by deep ultraviolet radiation and bromination for photonic applications,” *Journal of Vacuum Science and Technology B* **24**, 1755 (2006).
- [67] J. Pomplun, S. Burger, L. Zschiedrich, and F. Schmidt, “Adaptive finite element method for simulation of optical nano structures,” *physica status solidi (b)* **244**, 3419–3434 (2007).
- [68] C. Gohn-Kreuz, “Numerische Analyse der optischen Eigenschaften von Mikroresonatoren und experimenteller Aufbau zur Anregung von Resonanzmoden,” Diplom thesis, Universität Karlsruhe (TH), Karlsruhe (2008).
- [69] D. Floess, “Numerische Analyse optischer Flüstergalerieresonatoren zur Biodektektion,” Diplom thesis, Karlsruhe Institute of Technology (KIT), Karlsruhe (2011).
- [70] F. P. Schäfer, ed., *Dye lasers* (Springer, 1990).
- [71] T. Hänsch, “Repetitively pulsed tunable dye laser for high resolution spectroscopy,” *Applied Optics* **11**, 895–898 (1972).
- [72] O. Peterson, S. Tuccio, and B. Snavely, “CW operation of an organic dye solution laser,” *Applied Physics Letters* **17**, 245–247 (1970).
- [73] J. Valdmanis, R. Fork, and J. Gordon, “Optical pulses as short as 27 femtoseconds directly from a laser balancing self-phase modulation, group-velocity dispersion, saturable absorption, and saturable gain,” *Optics Letters* **10**, 131–133 (1985).

-
- [74] E. Yariv, S. Schultheiss, T. Saraidarov, and R. Reisfeld, “Efficiency and photostability of dye-doped solid-state lasers in different hosts,” *Optical Materials* **16**, 29–38 (2001).
- [75] A. Yariv and P. Yeh, *Photonics*. (Oxford University Press, 2007).
- [76] H. P. Latscha, U. Kazmaier, and H. A. Klein, *Organische Chemie: Chemie-Basiswissen II* (Springer Berlin / Heidelberg, 2008).
- [77] O. Svelto, *Principles of Lasers* (Plenum Press, 2007).
- [78] M. M. Mazumder, G. Chen, R. K. Chang, and J. B. Gillespie, “Wavelength shifts of dye lasing in microdroplets: effect of absorption change.” *Optics Letters* **20**, 878–880 (1995).
- [79] J. T. Verdeyen, *Laser Electrodynamics* (Prentice-Hall, 1995), 3rd ed.
- [80] H. Moon, Y. Chough, J. Kim, K. An, J. Yi, and J. Lee, “Cavity-Q-driven spectral shift in a cylindrical whispering-gallery-mode microcavity laser,” *Applied Physics Letters* **76**, 3679–3681 (2000).
- [81] O. Peterson, J. Webb, W. McColgin, and J. Eberly, “Organic dye laser threshold,” *Journal of Applied Physics* **42**, 1917–1928 (1971).
- [82] C. Grivas and M. Pollnau, “Organic solid-state integrated amplifiers and lasers,” *Laser & Photonics Reviews* **6**, 419–462 (2012).
- [83] M. B. Christiansen, T. Buß, C. L. C. Smith, S. R. Petersen, M. M. Jørgensen, and A. Kristensen, “Single mode dye-doped polymer photonic crystal lasers,” *Journal of Micromechanics and Microengineering* **20**, 115025 (2010).
- [84] J.-F. Ku, Q.-D. Chen, R. Zhang, and H.-B. Sun, “Whispering-gallery-mode microdisk lasers produced by femtosecond laser direct writing.” *Optics Letters* **36**, 2871–2873 (2011).
- [85] C. Vannahme, M. Christiansen, T. Mappes, and A. Kristensen, “Optofluidic dye laser in a foil,” *Optics Express* **18**, 9280–9285 (2010).
- [86] T. Wienhold, F. Breithaupt, C. Vannahme, M. Brøkner Christiansen, W. Dörfler, A. Kristensen, and T. Mappes, “Diffusion driven optofluidic dye lasers encapsulated into polymer chips.” *Lab on a Chip* **12**, 3734–3739 (2012).
- [87] A. Kurian, N. A. George, B. Paul, V. P. N. Nampoore, and C. P. G. Vallabhan, “Studies on fluorescence efficiency and photodegradation of rhodamine 6g doped PMMA using a dual beam thermal Lens technique,” *Laser Chemistry* **20**, 99–110 (2002).
-

- [88] G. Kranzelbinder and G. Leising, “Organic solid-state lasers,” *Reports on Progress in Physics* **63**, 729–762 (2000).
- [89] M. Fischer and J. Georges, “Fluorescence quantum yield of rhodamine 6G in ethanol as a function of concentration using thermal lens spectrometry,” *Chemical Physics Letters* **260**, 115–118 (1996).
- [90] F. López Arbeloa, P. Ruiz Ojeda, and I. López Arbeloa, “The fluorescence quenching mechanisms 6g in concentrated ethanolic solution,” *Journal of Photochemistry and Photobiology A* **45**, 313–323 (1988).
- [91] W. Holzer, H. Gratz, T. Schmitt, A. Penzkofer, A. Costela, R. Sastre, and F. J. Duarte, “Photo-physical characterization of rhodamine 6G in a 2-hydroxyethyl-methacrylate methyl-methacrylate copolymer,” *Chemical Physics* **256**, 125–136 (2000).
- [92] T. Grossmann, S. Schleede, M. Hauser, M. B. k. Christiansen, C. Vannahme, C. Eschenbaum, S. Klinkhammer, T. Beck, J. Fuchs, G. U. Nienhaus, U. Lemmer, A. Kristensen, T. Mappes, and H. Kalt, “Lasing in dye-doped high-Q conical polymeric microcavities,” *Proceedings of SPIE* **7913**, 79130Y (2011).
- [93] D. Nilsson, T. Nielsen, and a. Kristensen, “Solid state microcavity dye lasers fabricated by nanoimprint lithography,” *Review of Scientific Instruments* **75**, 4481 (2004).
- [94] B. Min, S. Kim, K. Okamoto, L. Yang, A. Scherer, H. Atwater, and K. Vahala, “Ultralow threshold on-chip microcavity nanocrystal quantum dot lasers,” *Applied Physics Letters* **89**, 191124 (2006).
- [95] T. Wienhold, M. Brammer, T. Grossmann, M. Schneider, H. Kalt, and T. Mappes, “Microoptical device for efficient read-out of active WGM resonators,” *Proceedings of SPIE* **8428**, 842812 (2012).
- [96] S. Klinkhammer, T. Grossmann, K. Lüll, M. Hauser, C. Vannahme, T. Mappes, H. Kalt, and U. Lemmer, “Diode-pumped organic semiconductor microcone laser,” *IEEE Photonics Technology Letters* **23**, 489–491 (2011).
- [97] A. Costela, I. Garcia-Moreno, J. M. Figuera, F. Amat-Guerri, R. Mallavia, M. D. Santa-Maria, and R. Sastre, “Solidstate dye lasers based on modified rhodamine 6G dyes copolymerized with methacrylic monomers,” *Journal of Applied Physics* **80**, 3167–3173 (1996).
- [98] L. Cerdán, a. Costela, I. García-Moreno, O. García, and R. Sastre, “Waveguides and quasi-waveguides based on pyrromethene 597-doped poly(methyl methacrylate),” *Applied Physics B* **97**, 73–83 (2009).

-
- [99] J. Bañuelos Prieto, F. López Arbeloa, V. Martínez Martínez, T. Arbeloa López, and I. López Arbeloa, “Photophysical Properties of the Pyrromethene 597 Dye: Solvent Effect,” *Journal of Physical Chemistry A* **108**, 5503–5508 (2004).
- [100] M. Ahmad, T. King, D. Ko, B. H. Cha, and J. Lee, “Photostability of lasers based on pyrromethene 567 in liquid and solid-state host media,” *Optics Communications* **203**, 327–334 (2002).
- [101] R. M. Waxler, D. Horowitz, and A. Feldman, “Optical and physical parameters of Plexiglas 55 and Lexan,” *Applied Optics* **18**, 101–104 (1979).
- [102] H. S. Choi and A. M. Armani, “Thermal nonlinear effects in hybrid optical microresonators,” *Applied Physics Letters* **97**, 223306 (2010).
- [103] T. Carmon, L. Yang, and K. Vahala, “Dynamical thermal behavior and thermal self-stability of microcavities,” *Optics Express* **12**, 4742–4750 (2004).
- [104] M. Hauser, “Mikroresonatoren aus Glas und Polymeren als optische Flüstergalerien,” Dissertation, Karlsruhe Institute of Technology (KIT) (2011).
- [105] N. Jokerst, M. Royal, S. Palit, L. Luan, S. Dhar, and T. Tyler, “Chip scale integrated microresonator sensing systems.” *Journal of Biophotonics* **2**, 212–226 (2009).
- [106] H. K. Hunt and A. M. Armani, “Label-free biological and chemical sensors.” *Nanoscale* **2**, 1544–1559 (2010).
- [107] W. E. Moerner, “New directions in single-molecule imaging and analysis.” *Proceedings of the National Academy of Sciences* **104**, 12596–602 (2007).
- [108] K. Matsubara, S. Kawata, and S. Minami, “Optical chemical sensor based on surface plasmon measurement,” *Applied Optics* **27**, 1160–1163 (1988).
- [109] D. Monzón-Hernández and J. Villatoro, “High-resolution refractive index sensing by means of a multiple-peak surface plasmon resonance optical fiber sensor,” *Sensors and Actuators B: Chemical* **115**, 227 (2006).
- [110] R. G. Heideman and P. V. Lambeck, “Remote opto-chemical sensing with extreme sensitivity: design, fabrication and performance of a pigtailed integrated optical phase-modulated Mach-Zehnder interferometer system,” *Sensors and Actuators B: Chemical* **61**, 100 (1999).
-

- [111] A. Ymeti, J. S. Kanger, J. Greve, P. V. Lambeck, R. Wijn, and R. G. Heide-
man, “Realization of a multichannel integrated Young interferometer chemical
sensor,” *Applied Optics* **42**, 5649–5660 (2003).
- [112] A. Leung, P. M. Shankar, and R. Mutharasan, “A review of fiber-optic biosen-
sors,” *Sensors and Actuators B: Chemical* **125**, 688–703 (2007).
- [113] T. Sünner, T. Stichel, S.-H. Kwon, T. W. Schlereth, S. Höfling, M. Kamp,
and A. Forchel, “Photonic crystal cavity based gas sensor,” *Applied Physics
Letters* **92**, 261112 (2008).
- [114] S. Mandal and D. Erickson, “Nanoscale optofluidic sensor arrays,” *Optics Ex-
press* **16**, 1623–1631 (2008).
- [115] S. Mandal, J. M. Goddard, and D. Erickson, “A multiplexed optofluidic
biomolecular sensor for low mass detection,” *Lab on a Chip* **9**, 2924–2932
(2009).
- [116] F. Vollmer, D. Braun, A. Libchaber, M. Khoshshima, I. Teraoka, and S. Arnold,
“Protein detection by optical shift of a resonant microcavity,” *Applied Physics
Letters* **80**, 4057–4059 (2002).
- [117] H.-C. Ren, F. Vollmer, S. Arnold, and A. Libchaber, “High-Q microsphere
biosensor - analysis for adsorption of rodlike bacteria,” *Optics Express* **15**,
17410–17423 (2007).
- [118] H. Zhu, I. M. White, J. D. Suter, P. S. Dale, and X. Fan, “Analysis of
biomolecule detection with optofluidic ring resonator sensors.” *Optics Express*
15, 9139–46 (2007).
- [119] M. Iqbal, M. A. Gleeson, B. Spaugh, F. Tybor, W. G. Gunn, M. Hochberg,
T. Baehr-Jones, R. C. Bailey, and L. C. Gunn, “Label-Free Biosensor Ar-
rays Based on Silicon Ring Resonators and High-Speed Optical Scanning In-
strumentation,” *IEEE Journal of Selected Topics in Quantum Electronics* **16**,
654–661 (2010).
- [120] J. A. Qavi, T. M. Mysz, and R. C. Bailey, “Isothermal Discrimination of Single-
Nucleotide Polymorphisms via Real-Time Kinetic Desorption and Label-Free
Detection of DNA Using Silicon Photonic Microring Resonator Arrays,” *Ana-
lytical Chemistry* **83**, 6827–6833 (2011).
- [121] F. Vollmer, S. Arnold, and D. Keng, “Single virus detection from the reactive
shift of a whispering-gallery mode,” *Proceedings of the National Academy of
Sciences* **105**, 20701–20704 (2008).

-
- [122] I. White and X. Fan, “On the performance quantification of resonant refractive index sensors,” *Optics Express* **16**, 1020–1028 (2008).
- [123] S. Arnold, S. I. Shopova, and S. Holler, “Whispering gallery mode bio-sensor for label-free detection of single molecules - thermo-optic vs. reactive mechanism,” *Optics Express* **18**, 281–287 (2010).
- [124] L. Yang, T. Lu, T. Carmon, B. Min, and K. Vahala, “A 4-Hz fundamental linewidth on-chip microlaser,” in “CLEO,” (Optical Society of America, 2007).
- [125] L. E. Richter, H. I. Mandelberg, M. S. Kruger, and P. A. McGrath, “Linewidth determination from self-heterodyne measurements with subcoherence delay times,” *IEEE Journal of Quantum Electronics* **22**, 2070–2074 (1986).
- [126] H. Ludvigsen, M. Tossavainen, and M. Kaivola, “Laser linewidth measurements using self-homodyne detection with short delay,” *Optics Communications* **155**, 180–186 (1998).
- [127] A. Mazzei, S. Götzinger, L. de S. Menezes, G. Zumofen, O. Benson, and V. Sandoghdar, “Controlled Coupling of Counterpropagating Whispering-Gallery Modes by a Single Rayleigh Scatterer: A Classical Problem in a Quantum Optical Light,” *Physical Review Letters* **99**, 173603 (2007).
- [128] T. J. Kippenberg, “Microresonators: Particle sizing by mode splitting,” *Nature Photonics* **4**, 9–10 (2010).
- [129] J. Zhu, S. K. Özdemir, L. Li, Y.-F. Xiao, L. He, D.-R. Chen, and L. Yang, “On-chip single nanoparticle detection and sizing by mode splitting in an ultrahigh-Q microresonator,” *Nature Photonics* **4**, 46 (2010).
- [130] G. M. Hale and M. R. Querry, “Optical constants of water in the 200 nm to 200\textmum wavelength region,” *Applied Optics* **12**, 555–563 (1973).
- [131] A. Vesel, K. Elersic, and M. Mozetic, “Immobilization of protein streptavidin to the surface of PMMA polymer,” *Vacuum* **86**, 773–775 (2012).
- [132] S. Arnold, M. Khoshsima, I. Teraoka, S. Holler, and F. Vollmer, “Shift of whispering-gallery modes in microspheres by protein adsorption,” *Optics Letters* **28**, 272–274 (2003).
- [133] H. K. Hunt, C. Soteropulos, and A. M. Armani, “Bioconjugation Strategies for Microtoroidal Optical Resonators,” *Sensors* **10**, 9317–9336 (2010).
-

- [134] S. Rozhok, R. Piner, and C. A. Mirkin, “Dip-Pen Nanolithography: What Controls Ink Transport?” *The Journal of Physical Chemistry B* **107**, 751–757 (2003).
- [135] D. S. Ginger, H. Zhang, and C. a. Mirkin, “The evolution of dip-pen nanolithography.” *Angewandte Chemie* **43**, 30–45 (2004).
- [136] K. Salaita, Y. Wang, and C. Mirkin, “Applications of dip-pen nanolithography,” *Nature Nanotechnology* **2**, 145–155 (2007).
- [137] S. Lenhert, P. Sun, Y. Wang, H. Fuchs, and C. A. Mirkin, “Massively Parallel Dip-Pen Nanolithography of Heterogeneous Supported Phospholipid Multilayer Patterns,” *Small* **3**, 71–75 (2007).
- [138] U. Bog, T. Laue, T. Grossmann, T. Beck, T. Wienhold, M. Hirtz, H. Fuchs, H. Kalt, and T. Mappes, “Biosensing with microlasers created by highly localized multipurpose surface functionalization,” submitted (2012).
- [139] S. Lenhert, F. Brinkmann, T. Laue, S. Walheim, C. Vannahme, S. Klinkhammer, M. Xu, S. Sekula, T. Mappes, T. Schimmel, and H. Fuchs, “Lipid multilayer gratings,” *Nature Nanotechnology* **5**, 275–279 (2010).
- [140] I. D. W. Samuel and G. A. Turnbull, “Organic semiconductor lasers.” *Chemical Reviews* **107**, 1272–95 (2007).
- [141] T. Förster, “Zwischenmolekulare energiewanderung und fluoreszenz,” *Annalen der Physik* **437**, 55–75 (1948).
- [142] V. G. Kozlov, V. Bulovic, P. E. Burrows, M. Baldo, V. B. Khalfin, G. Parthasarathy, S. R. Forrest, Y. You, and M. E. Thompson, “Study of lasing action based on Foerster energy transfer in optically pumped organic semiconductor thin films,” *Journal of Applied Physics* **84**, 4096–4108 (1998).
- [143] M. Oxborrow, “Traceable 2-D Finite-Element Simulation of the Whispering-Gallery Modes of Axisymmetric Electromagnetic Resonators,” *IEEE Transactions on Microwave Theory and Techniques* **55**, 1209–1218 (2007).
- [144] T. Beierlein, B. Ruhstaller, D. Gundlach, H. Riel, S. Karg, C. Rost, and W. Rieß, “Investigation of internal processes in organic light-emitting devices using thin sensing layers,” *Synthetic Metals* **138**, 213–221 (2003).
- [145] T. Grossmann, M. Christiansen, J. Peterson, H. Kalt, T. Mappes, and A. Kristensen, “Direct laser writing for nanoporous liquid core laser sensors,” *Optics Express* **20**, 17467–17473 (2012).

-
- [146] E. Lidorikis, M. Sigalas, E. Economou, and C. Soukoulis, “Tight-Binding Parametrization for Photonic Band Gap Materials,” *Physical Review Letters* **81**, 1405–1408 (1998).
- [147] Y. P. Rakovich, J. F. Donegan, M. Gerlach, A. L. Bradley, T. M. Connolly, J. J. Boland, N. Gaponik, and A. Rogach, “Fine structure of coupled optical modes in photonic molecules,” *Physical Review A* **70**, 51801 (2004).
- [148] M. Bayer, T. Gutbrod, J. Reithmaier, A. Forchel, T. Reinecke, P. Knipp, A. Dremin, and V. Kulakovskii, “Optical Modes in Photonic Molecules,” *Physical Review Letters* **81**, 2582–2585 (1998).
- [149] E. Ozbay, M. Bayindir, I. Bulu, and E. Cubukcu, “Investigation of localized coupled-cavity modes in two-dimensional photonic bandgap structures,” *IEEE Journal of Quantum Electronics* **38**, 837–843 (2002).
- [150] M. Barnes, S. Mahurin, A. Mehta, B. Sumpter, and D. Noid, “Three-dimensional photonic molecules from sequentially attached polymer-blend microparticles,” *Physical Review Letters* **88**, 15508 (2001).
- [151] Y. Hara, T. Mukaiyama, K. Takeda, and M. Kuwata-Gonokami, “Photonic molecule lasing,” *Optics Letters* **28**, 2437–2439 (2003).
- [152] V. Astratov, J. Franchak, and S. Ashili, “Optical coupling and transport phenomena in chains of spherical dielectric microresonators with size disorder,” *Applied Physics Letters* **85**, 5508–5510 (2004).
- [153] A. Nakagawa, S. Ishii, and T. Baba, “Photonic molecule laser composed of GaInAsP microdisks,” *Applied Physics Letters* **86**, 041112 (2005).
- [154] S. Boriskina, T. Benson, P. Sewel, and A. I. Nosich, “Directional emission, increased free spectral range, and mode Q-factors in 2-D wavelength-scale optical microcavity structures,” *IEEE Journal of Selected Topics in Quantum Electronics* **12**, 1175–1182 (2006).
- [155] W. Lee, H. Li, J. D. Suter, K. Reddy, Y. Sun, and X. Fan, “Tunable single mode lasing from an on-chip optofluidic ring resonator laser,” *Applied Physics Letters* **98**, 061103 (2011).
- [156] L. Shang, L. Liu, and L. Xu, “Single-frequency coupled asymmetric microcavity laser,” *Optics Letters* **33**, 1150–1152 (2008).
- [157] M. Povinelli, S. Johnson, M. Lonà, M. Ibanescu, E. Smythe, F. Capasso, and J. Joannopoulos, “High-Q enhancement of attractive and repulsive optical
-

- forces between coupled whispering-gallery-mode resonators,” *Optics Express* **13**, 8286–8295 (2005).
- [158] B. Little, S. Chu, H. Haus, J. Foresi, and J.-P. Laine, “Microring resonator channel dropping filters,” *Journal of Lightwave Technology* **15**, 998–1005 (1997).
- [159] T. Grossmann, T. Wienhold, U. Bog, T. Beck, C. Friedmann, H. Kalt, and T. Mappes, “Polymeric photonic molecule super-mode lasers on silicon,” submitted (2012).
- [160] I. S. Grudinin, H. Lee, O. Painter, and K. J. Vahala, “Phonon Laser Action in a Tunable Two-Level System,” *Physical Review Letters* **104**, 83901 (2010).
- [161] B. Peng, a. K. Özdemir, J. Zhu, and L. Yang, “Photonic molecules formed by coupled hybrid resonators,” *Optics Letters* **37**, 3435–3437 (2012).
- [162] H. Lin, J.-H. Chen, S.-S. Chao, M.-C. Lo, S.-D. Lin, and W.-H. Chang, “Strong coupling of different cavity modes in photonic molecules formed by two adjacent microdisk microcavities.” *Optics Express* **18**, 23948–23956 (2010).
- [163] T. Beck, S. Schloer, T. Grossmann, T. Mappes, and H. Kalt, “Flexible coupling of high-Q goblet resonators for formation of tunable photonic molecules.” *Optics Express* **20**, 22012–22017 (2012).
- [164] H.-Y. Chen and J. Lahann, “Designable biointerfaces using vapor-based reactive polymers.” *Langmuir* **27**, 34–48 (2011).
- [165] O. I. Szentesi and E. A. Noga, “Parylene C Films for Optical Waveguides,” *Applied Optics* **13**, 2458–2459 (1974).
- [166] C. Schmidt, M. Liebsch, A. Klein, N. Janunts, A. Chipouline, T. Käsebier, C. Etrich, F. Lederer, E. Kley, A. Tünnermann, and T. Pertsch, “Near-field mapping of optical eigenstates in coupled disk microresonators,” *Physical Review A* **85**, 033827 (2012).
- [167] A. Savchenkov, V. Ilchenko, A. Matsko, and L. Maleki, “High-order tunable filters based on a chain of coupled crystalline whispering gallery-mode resonators,” *IEEE Photonics Technology Letters* **17**, 136–138 (2005).
- [168] C. Chaichuay, P. Yupapin, and P. Saeung, “The serially coupled multiple ring resonator filters and Vernier effect,” *Optica Applicata* **39**, 175–193 (2009).

-
- [169] R. Boeck, N. Jaeger, N. Rouger, and L. Chrostowski, “Series-coupled silicon racetrack resonators and the Vernier effect: theory and measurement,” *Optics Express* **18**, 25151–25157 (2010).
- [170] S. V. Boriskina and L. Dal Negro, “Self-referenced photonic molecule bio(chemical)sensor.” *Optics Letters* **35**, 2496–2498 (2010).
- [171] M. J. Hartmann, F. G. S. L. Brandão, and M. B. Plenio, “Effective Spin Systems in Coupled Microcavities,” *Physical Review Letters* **99**, 160501 (2007).
- [172] H.-Y. Chen, A. A. McClelland, Z. Chen, and J. Lahann, “Solventless adhesive bonding using reactive polymer coatings.” *Analytical Chemistry* **80**, 4119–4124 (2008).
- [173] H. Schmidt and A. R. Hawkins, “Optofluidic waveguides: I. Concepts and implementations,” *Microfluidics and Nanofluidics* **4**, 3–16 (2007).
- [174] N. Gopalakrishnan, K. S. Sagar, M. B. k. Christiansen, M. E. Vigild, S. Ndoni, and A. Kristensen, “UV patterned nanoporous solid-liquid core waveguides.” *Optics Express* **18**, 12903–12908 (2010).
- [175] K. Sagar, N. Gopalakrishnan, M. B. k. Christiansen, A. Kristensen, and S. Ndoni, “Photolithographic fabrication of solid-liquid core waveguides by thiol-ene chemistry,” *Journal of Micromechanics and Microengineering* **21**, 095001 (2011).
- [176] L. Schulte, A. Grydgaard, M. R. Jakobsen, P. P. Szewczykowski, F. Guo, M. E. Vigild, R. H. Berg, and S. Ndoni, “Nanoporous materials from stable and metastable structures of 1,2-PB-b-PDMS block copolymers,” *Polymer* **52**, 422–429 (2011).
- [177] G. von Freymann, A. Ledermann, M. Thiel, I. Staude, S. Essig, K. Busch, and M. Wegener, “Three-Dimensional Nanostructures for Photonics,” *Advanced Functional Materials* **20**, 1038–1052 (2010).
- [178] N. Gopalakrishnan, M. B. k. Christiansen, and A. Kristensen, “Nanofiltering via integrated liquid core waveguides.” *Optics Letters* **36**, 3350–3352 (2011).
- [179] H. Li, L. Shang, X. Tu, L. Liu, and L. Xu, “Coupling variation induced ultra-sensitive label-free biosensing by using single mode coupled microcavity laser.” *Journal of the American Chemical Society* **131**, 16612–16613 (2009).
-

Acknowledgements

The last chapter of this work is dedicated to all the people that supported me during my work, which was performed at the Institut für Angewandte Physik (APH) and the Institut für Mikrostrukturtechnik (IMT) at the Karlsruher Institut für Technologie (KIT). The work on nanoporous liquid-core lasers was carried out at the Department of Micro- and Nanotechnology (DTU Nanotech) at the Danish Technical University (DTU). Without the help of many colleagues the results presented in this thesis would not have been accomplished. Therefore, I want to express great gratitude to

- Prof. Dr. Heinz Kalt for the chance to work on this intriguing subject, the interest in my thesis, and especially for the creative freedom to look into different directions.
- Priv.-Doz. Dr.-Ing. Timo Mappes for the unceasing support and guidance over the last years, the interest and trust in my work and for agreeing to act as a co-examiner.
- Prof. Dr. Anders Kristensen for the chance to work on nanoporous liquid-core lasers in his group at DTU Nanotech.
- Dr. Mario Hauser and Dr. Torsten Beck for their assistance, numerous helpful discussions in all matters and support during the last three years. They gave the project a firm foundation and I benefited daily from their pioneering work.
- All other group members of the AG Kalt for the special time in this group, the great atmosphere and the constant support in all matters, especially among the PhD students.
- Dr. Christoph Vannahme and Dr. Sönke Klinkhammer for the helpful discussions about organic gain materials and lasing, and the good and constructive collaboration on microgoblet lasers.
- Tobias Wienhold for his excellent help concerning fabrication issues, the fruitful discussions and the unceasing support during the last years at IMT.

Acknowledgements

- Uwe Bog, Dr. Thomas Laue and Dr. Dr. Michael Hirtz for the exciting collaboration on the surface functionalization of microgloblets via dip-pen nanolithography.
- All members of the Mappes Biophotonic group at IMT. The discussions, especially in the group meetings, were always an enrichment for my projects and myself.
- Dr. Mads Brøkner Christiansen for his guidance in the project on nanoporous liquid-core lasers and the good time during our experiments at DTU. Special thanks go to all the group members in the optofluidics group for their help and discussions in all matters during my pleasant time in Copenhagen.
- JCMwave GmbH for providing an academic license for the use of JCMsuite. The support and input from Prof. Dr. Frank Schmidt, Dr. Sven Burger, and Dr. Benjamin Kenntner from the Zuse Institute Berlin (ZIB) were a great help for us to set up the finite element simulations.
- The students Simone Schleede, Dominik Flöss, Saskia Becker, Jan Fischer, and Michael Jenne for their excellent work and support in my projects.
- All of the staff at the APH, IMT, and DTU Nanotech for providing an excellent infrastructure for scientific research and development.
- The Deutsche Telekom Stiftung, the Karlsruhe School of Optics and Photonics (KSOP), and the Karlsruhe House of Young Scientists (KHYS) for the financial support during the PhD work.
- Above all I want to greatly thank Nina, my family and friends. Without their constant support and encouragement, I could not have finished this work!